

Co-metorship: ED A&A, France and University of Belgrade, Serbia

**DOCTORAL SCHOOL ED A&A**  
ECOLE DOCTORALE D'ASTRONOMIE ET D'ASTROPHYSIQUE  
D'ILE DE FRANCE

# PHD THESIS

to obtain the title of

**PhD of the Observatoire de Paris**  
**Specialty: ASTRONOMY AND ASTROPHYSICS**

Defended by  
Sonja VIDOJEVIC

## **Statistics of Langmuir Waves Associated with Type III Solar Radio Bursts**

Thesis advisors: Milan MAKSIMOVIC and Olga ATANACKOVIC  
prepared at LESIA, Observatoire de Paris, and  
Department of Astronomy, Faculty of Mathematics, Belgrade

defended on September 24, 2012

**Jury:**

<i>President:</i>	CHRISTOPHE SAUTY
<i>Reviewers:</i>	STUART BALE VLADIMIR KRASNOSELSKIKH
<i>Co-Mentor:</i>	MILAN MAKSIMOVIC
<i>Co-Mentor:</i>	OLGA ATANACKOVIC
<i>Examinators:</i>	STEVO SEGAN EDUARD KONTAR



# Acknowledgments

I would like to express my sincere gratitude to all people that have contributed in different ways to the work presented in this Ph.D. thesis. I will never be able to provide an exhaustive list. I would like, however, to emphasize my thesis mentors Milan Maksimovic from LESIA, l'Observatoire de Paris and Olga Atanackovic from Department of astronomy, Faculty of mathematics, University of Belgrade without whose generous help this thesis would not have been possible.

I owe my deep gratitude to French Government for the scholarship for co-mentorship (co-tutelle, Fr.) Ph.D. studies at Paris Observatory, France (l'École Doctorale "Astronomie et Astrophysique d'Ile-de-France"), given via French embassy and French Cultural Centre in Belgrade; my gratitudes go also to LESIA, Observatoire de Paris and Serbian Ministry of Education and Science (project 176002) for additional funds and grants to attend a summer school and several conferences and work shops during my studies.

SV, July 2012, Meudon

A widely-known joke states  
that with a sufficiently large data set,  
*any* hypothesis may be proved by statistics.

The other side of the story,  
general conclusion based on one or few cases,  
may be even more dangerous.

Thus, none of these approaches should be used exclusively.

# Abstract

## Statistics of Langmuir waves associated with type III solar radio bursts

**Abstract:** Interplanetary electron beams, produced by solar flares, are unstable in the solar wind and generate Langmuir waves at the local plasma frequency,  $f_p$ . These waves are then converted into the so-called type III radio bursts which are freely propagating electromagnetic emissions at  $f_p$  or its harmonic. The type IIIs are therefore observed as drifting emissions from high to low frequencies, in the kilometric wavelengths range. Since the first theoretical explanation by [Ginzburg and Zhelezniakov \(1958a\)](#), several refined models have attempted to describe in details the physical processes at the origin of type III bursts. The mechanisms of “Bump-on-tail” instabilities, Langmuir waves generations, conversion of these Langmuir waves into radio emissions throughout nonlinear wave-wave interactions etc, have been studied in detail. Of particular interest from the observational point of view are the so called *in situ* type III bursts for which the electron beam, at the origin of the emission and traveling along open interplanetary magnetic field lines, is observed directly *in situ* by a spacecraft, together with the local Langmuir waves and the resulting radio emissions. Until now only a few of these *in situ* type IIIs have been reported in the literature.

The first research study performed in this thesis was to examine the first 16 years of radio, waves and particles data recorded by the Wind spacecraft in the Solar Wind and to look for *in situ* type IIIs. Applying rigorous and careful criteria, this examination has yielded to a data set of 36 high-quality events. With such a numerous data set, which is statistically representative of the studied phenomenon, it is now possible to constrain observationally and with a better confidence the type III generation models. After having built our statistical dataset, we have studied, for each of the events, the precise shapes of the Langmuir wave power distributions, observed in the spectral domain. We have fitted these observed distributions by a Pearson’s system of probability distributions and have shown that the probability distributions of the logarithm of the Langmuir waves power spectral density belong to three “main” types of Pearson’s probability distributions: type I, type IV and type VI. In addition we have modeled the effects of the instrumental integration time of the Wind radio receivers on the observed Langmuir wave power distributions. By combining our observations with our models we have shown that it was not possible to conclude definitively, that the distribution of the Langmuir waves energy in the real temporal domain is lognormal, as it is predicted in some theories as the Stochastic Growth Theory by [Robinson \(1992\)](#).

In the last part of the thesis, we have shown how our high-quality data set of 36 *in situ* type III events can be used for further studies that could allow to constrain the theoretical models even better. For instance we have investigated the correlation between the Langmuir waves power and the energy of impulsive electron or with the power of the radio emissions themselves.

**Keywords:** Solar wind; Langmuir waves; Electron beam; Type III radio bursts.



# Résumé

## Statistiques des ondes de Langmuir associées aux sursauts radio Solaires de type III

### Résumé :

Les faisceaux d'électrons interplanétaires, produits par les éruptions solaires, sont instables dans le vent solaire et génèrent des ondes de Langmuir à la fréquence plasma locale,  $f_p$ . Ces ondes sont ensuite converties en ce qu'on appelle les sursauts radio de type III qui sont des émissions électromagnétiques se propageant librement à  $f_p$  ou leurs harmoniques. Les type IIIs sont donc observés comme des émissions dérivant des hautes aux basses fréquences, dans la gamme de longueurs d'onde kilométrique. Depuis la première explication théorique par [Ginzburg and Zhelezniakov \(1958a\)](#), plusieurs modèles détaillés ont été proposés pour décrire en détail les processus physiques à l'origine des sursauts de type III. Les mécanismes d'instabilités "Bump-on-tail", les générations d'ondes de Langmuir, la conversion de ces ondes de Langmuir en émissions radio à travers les interactions non linéaires onde-onde etc, ont été étudiées en détail. Les type III *in situ*, pour lesquels le faisceau d'électron, à l'origine de l'émission et qui voyage le long des lignes de champ magnétique interplanétaire ouvertes, sont observées directement *in situ* par un spacecraft, avec les ondes de Langmuir locales et les émissions de radio qui en résultent, sont particulièrement intéressants. Jusqu'à présent, seuls quelques-uns de ces type III *in situ* ont été rapportés dans la littérature.

La première étude réalisée dans le cadre de cette thèse a été d'examiner les 16 premières années de données ondes et particules enregistrées par le satellite Wind dans le vent solaire et de chercher les type III *in situ*. L'application de critères rigoureux pendant cet examen a fourni un ensemble, de données de 36 événements de grande qualité. Avec un tel ensemble, statistiquement représentatif du phénomène étudié, il est désormais possible de mieux contraindre les modèles de génération de type III. Après avoir construit notre base de données statistiques, nous avons étudié, pour chacun de ces événements, les formes précises des distributions de puissance des ondes Langmuir, observées dans le domaine spectral. Nous avons modélisé ces distributions avec un système de distributions de probabilités de type Pearson. Nous avons montré que les distributions de probabilité du logarithme de la densité de puissance spectrale des ondes de Langmuir appartiennent à trois types "principaux" de distributions de Pearson : type I, type IV et type VI. En outre, nous avons simulé les effets de l'intégration et de la fonction de transfert instrumentale des récepteurs radio de Wind sur les distributions de puissance des ondes de Langmuir observées. En combinant nos observations avec nos simulations, nous avons montré qu'il n'était pas possible de conclure de façon définitive, que la distribution de l'énergie des ondes de Langmuir dans le domaine temporel réel est log-normale, comme prévu par certaines théories de type "croissance stochastique" ([Robinson, 1992](#)).

Dans la dernière partie de la thèse, nous avons montré comment notre base de données constituée par les 36 événements de type III *in situ* peut être utilisée pour d'autres études permettant d'encore mieux contraindre les modèles théoriques. Par exemple, nous avons étudié la corrélation entre la puissance des ondes de Langmuir et l'énergie des électrons impulsifs ou bien encore la puissance des émissions de radio elles-mêmes.

**Mots-clés :** Vent solaire; Ondes de Langmuir; Faisceau d'électrons; Sursauts radio Solaires de type III.



# Sažetak

## Statistika Lengmirovih talasa povezanih sa Sunčevim radio erupcijama tipa III

**Sažetak:** Međuplanetski snopovi elektrona proizvedeni u Sunčevim erupcijama nestabilni su u Sunčevom vetru i proizvode Lengmirove talase na plazmenoj frekvenciji,  $f_p$ . Ovi talasi se zatim konvertuju u takozvane radio-erupcije tipa III – elektromagnetno zračenje koje se slobodno prostire na  $f_p$  ili na prvom harmoniku. Erupcije tipa III se posmatraju kao zračenje koje se pomera od visokih ka niskim frekvencijama u kilometarskom opsegu. Posle prvog teorijskog objašnjenja koje su dali Ginzburg i Železnjakov 1958. godine ([Ginzburg and Zhelezniakov, 1958a](#)), sa nekoliko poboljšanih modela izvršen je pokušaj da se detaljno opišu fizički procesi od kojih potiču erupcije tipa III. Nestabilnost usled “izbočine na repu” (“Bump-on-tail”, eng.) raspodele po brzinama čestica, generisanje Lengmirovih talasa, konverzija Lengmirovih talasa u radio-zračenje putem nelinearnih talasno-talasnih interakcija itd, su mehanizmi koji su detaljno proučavani. Sa posmatračkog stanovišta, od posebnog interesa su takozvane erupcije tipa III za koje je snop elektrona, koji se kreće duž linija sila magnetnog polja, posmatran pomoću satelita na mestu izvora emitovanja direktno-*in situ* zajedno sa Lengmirovim talasima i rezultujućom radio-emisijom. Samo nekoliko erupcija tipa III posmatranih *in situ* je do sada proučeno i opisano u literaturi.

Prvi zadatak u ovoj disertaciji je bio da se ispitaju posmatranja čestica, radio i elektrostatičkog zračenja Sunčevog vetra zabeleženih pomoću satelita Wind *in situ* tokom prvih 16 godina i da se izdvoje erupcije tipa III. Primenjujući pažljivo odabrane stroge kriterijume, dobijen je skup od 36 događaja visokog kvaliteta. Sa ovako brojnim skupom posmatranja koji je statistički reprezentativan za posmatranu pojavu, sada je sa većim poverenjem moguće postaviti posmatračka ograničenja na modele generisanja erupcija tipa III. Nakon izdvajanja statističkog skupa, za svaki od događaja je precizno određen oblik raspodele snage Lengmirovih talasa posmatrane u spektralnom domenu. Ova posmatranja su modelovana sistemom Pirsonovih raspodela verovatnoće i pokazano je da raspodela verovatnoće logaritama spektralne gustine snage Lengmirovih talasa pripada trima “glavnim” tipovima Pirsonovih raspodela verovatnoće: tipu I, tipu IV i tipu VI. Dodatno su modelovani instrumentski efekti vremena integracije radio-prijemnika satelita Wind na posmatrane raspodele snage Lengmirovih talasa. Kombinujući posmatranja i naše modele, pokazali smo da nije moguće izvesti definitivan zaključak da je raspodela energije Lengmirovih talasa u realnom vremenu log-normalna što predviđaju neke teorije kao što je Robinsonova teorija stohastičkog rasta ([Robinson, 1992](#)).

U poslednjem delu disertacije, pokazali smo kako naš skup *in situ* posmatranja visokog kvaliteta od 36 događaja tipa III može da se koristi u budućim studijama kojima bi se još bolje postavila ograničenja na teorijske modele. Mi smo, na primer, ispitali korelaciju snage Lengmirovih talasa sa energijom brzih elektrona i sa snagom radio-zračenja.

**Ključne reči:** Sunčev vetar; Lengmirovi talasi; Snop elektrona; Radio erupcije tipa III.



# Contents

<b>List of Abbreviations</b>	<b>xi</b>
<b>List of Figures</b>	<b>xi</b>
<b>List of Tables</b>	<b>xiii</b>
<b>Overview</b>	<b>1</b>
<b>1 Processes in the Solar Wind</b>	<b>5</b>
1.1 The Solar Wind . . . . .	5
1.2 Review of Plasma Emission Mechanisms . . . . .	8
1.3 Solar Radio Bursts . . . . .	12
1.4 Bursty Electric Fields . . . . .	18
<b>2 Langmuir Waves Distribution</b>	<b>25</b>
2.1 Observations and Sample Events Selection . . . . .	25
2.2 Stochastic Growth Theory Predictions . . . . .	28
2.3 Applying Pearson's System of Distributions . . . . .	34
2.4 Effect of the TNR Instrument . . . . .	38
2.4.1 The input distributions for the Langmuir waves amplitudes . . . . .	38
2.4.2 The TNR instrumental transfer function and integration time . . . . .	41
2.4.3 Simulations of the TNR response to various input distributions of the Langmuir waves power . . . . .	43
2.5 Conclusions . . . . .	49
<b>3 Other Relationships Between Particles, LW and Type III</b>	<b>53</b>
3.1 Langmuir Waves vs Particles . . . . .	53
3.1.1 Observations . . . . .	54
3.1.2 Relationships between particles and LW power . . . . .	58
3.2 LW vs Type III Power at $2f_p$ . . . . .	62
<b>4 General Conclusions</b>	<b>65</b>
4.1 Conclusions . . . . .	65
<b>A Derivation of Landau Damping</b>	<b>69</b>
A.1 Collisionless Boltzmann Equation . . . . .	69
A.2 Solution of the Vlasov Equation . . . . .	70
<b>B Pearson's System</b>	<b>73</b>
B.1 Function of Density Distribution . . . . .	73
B.1.1 Uncertainties in $\beta_1$ and $\beta_2$ estimation . . . . .	74
B.2 Probability Density Functions and Transformation Formulas . . . . .	74
<b>C STEREO TDS Observations</b>	<b>79</b>
C.1 LW Associated with <i>in situ</i> Type III Radio Bursts . . . . .	79

---

<b>D Background Removal – Pseudocode</b>	<b>83</b>
D.1 Background Removal . . . . .	83
D.2 Pseudocode . . . . .	85
<b>E Publications</b>	<b>87</b>
E.1 Vidojevic et al., 2010 . . . . .	87
E.2 Vidojevic et al., 2011 . . . . .	92
E.3 Maksimovic et al., 2011 . . . . .	97
E.4 Vidojevic and Maksimovic, 2009 . . . . .	102
<b>Bibliography</b>	<b>109</b>

# List of Abbreviations

3DP	Three-dimensional Plasma and Energetic Particle Investigation
AKR	Auroral Kilometric Radiation
CMEs	Coronal Mass Ejections
GSE	Geocentric Solar Ecliptic cartesian coordinate system
ICME	Interplanetary Coronal Mass Ejections
IMF	Interplanetary Magnetic Field
JKR	Jovian Kilometric Radiation
LW	Langmuir Waves
MFI	Magnetic Field Investigation
RAD1	Radio Receiver, frequency range from 20 to 1040 kHz
RAD2	Radio Receiver, frequency range from 1075 to 13825 kHz
RPW	Radio and Plasma Waves
SGT	Stochastic Growth Theory
STEREO	Solar TERrestrial RELations Observatory
STP	Solar Terrestrial Probes program
SWE	Solar Wind Experiment
TDS	Time Domain Sampler
TNR	Thermal Noise Receiver



# List of Figures

1.1	Schematic picture of the ingredients involved in beam-LW-T III processes.	10
1.2	Classification of solar bursts.	13
1.3	Wind/WAVES dynamical spectrum on 21 October 2002.	16
1.4	Schematic presentation of a group of particles interacting resonantly with waves in an unmagnetized plasma.	19
1.5	Rapidly fluctuating electric field.	20
2.1	Example of Langmuir waves “seen” by different Wind experiments.	31
2.2	The power of Langmuir waves obtained by integration of the power spectral density.	32
2.3	Histograms of the logarithm of Langmuir waves power before and after background removal.	33
2.4	Pearson type I and normal probability density distribution of the logarithm of Langmuir waves power.	35
2.5	Sample of 36 events in $(\beta_1, \beta_2)$ plane.	37
2.6	STEREO TDS data - Langmuir waves amplitudes distribution.	39
2.7	STEREO TDS data - LW temporal width at half maximum distribution.	39
2.8	Monochromatic sinusoidal wave packet.	40
2.9	Monochromatic sinusoidal wave packet with Gaussian envelope.	40
2.10	TNR normalization function $G(f_p, \Delta t)$ .	43
2.11	Distributions of electric wave packet amplitudes $E_i$ .	45
2.12	Comparisons between the Wind observations and our simulations, first set.	46
2.13	Comparisons between the Wind observations and our simulations, second set.	47
2.14	Comparisons between the Wind observations and our simulations, third set.	48
2.15	The values of $\beta_1$ and $\beta_2$ parameters from the the Wind observations compared to the corresponding values from our simulations.	50
3.1	Wind observations on 20 October 2002.	55
3.2	The electron flux versus energy of the EESA instrument channels.	59
3.3	Langmuir waves power versus energy of the EESA instrument channels.	60
3.4	Wave energy versus electron beam energies, simulations of Hamish Reid, 2010.	60
3.5	LW power normalized to the electron plasma pressure as a function of the electron beam speed normalized to the ambient electron thermal speed.	61
3.6	$P_{LW}$ as a function of $n_b/\sqrt{n_e}$ .	61
3.7	Type III power at $2f_p$ vs LW power.	63
C.1	STEREO TDS observations - typical Langmuir waves packages.	81



# List of Tables

1.1	Emission processes proposed for solar radio bursts. . . . .	9
2.1	List of sample events. . . . .	29
2.2	List of sample events, continuation. . . . .	30
3.1	List of impulsive (energetic) events. . . . .	56
3.2	Electron energies of EESAs channels. . . . .	57
B.1	Type: Pearson XI (normal). . . . .	75
B.2	Type: Pearson I (beta type I). . . . .	76
B.3	Type: Pearson IV (not related to any distribution). . . . .	77
B.4	Type: Pearson VI (beta type II). . . . .	78



# Overview

## Background and motivation

“It is an interesting fact that most of the material in the visible universe, as much as 99% according to some estimates, is in the plasma state.” (Gurnett and Bhattacharjee, 2005). The Sun, most stars, and a significant fraction of the interstellar medium are in plasma state. Thus, plasmas play a major role in the universe. Plasma physics is related to the formation of planetary radiation belts, the development of sunspots and solar flares, the acceleration of high velocity winds that flow outward from the Sun and other stars, the acceleration of cosmic rays, and the generation of radio emissions from the Sun and other astrophysical objects. Most of the information about astronomical objects come from measurements of their *electromagnetic radiation* only. The reason for this is simple: the electromagnetic waves can propagate through the universe far from the source where they are created. Our instruments are able to detect and measure that radiation. But, we can not measure, for example, properties of electrostatic plasma radiation or properties of plasma constituents *in situ* because we do not have instruments located at the sources of that electromagnetic radiation. While the radiative transfer in dynamic gaseous media is a well-developed discipline, the importance of the interaction between electromagnetic radiation and matter in the plasma state has only recently been recognized and analyzed. The Sun’s chromosphere, photosphere, corona and solar wind represent a unique laboratory for studies of the production, transport, and absorption of electromagnetic radiation in a plasma. The results of such studies are relevant to our understanding of radiation–plasma coupling in other astrophysical systems and to the interpretation of electromagnetic emissions from remote astrophysical objects. There are already a few examples of where we can observe all essential parties involved in energy conversion processes: auroral kilometric radiation (AKR), Jovian kilometric radiation (JKR), bow shock type II radio bursts and type III radio bursts produced as a consequence of solar wind – energetic particles interaction.

The interplanetary space in our solar system is filled with charged particles emanating from the Sun. The existence of this flow of charged particles was first presumed in 1908 by the Norwegian physicist Kristian Birkeland (1867–1917). He also recognized that this flow must comprise both positive ions and electrons. In 1951 the observations of plasma tails of comets allowed Biermann to infer that the pressure of the solar radiation on the molecules in the comet tail is by far insufficient to explain why comet tails always point away from the Sun. Rather, a solar corpuscle flow with velocities of the order of  $10^6 \text{ m s}^{-1}$  was necessary to deflect the comet tail. The name for the plasma flow streaming from the Sun, “solar wind”, was coined and introduced for the first time by Eugene Parker (Parker, 1958). He recognized that the solar magnetic field is “frozen” in the solar wind but, although the plasma flow is radially outward, solar rotation shifts the footpoints of the particle flow azimuthally, which transforms a radial outflow into an Archimedian spiral. Experimental evidence of the existence of the solar wind came with the beginning of the space age in the late 1950s and early 1960s. *In situ* observations of the interplanetary medium by Soviet moon probes Luna 1 and Luna 2, both launched in 1959 (Gringauz *et al.*, 1960) and American Mariner 2 mission to Venus (Neugebauer and Snyder, 1962), independently confirmed the existence of the solar wind. These early observations revealed that the solar wind is highly variable in nature. Few decades earlier, in the beginning of 1940s, a strong radio noise originating from the direction of the Sun was observed in metric wavelength

range. Since this initial discovery, solar radio astronomy has developed very promptly and rapid progress was made in studying solar radio signals. Theoretical, observational and instrumental development in solar plasma physics is continuing to the present time. While the accomplishments of the past decades have answered important questions about the physics of the Sun, the interplanetary medium, and the space environments of Earth and other solar system bodies, they have also highlighted other questions, some of which are long-standing and fundamental. We shall mention only few of them which are expected to be in the focus of solar and space physics scientific investigations in the forthcoming and that are of direct interest in this thesis:

- How and where are particles accelerated at the Sun? How do energetic solar events propagate through the heliosphere?
- What are the conditions under which the electrodynamic interaction of a conducting body with an ambient magnetized plasma generates waves that can affect the particle population?
- What are the the basic physical principles that govern the processes observed in solar and space plasmas?

Two of the major open questions in solar physics are to explain the fact that the Sun's corona is several hundred times hotter than the underlying photosphere and the fact that the coronal particles are accelerated to supersonic velocities within a few solar radii of the surface to form the solar wind. Resolving these mysteries – understanding how the corona is heated and how the solar wind originates and evolves in the inner heliosphere – has been recognized and identified by solar scientific community as its top science priority for the coming decade. To answer these questions, measurements from a spacecraft that passes as close to the solar surface as possible are required. A few upcoming missions, Solar Orbiter and Solar Probe, will make *in situ* measurements of the plasma, energetic particles, magnetic field, and waves inward of  $\sim 0.3$  AU to an altitude of three solar radii above the Sun's surface. This region is one of the last unexplored frontiers in the solar system. Such measurements will locate the source and trace the flow of energy that heats the corona; determine the acceleration processes and find the source regions of the fast and slow solar wind; identify the acceleration mechanisms and locate the source regions of solar energetic particles; and determine how the solar wind evolves with distance in the inner heliosphere. In addition, if suitable remote-sensing instruments will be included, these missions can complement the *in situ* measurements with valuable close-up views of the Sun.

In the research conducted for this thesis we were primarily interested in solar plasma physics related to the radio emission mechanisms, to the propagation of electromagnetic waves through the heliosphere and to the energetic solar events and their mutual interactions. Mechanisms of local generation of Langmuir electrostatic waves and electromagnetic radio waves by the propagation of an electron beam are some of the basic and fundamental problems in plasma physics. Understanding of the conversion mechanisms by which electron beam produces Langmuir waves and radio waves is of essential importance to explain some of strong radiations in plasma astrophysics from remote objects such as radio jets in active galactic nuclei, pulsars and neutron stars (e.g. Cairns *et al.*, 2001), or from nearby objects – solar radio bursts. Because our measuring instruments are in vast majority located close to the Earth, *in situ* measurements of the source (electron beam) are not possible for the remote objects. Consequently, for these objects we have measurements of electromagnetic emission in radio domain solely. Unique opportunity to study complete conversion processes we have for the objects in our solar system, thanks to the spacecraft missions with instruments orbiting or passing by these objects. Such emissions, most extensively studied, are

type III solar radio bursts – with simultaneously observed energetic electrons, as a source, and associated Langmuir and radio waves in the regions where these waves are generated (*in situ*).

The intent of this research is to examine statistically in details characteristics of Langmuir waves associated with type III solar radio bursts and electron beams responsible for their generation, all observed *in situ* simultaneously.

The first theoretical explanation of the processes responsible for the type III radio bursts generation was proposed by Ginzburg and Zhelezniakov in 1958a as a two steps mechanism, now known as a “standard type III model”. In the first step, intense Langmuir waves are excited at the local electron plasma frequency by electron beam through a “bump-on-tail” velocity distribution instability. “Bump-on-tail” instability mechanism is actually Landau growth mechanism (inverse of Landau damping, Landau 1946) caused by velocity dispersion where higher energy electron fluxes rise ahead of lower energy electron fluxes creating a positive slope in velocity distribution. In the second step, Langmuir waves are subsequently converted into radio emissions at  $f_p$  and  $2f_p$  thorough nonlinear wave-wave interactions.

Over the time, much research has been focused to refine the standard type III model. For example, taking into account effects of re-acceleration of beam particles by Langmuir waves, Zaitsev *et al.* (1972) indicated that the beam can survive large distances of the order of 1 AU and more. Another possibility is that various nonlinear wave-wave interactions can shift the Langmuir waves out of resonance with the beam electrons. This would allow the electrons to travel larger distances in quasi-relaxation time, so the beam will be stabilized. However, strong support to the standard type III model is provided by the observations of type III solar radio bursts and energetic particles, by the theoretical development and numerical simulations.

Despite the great interest and work already done, the electron beam propagation and plasma radio emission are far from well understood. This is mostly because these processes are essentially a nonlinear multiscale problems, hardly solvable. The intent of this research is to examine statistically in details basic and general characteristics of Langmuir waves associated with type III solar radio bursts and electron beams responsible for their generation, all observed *in situ* simultaneously. These statistical results obtained directly from the measurements can be used as reliable direction guidances for theoretical work, in understanding limitations of existing instruments and in construction of instruments for future missions, as well as in numerical simulations, comparison with solar flares X-ray,  $\gamma$ -ray, ground based radio, optical measurements etc. Additionally, this work is indirectly related to the acceleration of solar energetic electrons: the electron beams are source of electromagnetic emission, therefore the radio bursts can be used to track the escaping electrons from the Sun into the interplanetary medium. Furthermore, they provide possibility to investigate acceleration of electrons during a non-linear stage of beam-plasma instability to the energies greater than the energies at which they were injected.



# Processes in the Solar Wind

---

## Contents

<b>1.1</b>	<b>The Solar Wind</b>	<b>5</b>
<b>1.2</b>	<b>Review of Plasma Emission Mechanisms</b>	<b>8</b>
<b>1.3</b>	<b>Solar Radio Bursts</b>	<b>12</b>
<b>1.4</b>	<b>Bursty Electric Fields</b>	<b>18</b>

---

In this chapter we shall present a short historical review of solar wind discovery and development, following some solar wind basics. The importance of conditions in the solar wind in the Earth's vicinity is emphasized. Plasma emission mechanisms, as most prominent mechanisms, are reviewed. The connection between type III radio bursts, Langmuir waves (electron plasma oscillations) and beam-plasma system is explained. Lognormal variability in Langmuir waves and source of lognormal distribution in many solar wind parameters is discussed. A theory which includes these lognormal variation, Stochastic Growth Theory, is reviewed. Finally, the main open questions, concerning the subject of the thesis, are pointed out.

## 1.1 The Solar Wind

The solar wind is a continuous, but highly variable stream of charged particles emanating from the Sun's hot atmosphere – the corona. The particles are accelerated sufficiently to escape the gravitational pull of the Sun and travel outward into the heliosphere. Solar wind consists mainly of protons and electrons, about 95% (by number), with the rest consisting almost entirely of doubly ionized helium nuclei ( $\alpha$ -particles). The plasma temperature is found from the particle velocity dispersion in the frame of reference of the plasma bulk motion. The mean values of the proton and electron components are both between  $10^5$  and  $1.5 \times 10^5$  K, while the  $\alpha$ -particles are four to five times hotter.

The solar wind plasma is collisionless beyond a few solar radii, and because of solar wind's high conductivity the solar magnetic field is “frozen” in the plasma. The radially expanding solar wind transports the field into interplanetary space while its footpoints remain anchored in the solar atmosphere. As a result of the combined motion of outflow and the 24.47 days sidereal solar rotation period (at the Sun's equator), the interplanetary magnetic field (IMF) becomes bent into an Archimedian spiral form. It is usually referred to as the Parker spiral after Eugene Parker (Parker, 1958) who postulated this characteristic field configuration. At 1 AU<sup>1</sup> this spiral (the average direction of the field vector in the ecliptic plane) makes an angle of roughly 45° to the Earth-Sun line, but variations of many tens of degrees are common. The magnetic field magnitude is between 2 and 10 nT on average. The IMF originates in regions on the Sun where the magnetic field is “open” –

---

<sup>1</sup>1 astronomical unit (AU) is the mean distance between the Earth and the Sun, it is approximately equal  $1.495978\ 706\ 91(6) \times 10^{11}$  m. (Source: Bureau International des Poids et Mesures, <http://www.bipm.org>)

that is, where field lines emerging from one region do not return to a conjugate region but extend virtually indefinitely into space. The direction (polarity, sense) of the field in the Sun's northern hemisphere is opposite to the field in the southern hemisphere. The polarities reverse with each solar cycle. Along the solar magnetic equator plane, the oppositely directed open field lines run parallel to each other and are separated by a thin current sheet known as the "interplanetary current sheet" or "heliospheric current sheet". The current sheet is tilted (due to an offset between the Sun's rotational and magnetic axes) and warped (due to a quadrupole moment in the solar magnetic field) and thus has a wavy, "ballerina skirt"-like structure as it extends into interplanetary space. Because the Earth is located sometimes above and sometimes below the rotating current sheet, it experiences regular, periodic changes in the polarity of the IMF. These periods of alternating positive (away from the Sun) and negative (toward the Sun) polarity are known as magnetic sectors. The IMF is a vector quantity with three directional components, two of which,  $B_x$  and  $B_y$  are oriented parallel to the ecliptic plane. The third component,  $B_z$ , is perpendicular to the ecliptic and is created by waves and other disturbances in the solar wind. When the IMF and geomagnetic field lines are oriented opposite or "antiparallel" to each other, they can "merge" or "reconnect", resulting in the transfer of energy, mass, and momentum from the solar wind flow to magnetosphere. The strongest coupling, with the most dramatic magnetospheric effects, occurs when the  $B_z$  component is oriented southward. The IMF is a weak field, varying in strength near the Earth from 1 to 37 nT, with an average value of  $\sim 6$  nT.

The relative averaged elemental abundances in the solar wind vary considerably with time. Such variations have been extensively studied for the alpha particles to proton ratio ( $\text{He}^{2+}/\text{H}^+$ ),  $A(\text{He})$ , but are less well established for heavier elements. The most probable  $A(\text{He})$  value is  $\sim 0.045$ , but the  $A(\text{He})$  ranges from less than 0.01 to values of 0.35 on occasion. The average  $A(\text{He})$  is about half that commonly attributed to the solar interior, for reasons presently unknown. Much of the variation in  $A(\text{He})$  and in the abundance of heavier elements is related to the large-scale structure of the wind. For example, Fe/O and Mg/O ratios are systematically lower in high-speed streams than in low-speed flows.  $A(\text{He})$  tends to be relatively constant at  $\sim 0.045$  within quasi-stationary, high-speed streams but tends to be highly variable within low-speed flows. Particularly low ( $<0.02$ ) abundance values are commonly observed at the heliospheric current sheet.  $A(\text{He})$  values greater than about 0.10 are relatively rare and account for less than 1% of all the measurements. At 1 AU, enhancements in  $A(\text{He})$  above 0.10 occur almost exclusively within ICME plasma. The physical causes of these variations are uncertain for the most part, although thermal diffusion, gravitational settling, and Coulomb friction in the chromosphere and corona all probably play roles.

The existence of a hot expanded solar atmosphere has been known for a long time from observations during solar eclipses. It finally aroused scientific interest in the 19th century. A spectacular observation took place on 1 September 1859. While sketching sunspot groups, R. C. Carrington and R. Hodgson independently witnessed one of the most intense solar flares. Only 18 hours later one of the strongest magnetic storms was registered (Carrington, 1859; Hodgson, 1859). Hence, to reach Earth in that time, the disruption must have travelled at a velocity of  $2\,300\text{ km s}^{-1}$ , which is a remarkably fast propagation speed even according to current knowledge. More important, a connection between eruptions on the Sun and disturbances of the Earth's magnetic field was established. However, until 1951 the general belief was that the interplanetary space is basically a vacuum which is disrupted by eruptions on the Sun. Eventually, the observation that the plasma tails of active comets always point almost radially away from the Sun led Ludwig Biermann to postulate that the solar corpuscular radiation is continuous rather than

intermittent (Biermann, 1951). Shortly before the beginning of the space age Parker (1958) developed a dynamic model and predicted that interplanetary space was filled with plasma flowing rapidly outward from the Sun. Parker (1958) also introduced the phrase “solar wind” to describe the outward flowing solar corona which supplies the pressure required to stand off the local interstellar medium, to exert the necessary force on cometary plasma tails and to transmit solar disturbances to the geomagnetic field. The first in situ observation of the solar wind was realized by Soviet space probes Luna-1 and Luna-2 in 1959 (Gringauz *et al.*, 1960). Their measurements were consistent with Parker’s theory. The first conclusive measurements after that were performed by the American Mariner 2 mission to Venus in 1962 (Neugebauer and Snyder, 1962). An excellent account of these early developments is given by Parker (2001). Mariner 2 satellite was measuring a spectrum of the solar wind every 3.7 minutes almost continuously for 113 days. There was no longer any doubt that Parker had been right. The solar wind exists.

The measurements revealed that the solar wind has two underlying quasi-stationary modes. It is organised into low- and high-speed streams (velocities  $\approx 350$  and  $700 \text{ km s}^{-1}$ , respectively). They are differentiated primarily by mean velocity, source region, and composition Feldman *et al.* (2005). In all streams, the density was found to be anti-correlated with speed (Neugebauer and Snyder, 1966). These basic features of the solar wind were confirmed by all subsequent spacecraft measurements in interplanetary space. Our understanding of the solar wind has improved substantially in the last decades. The organisation of the solar wind in two different types is firmly established by now. As already found by Neugebauer and Snyder (1966) the most apparent difference between the two types is the flow velocity. Furthermore, the proton density is known to be smaller in fast streams ( $n_p \approx 3 \text{ cm}^{-3}$  at 1 AU) than in the slow streams ( $n_p \approx 10 \text{ cm}^{-3}$  at 1 AU). The fast solar wind is characterised by its relatively low variability. In contrast, the slow solar wind is highly variable. There is now increasing evidence that the acceleration of fast and slow solar wind might be the result of different mechanisms. High-speed solar wind can usually be traced back to coronal holes, regions in the corona where the density and the temperature are lower than at other places in the corona. The weak, diverging and open magnetic field lines in coronal holes extend radially outward and do not immediately return back to the Sun. The open field lines allow the plasma to flow outward into interplanetary space. The larger the coronal hole, the faster is the flow speed. The slow solar wind traces back to the active regions in the solar atmosphere where the magnetic field lines close back down to the solar surface. It is still unclear how the slow solar wind escapes from these regions. The simple pattern of fast and slow wind is occasionally disrupted by the third type of solar wind flow which is sometimes referred to as the transient solar wind. This type consists of streams caused by isolated eruptions of material from the Sun’s atmosphere known as coronal mass ejections (CMEs). They can happen at any time during the solar cycle but are more common during the solar maximum.

The conditions in the solar wind in the Earth’s vicinity are now referred to generically as “Space Weather”. These conditions include the solar wind speed and density, magnetic field strength and orientation, and energetic particle levels. They are largely controlled by the Sun, which is the source of the solar wind as well as of coronal mass ejections that impact the Earth with high densities and magnetic field strengths travelling at up to thousands of  $\text{km s}^{-1}$ , and of flares and eruptions that accelerate particles to damagingly high energies and send them towards the Earth. The Earth’s magnetosphere and atmosphere have historically protected us from most of the potentially damaging effects of Space Weather. The magnetosphere’s closed magnetic field lines cushion us from the shocks induced by changing conditions in the solar wind, and deflect much of the damaging ionized radiation flux from the Sun. The atmosphere absorbs most of the large flux of ionizing ultraviolet, extreme

ultraviolet and soft X-ray photons produced by solar flares that would otherwise damage biological cells, but life has adapted to survive the resulting conditions at the surface of the Earth.

But the increasing reliance of modern society on technologically advanced electronic systems has resulted in vulnerability to electromagnetic and particle influences from the sources external to the Earth. The inter-connected international power grids contain long-range electrical connections that are susceptible to the large-scale electric fields generated when the magnetosphere is compressed by disturbances in the solar wind, resulting in voltage and current overloads that can shut down power supplies to millions of people. Long-distance oil and gas pipelines, particularly at high latitudes, are similarly subjected to currents that cause damaging corrosion. Use of global positioning data from satellites is becoming widespread and many industries now depend on such data: air traffic is moving towards relying entirely on such technology. But the technology requires precise timing of radio signals passing through the Earth's ionosphere, where changing conditions caused by Space Weather effects can disrupt the measurements. Cell phones rely on communications at microwave frequencies where the Sun can cause harmful interference during flares, disrupting service. Other ground-based radio communication methods require low-absorption paths through the atmosphere that can be destroyed when ionizing radiation from the Sun increases the charged particle densities in the lower ionosphere. With increased astronaut activity expected in coming years as NASA sends missions to the Moon and Mars, there is concern about the possibility of deadly radiation storms occurring during manned missions. There are frequent losses of satellites in low-Earth orbit due to increased drag from the atmosphere during periods of high solar activity. Namely, during solar maximum the upper atmosphere is heated by ionizing photon fluxes and expands outwards. And since all satellites are susceptible to radiation damage in critical computing components, that can result in complete loss of control. The commercial implications of Space Weather are now widely recognized and insurance companies in particular are paying attention to its effects on their industry.

For all of these reasons, the study of Space Weather has become an important practical task in addition to the intellectual value of understanding the physical processes involved. Since most of Space Weather's effects originate in the solar atmosphere, any diagnostics there can potentially be valuable. Radio observations sample most of the activity in the Sun's atmosphere and are expected to play an important role in monitoring Space Weather sources.

The fundamental issue in all solar wind research certainly deals with the solar wind's origin: What accelerates the solar wind? Up to date no conclusive answer has been found to this question that is also closely related to the fundamental issue in coronal physics in general: How is the corona being heated? We know that the solar wind is accelerated because the corona is hot, and the corona exists because there is something heating it. However, we do not know what heats the corona, all though many theories exist (see [Cranmer \(2002\)](#) and [Hollweg \(2008\)](#) for recent reviews). Since *in situ* measurements in the vicinity of the solar surface are impossible, *in situ* solar wind measurements shall help finding underlying mechanisms.

## 1.2 Review of Plasma Emission Mechanisms

The dynamical behavior of a plasma is more complex than the dynamics of gases and fluids. This dynamical complexity has two main origins:

- (i) The dominant form of particles interaction in a plasma, Coulomb scattering, is so

weak that the mean free paths of the electrons and ions are often larger than the plasma's macroscopic length scales. Therefore, absence of collisions won't allow the plasma to be thermalized. Thus, the particles' momentum distribution functions may deviate seriously from their equilibrium Maxwellian forms and, in particular, to be highly anisotropic.

- (ii) The electromagnetic fields in a plasma are of long range. This allows charged particles to couple to each other electromagnetically and to act together as modes of excitation that behave like single dynamical entities. Much of plasma physics consists of the study of the properties and interactions of these modes.

The dynamical behavior of a plasma depends markedly on frequency. At the lowest frequencies the ions and electrons are locked together by electrostatic forces and behave like an electrically conducting fluid; this is the regime of magnetohydrodynamics (MHD). At somewhat higher frequencies the electrons and the ions can move relative to each other, behaving like two separate, interpenetrating fluids. At still higher frequencies, complex dynamics is supported by momentum space anisotropies and can be analyzed using a variant of the kinetic theory collisionless Boltzmann equation. In the collisionless Boltzmann analysis the phenomena can be treated as linear perturbations of an equilibrium state. The complexities and long mean free paths of plasmas in solar wind also produce rich nonlinear phenomena. Here, we shall focus on kinetic treatment of the dynamics and plasma emission processes in the solar wind.

**Table 1.1:** Emission processes proposed for solar radio bursts of the active Sun.

Electron velocity distribution	Coherent emission processes	Incoherent emission
thermal	–	gyro-magnetic
non-thermal	plasma emission, electron maser	gyro-synchrotron

The solar burst emission, in general, originates in small regions of the solar corona, requiring very high brightness temperatures<sup>2</sup> to yield the observed flux densities. This indicates that the emissions are not thermal and do not originate from single particles, but are emitted coherently: particles that emit the radio emission act together in phase. In the most important mechanism of these, waves in the plasma couple to each other to produce radio waves. As many electrons cooperate in phase, such a process is called *coherent* and can reach an extremely high brightness temperature. Such waves, including direct excitation of radio waves (called maser), are driven unstable by *non-thermal* particle distributions. Namely, electrons having a non-Maxwellian distribution in velocity have disposition to excite waves. The most prominent incoherent emission process observed in bursts is weakly

<sup>2</sup>The brightness is a quantity determined by Planck's frequency distribution of black body radiation. Thermal radio emission in astronomy can be described by the Rayleigh-Jeans approximation of low photon energy compared to the thermal energy,  $h\nu \ll k_B T$ . The temperature figuring in the Rayleigh-Jeans approximation of Planck's function is brightness temperature –  $T_b$ , so the equation:

$$T_b = \frac{c^2}{2k_B} \frac{B(\nu)}{\nu^2} \quad (1.1)$$

defines the Rayleigh-Jeans temperature of an equivalent blackbody that has the same power per unit area per unit frequency per unit solid angle as the astronomical source.

relativistic synchrotron radiation, called gyro-synchrotron emission. There is also a thermal burst emission at millimeter waves when the hot flare plasma emits thermal bremsstrahlung radiation. Table 1.1 summarizes the emission processes proposed for radio bursts radiation.

To interpret radio bursts, a physical cause providing the energy and an emission mechanism converting it into radio emission must be identified. The initial energy is generally assumed to be magnetic for all radio bursts. The release of free magnetic energy manifests itself in flares, but seems to be more general and related to the dynamics of the corona. Radio bursts not associated with flares include noise storms (related to emerging active regions) and moving sources related to coronal mass ejections. Hereinafter we shall focus on *plasma emission* since it is the emission process for the vast majority of solar radio bursts at decimeter and longer wavelengths. “From a theoretical viewpoint, plasma emission may be defined as any emission process in which energy in Langmuir turbulence is partially converted into energy in escaping radiation.” Melrose (1985).

The theory of plasma radiation is rather more complex than the other mechanisms mentioned because it involves two stages, and one or both may involve plasma instabilities, wave–wave and/or wave–particle interactions, and induced emission. The first stage requires the production of high levels of longitudinal (Langmuir) waves in the plasma, and the second stage requires some of the Langmuir wave energy to be converted to transverse (electromagnetic) waves that can escape from the plasma and be recorded by a radio receiver. A schematic presentation of ingredients involved in these processes is shown in Fig. 1.1.

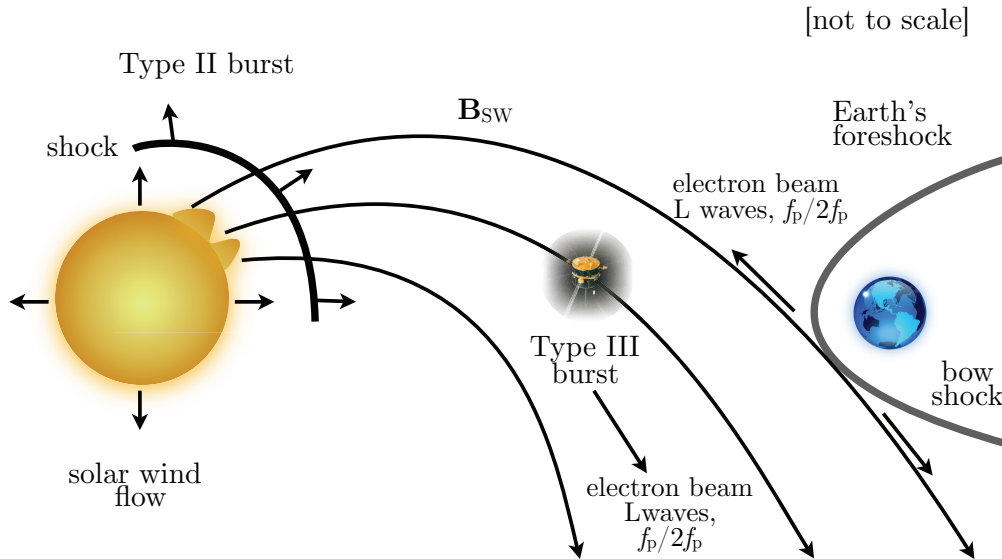


**Figure 1.1:** Schematic picture of the ingredients involved in electron beam–Langmuir waves–type III radio bursts processes.

The basic ideas of the theory were introduced by Ginzburg and Zhelezniakov (1958a), but the details have been greatly modified, updated and revised since then. The classical plasma emission mechanism is a nonlinear wave–wave interaction of Langmuir, ion-acoustic, and electromagnetic waves. In the wave–wave mechanism, existing Langmuir waves ( $L$ , for longitudinal waves) decay into backward propagating Langmuir waves ( $L'$ ) and ion-acoustic waves ( $S$ , for sound or also called acoustic waves) by the electrostatic

decay process  $L \rightarrow L' + S$ . Forward propagating Langmuir waves ( $L$ ) also decay, stimulated by the presence of ion-acoustic waves produced by the initial electrostatic decay, to give electromagnetic waves near plasma frequency,  $f_p$ :  $L \rightarrow T_f + S'$  (here,  $f$  stands for fundamental). The forward and backward propagating Langmuir waves combine together, resulting in an electromagnetic wave near the first harmonic (the process is also known as coalescence),  $2f_p$ :  $L + L' \rightarrow T_h$  ( $h$  stands for harmonic). In each case the Langmuir waves are assumed to be limited to a narrow range ( $< 20\%$ ) around a resonant wavenumber  $\kappa$  given by  $\kappa = \omega_p/v_p$ , for angular plasma frequency  $\omega_p + 2f_p$  and electron beam speed  $v_b$ . These three sorts of waves interact and combine together and produce a maximum response when their wave vectors and frequencies satisfy the resonance conditions  $\kappa_L + \kappa_3 = \kappa_T$  and  $\omega_L + \omega_3 = \omega_T$ . Here the subscript  $L$  represents longitudinal Langmuir waves (electrostatic),  $T$  represents transverse waves (electromagnetic) and subscript 3 a third wave or influence. These resonance conditions correspond to momentum and energy conservation respectively. For fundamental radiation we have  $\omega_T \approx \omega_L \approx \omega_p$ , so that  $\omega_3$  must be small – it can be a low-frequency wave or a low-frequency fluctuation of the electric field produced by a thermal ion. Also, since  $|\kappa_T| \ll |\kappa_L|$ , it is required that  $\kappa_3 \approx -\kappa_L$ . For the harmonic radiation, it is  $\omega_T \approx \omega_L \approx 2\omega_p$  and  $k_T \approx \sqrt{3}\frac{\omega_p}{c}$ . To obtain frequency matching, it is necessary that  $\omega_T \approx \omega_3 \approx \omega_p$ , which leads to the idea that two Langmuir waves coalesce to produce a radio wave. For momentum matching, since  $|\kappa_L| \approx \frac{\omega_p}{v_o} \gg |\kappa_T|$ , it is necessary that  $\kappa_L \approx -\kappa_3$ . The direction of  $\kappa_L$  is approximately in the direction of the electron streaming, so for the coalescence to work there must be a way to obtain a secondary Langmuir wave distribution that is approximately isotropic or in the backward direction.

Spacecraft observations of spatially coincident Doppler-shifted ion-acoustic waves and Langmuir waves in the solar wind and Earth's foreshock support this theory (Lin *et al.*, 1986; Kellogg *et al.*, 1992; Cairns and Melrose, 1985; Hospodarsky and Gurnett, 1995; Thejappa *et al.*, 2003). However, there are studies showing that some low frequency signals interpreted as ion-acoustic modes may be attributed to non-linear plasma sheath interaction with the probes performing the measurements (Boehm *et al.*, 1994).

A second radiation mechanism is the linear mode conversion in which a nearly monochromatic Langmuir  $z$ -mode wave incident on a density gradient partially reflects and partially converts into electromagnetic radiation near  $f_p$  (Yin *et al.*, 1998; Kim *et al.*, 2008). Here the density gradient spatial scale must be larger than the plasma skin depth  $c/\omega_p$ . The reflected Langmuir wave then collides with the primary Langmuir wave to produce  $2f_p$  radiation. A study by Bale *et al.* (1998) found that Wind<sup>3</sup> observations of Langmuir electric fields perpendicular to the local magnetic field were consistent with the presence of Langmuir  $z$ -mode waves. This was interpreted by Bale *et al.* (1998) as evidence for mode conversion, but instead may indicate that the plasma was sufficiently magnetized for  $z$ -mode Langmuir waves to be detectable (Willes and Cairns, 2000). Moreover, STEREO<sup>4</sup> observations show

<sup>3</sup>NASA launched the Wind spacecraft in November, 1994 to the Earth's L1 Lagrange point as the interplanetary component of the Global Geospace Science Program within the International Solar Terrestrial Physics (ISTP) program. The spin stabilized spacecraft, with its spin axis pointing ecliptic north, carries eight instrument suites that provide comprehensive measurement of particles from solar wind thermal populations to the solar energetic component, and of fields from DC magnetic to radio waves and  $\gamma$  rays. The Wind instrument suite provides comprehensive and also uniquely high time resolution in situ solar wind measurements that enable the investigation of wave-particle interactions.

<sup>4</sup>STEREO (Solar TERrestrial RELations Observatory) is the third mission in NASA's Solar Terrestrial Probes program (STP). The mission, launched in October 2006, has provided a unique and revolutionary view of the Sun-Earth System. The two nearly identical observatories – one ahead of Earth in its orbit, the other trailing behind – have traced the flow of energy and matter from the Sun to Earth. STEREO has revealed the 3D structure of coronal mass ejections; violent eruptions of matter from the Sun that can disrupt satellites and power grids, and help us understand why they happen. STEREO is a key addition to the fleet of space weather detection satellites by providing more accurate alerts for the arrival time of

that a perpendicular Langmuir wave structure is also consistent with three-dimensional eigenmode localization by solar wind density cavities (Malaspina *et al.*, 2009).

A third mechanism is the quasi-mode method given by Yoon *et al.* (1994) in which induced scattering of forward propagating Langmuir waves of thermal ions induces backward propagating Langmuir waves. This mechanism generates  $2f_p$  radiation only. The oppositely directed waves interact to generate an electrostatic quasi-normal mode at  $2f_p$  that is converted to an electromagnetic wave by a non-linear mode coupling process in regions of decreasing density. This mechanism has not yet been fully supported by the measurements.

A fourth mechanism is antenna radiation, where plasma oscillations at  $f_p$  directly drive currents at  $2f_p$ , which radiate simply as a collection of accelerating charges (Papadopoulos and Freund, 1978; Goldman *et al.*, 1980). Prior formulations of this mechanism lack a description of localized wave packet modulation consistent with observations, preventing evaluation of the vector potential associated with the driving electrostatic currents without simplifying assumptions. Comparisons between a similar antenna radiation mechanism and spacecraft data were carried out by Pottellette *et al.* (1992) in the context of auroral kilometeric radiation. Antenna radiation is unique in that it is the only mechanism not independent of a backscattered Langmuir wave to generate  $2f_p$  radiation. Early work on antenna radiation considered localization of currents by Langmuir wave collapse (Zakharov, 1972).

### 1.3 Solar Radio Bursts

Solar radio signatures connected to the solar eruptive events and energetic electron beams are of particular relevance in the context of the thesis. The focus is therefore on the nonthermal solar radio bursts, which are usually generated by plasma emission. Solar radio bursts are normally classified according to two criteria: the wavelength of observation and the morphological appearance in dynamic radio spectra. These different classification schemes are given below, with an emphasis on the underlying physical processes.

Starting at the highest frequencies (i.e. the lowest heights) different spectral regimes are reviewed in the following.

*Microwaves* ( $f > 3$  GHz). They originate low in the corona and/or in the chromosphere (at heights of  $h < 0.1 R_\odot$ ). Microwave emission is generally broad-band and continuous (i.e. there are no fine structures). Most of the microwave bursts are due to the gyrosynchrotron emission of relativistic electrons. Microwave bursts are often closely correlated with the flare's hard X-ray emission, which implies that they are generated by the same energetic electron population that produces the hard X-ray bremsstrahlung – the same particle population that contains the bulk of the energy released in the flare. Therefore, microwave observations of flares provide important information on the primary particle acceleration mechanisms.

*Decimeter/Meter Waves* ( $f < 3$  GHz). This remains the best-studied wavelength regime. Radiation in this range is coming from the low and the middle corona ( $h \approx 1 R_\odot$ ), respectively. In contrast to microwaves, most of the emission is non-continuous, it can be narrow-band, and a multitude of distinct fine structures, harmonics and frequency drifts is observed. The high fluxes and brightness temperatures of the observed bursts require a coherent emission mechanism – namely plasma emission.

*Dekameter Waves* ( $f < 30$  MHz). The dekametric regime is generally similar to the metric, but it originates from the higher corona. Emission mechanisms and morphologies of bursts are also similar. Observations in the dekametric band provide an important link between the comparatively well known middle corona and the interplanetary space.

---

Earth-directed solar ejections with its unique side-viewing perspective.

*Hectometer/Kilometer Waves* ( $f < 3$  MHz). With respect to the emission mechanisms and morphology of bursts, this range is also similar to the meter/dekater bands. However, as these extremely long wavelengths correspond to the plasma frequency of the IP medium, they are of particular interest in the context of influence on the Earth. Observations in this regime allow the tracking of disturbances from the high corona up to the Earth (and even beyond it).

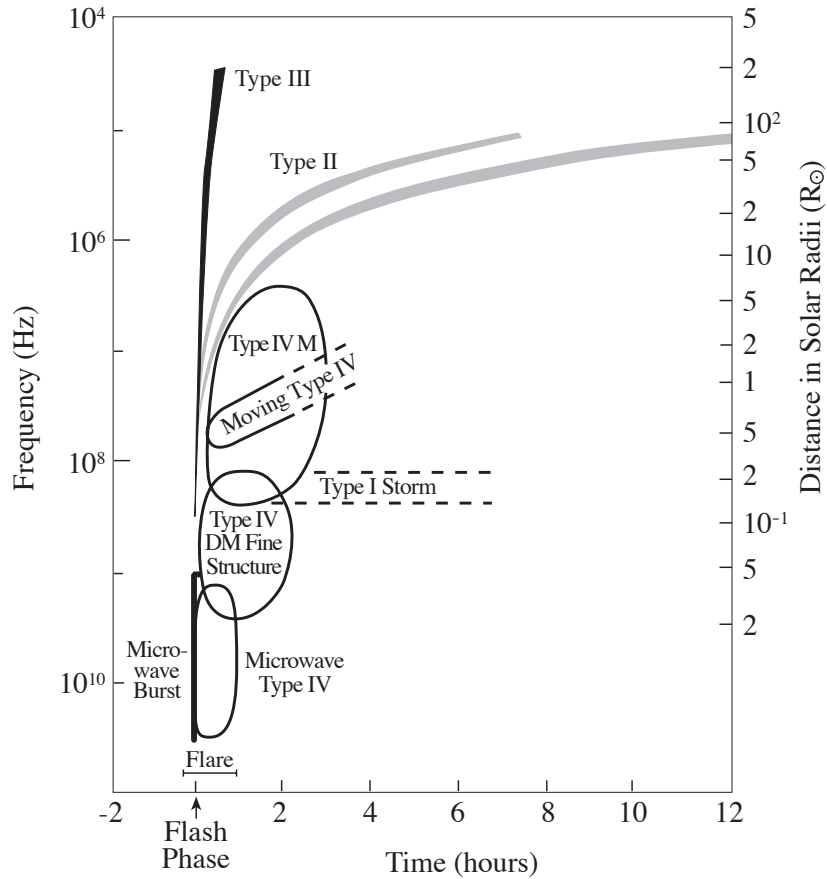


**Figure 1.2:** Classification of the solar radio bursts according to morphological appearance in dynamic radio spectra. As is the convention for solar radio spectrograms, time runs from left to right and frequency decreases from bottom to top (corresponding to increasing height). Adopted from Lang (2001).

The classification of solar radio bursts according to morphological appearance in dynamic radio spectra is schematically shown in Fig. 1.2. This is an idealized dynamic radio spectrum and it shows the basic types of solar radio bursts (frequency decreases from bottom to top). Important characteristics of the bursts are their duration  $\Delta t$ , their bandwidth  $\Delta f$ , and their drift rate,  $Df = df/dt$ . In the following, the numerical values given for these parameters are referred to the metric range.

Solar radio bursts were amongst the first phenomena identified as targets for radio astronomy. Solar radio bursts at frequencies below a few hundred MHz were classified into 5 types in the 1960s (Wild *et al.*, 1963). It is generally accepted that all following bursts are generated by plasma emission (though at least some type IV bursts may be due to

gyrosynchrotron emission). The microwave bursts, which are due to other mechanisms, have already been discussed previously.

**Type I Bursts.** Type I bursts (Fig. 1.2) are characterized by a very short duration ( $< 1$  s), they have bandwidths of a few tens of MHz, and they do not show obvious drifts. Type I bursts are only observed at metric wavelengths and always appear in large numbers, forming irregular structures superposed on a continuous background. These so-called noise storms can last for hours to days. Type I emission is therefore not necessarily associated with flares. It is thought to be generated by electrons accelerated to a few thermal energies by an ongoing local energy release in closed coronal structures.

**Type II Bursts.** Type II bursts (Fig. 1.2) are narrow-band (a few MHz) emission lanes which slowly drift towards lower frequencies ( $D_f \approx 0.1 - 1 \text{ MHz s}^{-1}$ ). Both fundamental and harmonic bands can be present, and sometimes each band is split into a higher and a lower frequency lane (with a relative separation of  $\Delta f/f \approx 0.1$ ). Most bursts are observed in the metric range, but some are also detected in the dekametric to kilometric regimes. These are called interplanetary (IP) type II bursts. A type II burst is generated by a magnetohydrodynamic shock wave which propagates outwards through the corona. In the corona and in the IP medium, a type II-generating shock is formed when a disturbance exceeds the Alfvén speed

$$v_A = \frac{B}{\sqrt{\mu_0 m_p \mu N}} \quad (1.2)$$

where  $\mu_0$  is the permeability of vacuum,  $m_p$  the proton mass,  $\mu$  the mean molecular weight (0.6 in the corona), and  $N$  the total particle number density ( $N = 1.92 N_e$  for  $\mu = 0.6$ ). Velocities of coronal type II sources are of the order of  $1000 \text{ km s}^{-1}$ . At the shock front, electrons are accelerated to suprathermal and/or high energies. They excite Langmuir waves which are then converted into escaping radio waves by the plasma emission process outlined in Sec. 1.2. Further evidence for electron acceleration is provided by the structure observed in some type II bursts, in which small type III-like bursts (see below) emanate from the “backbone” of the emission lane. These features are interpreted as accelerated electrons which escape from the shock. Type II bursts are associated both with flares and CMEs, though there is no one to one correspondence. This has resulted in an extended discussion on the real nature of the shocks which produce the bursts, the candidates being a flare-generated pressure pulse or a piston-driven shock created by a CME. The current view is that both flares and CMEs can create shocks, but it seems that the flare-generated disturbances usually cannot penetrate to IP space, since most of those bursts cease at  $\approx 20 \text{ MHz}$ . This is probably due to a local maximum of the Alfvén speed in the higher corona. Therefore, most hectometric/kilometric type II bursts seem to be generated by CME-driven shocks. These bursts are associated with fast CMEs, long-living energetic solar particle events, and IP shocks, and are therefore particularly relevant for space weather purposes.

**Type III Bursts.** Type III bursts (Fig. 1.2 and Fig. 1.3) are the most common flare associated bursts and can occur over a wide frequency range, from  $\approx 1 \text{ GHz}$  to  $\approx 10 \text{ kHz}$ , corresponding to a height range extending from the low corona to beyond 1 AU. They are mainly defined by their rapid drift ( $D_f \approx 100 \text{ MHz s}^{-1}$ ) towards lower frequencies, they have a short duration (seconds) and a relatively broad bandwidth ( $\Delta f \approx 100 \text{ MHz s}^{-1}$ ). Many type III bursts display harmonic structure at metric to dekametric wave lengths. Type III bursts are characteristic of the impulsive phase of solar flares, where they often occur in groups of  $\approx 10$  bursts, lasting a few minutes. Non-flare associated type IIIs form storm type III bursts, somewhat reminiscent of type I noise storms. The exciting agent of a type III burst is a beam of mildly relativistic electrons ( $v \approx 0.3 c$ ) which propagates out of the corona along open magnetic field lines (the beams may also propagate in closed loops,

resulting in so-called inverted-U bursts). As in the case of type II bursts, the accelerated electrons generate plasma emission. Type III bursts can propagate through IP space up to the Earth, where the radio-generating electrons can be directly observed as impulsive electron events. Type III bursts therefore give vital clues on the acceleration of electrons in flares, as well as on the propagation of these particles through IP space. A special class of type III bursts are the so-called shock-accelerated (SA) type III bursts. They start from a type II backbone and are somewhat reminiscent of herringbones, but contrary to them, SA type III bursts extend into the IP medium. They are thought to be generated by electron beams which are accelerated at a coronal (or IP) shock.

**Type IV Bursts.** Type IV bursts are flare-related broad-band continua (Fig. 1.2). They are divided into two distinct categories: stationary type IV bursts show no frequency drift and are characterized as broad-band, long lasting continuum features which show a wide variety of fine structures – pulsations, zebra patterns and fiber bursts. They follow major flares and may evolve into type I storms. On the other hand, moving type IV bursts display a slow drift towards lower frequencies (corresponding to source velocities of up to several hundreds  $\text{km s}^{-1}$ ), while they are otherwise morphologically similar to stationary type IVs. Type IV bursts are believed to be either due to plasma emission or due to gyrosynchrotron emission. In any case, the electrons which are responsible for the emission are trapped in a closed magnetic structure. This can be a set of coronal loops (stationary type IV), or a rising structure like an expanding loop or a plasmoid which is ejected during an eruptive event. The bulk of the electrons remains confined to the magnetic structure due to magnetic mirroring at converging magnetic field lines (i.e., at the feet of coronal loops), therefore, we observe prolonged emission. Type IV bursts are only rarely observed in the near-Sun IP medium, but they are nevertheless interesting for solar-terrestrial studies since they can provide valuable information on the energy release mechanism of solar eruptive events. Several flare models require the formation and ejection of plasmoids, and CME cores might actually be sources of type IV bursts.

**Type V Bursts.** Type V bursts are continuum bursts which start during or immediately after a group of type III bursts. They are possibly created by electrons which have been removed from the type III-generating beam by pitch angle scattering.

Type III radio bursts are most important for the subject of the thesis, so they will be elaborated in more details in the following. Type III bursts are brief radio bursts that drift very rapidly in frequency versus time (Fig. 1.3). Because the emission is at the plasma frequency or its harmonic, the drift in frequency with time can be directly converted into a drift from high to low ambient coronal density with time. Coronal density models can then be used to infer a velocity for the exciter. Drift rates at higher frequencies are faster, because the density scale heights lower in the atmosphere are smaller, and a disturbance at constant speed will therefore have a higher frequency drift rate. The inferred speed clearly depends on coronal density modeled, but the general result is that for relatively “fast-drift” bursts (type III bursts consistently have the fastest drift burst rates at metric wavelengths), the exciter speeds tend to be of order one-tenth the speed of light, and accordingly the only plausible drivers for type III bursts are electron beams of energies up to tens of keV. Such electron beams have long been known to be very efficient producers of electrostatic Langmuir waves via the bump-in-tail instability. They can be seen to start at densities corresponding to the very low corona (frequencies up to several GHz) and propagate all the way out to 1 AU, where their electrons can be detected in situ by spacecraft in the solar wind. In addition to isolated bursts, type IIIs are commonly seen in the impulsive phase of solar flares, and the connection they imply between the acceleration region in solar flares and the open field lines that reach the solar wind makes them important for understanding field line connectivity in flares and the access of flare-accelerated particles to the Earth. Large

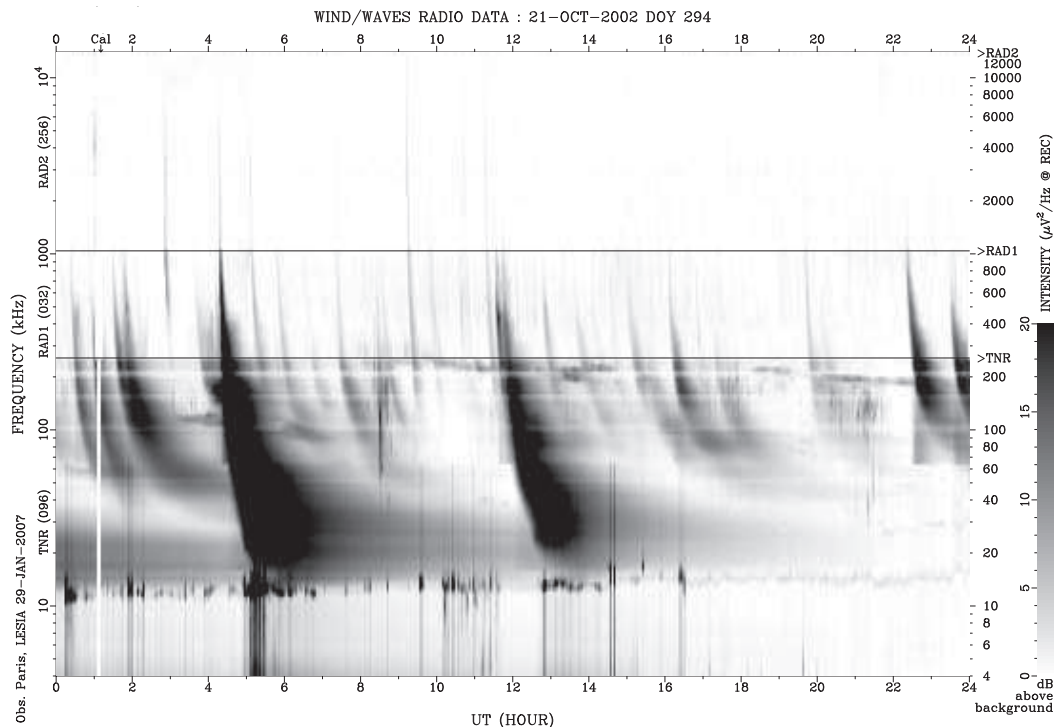


**Figure 1.3:** Wind/WAVES dynamical spectrum on 21 October 2002. Approximate GSE coordinates of the Wind spacecraft during the day are  $(x, y, z) = (100, 6, 5)$  Earth radii. A lot of type III bursts can be seen on this dynamical spectrum with plenty of enhanced Langmuir waves emissions. The plasma frequency at 1 AU increases slowly from about 10 to 18 kHz during the day.

flares are not necessary for production of electron beams: type III bursts can be seen at times when there is no activity at other wavelengths. The plasma emission mechanism is very efficient at converting a small amount of free energy in an electron velocity distribution into the electromagnetic emission, so it does not require so many electrons in a beam to produce a detectable type III burst.

Despite this fact, it is well established that a large fraction of flares, particularly impulsive flares (Cane and Reames, 1988), exhibit type III bursts at the onset. The implication is that the energy which is responsible for the heating of the corona open magnetic field lines is released, and so such type III bursts potentially form a diagnostic tool of energy release and acceleration. According to Aschwanden *et al.* (1993) cases were found where both upgoing and downgoing electron beams produced radio signatures, originating in a frequency range corresponding to a density of over  $10^9 \text{ cm}^{-3}$ . There it was also suggested that the downgoing beams were well-correlated with particle precipitation into the solar chromosphere revealed by the structure in the hard X-ray emission time profile, further connecting the type III bursts to the main energy release events in flares. The presence of type III bursts generated by the energy release in flares has implications in flare models, and therefore for Space Weather prediction, because the electron beams are seen to propagate out to regions of very low density and therefore must be on open field lines. We believe that the flare energy release involves magnetic energy density stored in the corona in a form, such as sheared non-potential magnetic fields, that is available for conversion to

the particle energy (thermal and nonthermal). This is because no other medium known to us offers the possibility of storing sufficient energy to explain large solar flares (Wu *et al.*, 1989). Conversion of magnetic energy into particle energy may take place as a by-product of the mechanism of magnetic reconnection, in which magnetic field lines may change topology and connectivity (field lines may be cut and then reconnected to other field lines, a non-ideal MHD process). The strongest magnetic fields in the solar photosphere occur in sunspots: most of the field lines passing through strong field regions appear to close within the solar atmosphere (i.e., both footpoints are connected to the solar photosphere), which suggests that the energy available for flares is probably stored on closed field lines. However, that need not be the case and open field lines (which have one end rooted in the solar photosphere and the other pulled out into the solar wind) also may be involved. A popular model for long-duration flares and the associated coronal mass ejections involves a so-called “helmet-streamer” configuration in which closed loop field lines lie under a current sheet which separates regions of open field lines of opposite magnetic polarity: reconnection at the top of the loop creates new closed field lines (as well as field lines not rooted in the solar surface) and releases energy. In this model open field lines are an intrinsic part of the energy release process, and it seems natural that particles accelerated in the energy release would find their way onto open field lines. However, type III bursts are mostly found in the flash phase of very impulsive flares (Cane and Reames, 1988), which are not thought to be a consequence of the helmet-streamer model. Other models applied to very impulsive flares involve interactions between pairs of closed loops, such as when loops carrying magnetic flux emerging from beneath the solar photosphere reconnect with pre-existing loops in the solar corona. In such models the outcome of reconnection is two new closed loops, and then no open field lines are involved, making it difficult to realize how type III bursts could originate in the energy release region. Another class of flare models involves reconnection between one open field line and one closed field line, in which topology is switched, and in this model we again have open field lines as an intrinsic part of energy release.

In addition, a class of type III bursts that occurs somewhat after (typically 10 minutes or so, during Type II emission) the impulsive phase has been reported to show a very high degree of association with solar energetic particle events (Cane *et al.*, 2002). These bursts occur in groups and are labelled type III-l; they are commonly seen below 14 MHz. Their association with solar energetic particle events has made them an important topic of current studies. Initially, it was thought that these fast drift bursts might originate in a Type II shock, since they often occur at the same time (i.e., well after the onset of the impulsive phase, hence a phenomenon quite different from the impulsive-phase type IIIs discussed above) and in a similar frequency range (Dulk *et al.*, 2000).

Cane *et al.* (2002) found that nearly all solar energetic proton events are preceded by the above mentioned groups of type III-l bursts, and that they are particularly prominent in dynamic spectra below the ionospheric cutoff at about 10 MHz. Since the type III bursts in a type III-l group often start at frequencies above the Type II emission visible in dynamic spectra at the same time, they argued that the type III-ls had to originate lower in the corona than the Type II shock. Thus III-ls were unlikely to originate in the Type II shock or in any shock associated with a fast CME. This implies that the source of the type III-l emission and, by implication, any associated energetic protons, was more likely to be in the flare region, and that open field lines must connect the acceleration region to the solar wind. This picture is in contrast to the belief that large gradual solar energetic particle events are due to acceleration of particles by large coronal mass ejections (Reames, 1999). The association of type III-l with solar energetic particle events is still being investigated and the exact relationship is by no means established, but if it holds up then their observation, occurring up to tens of minutes before the arrival of the corresponding solar energetic

particle events at the Earth, would hold promise as a Space Weather diagnostic tool.

### Beam–plasma system

One of the main achievements of the kinetic theory of plasmas was the discovery of Landau damping in 1946 (Landau, 1946). Although this first derivation was a straightforward application of the theory of Laplace transforms, the existence of Landau damping was questioned since its physical nature was not clear. This problem was not fully resolved until 1961 when a more physical derivation was made by considering the particle distribution to be built up by cold streams (Dawson, 1961). The problem of Landau damping of longitudinal plasma oscillations Dawson (1961) investigated by dividing the plasma electrons into two groups. The first group was the main plasma and consisted of all electrons with velocities considerably different from the wave velocity while the second group, the resonant electrons, consists of all electrons with velocities near the wave velocity. It was assumed that initially the main plasma had a wave on it while the resonant particles are undisturbed. It is shown that equating the gain in energy of the resonant particles to the loss in energy of the wave gave the correct Landau damping. The possibility of observing Landau damping in the laboratory was finally demonstrated in 1966 (Malmberg and Wharton, 1966).

Landau (1946) showed that plasma waves in unmagnetized collisionless plasmas suffer damping due to wave-particle interactions, or "Landau damping". The physical mechanism of Landau damping can be understood as follows: at Landau resonance the particles do not see a rapidly fluctuating electric field of the wave, and hence they can interact strongly with the wave. Those particles having velocities slightly less (greater) than the phase velocity of the wave are accelerated (decelerated) by the wave electric field to move with the wave phase velocity. Thus the group of particles moving slightly slower (faster) than the phase velocity gain energy from (lose energy to) the wave. In a collisionless plasma characterized by a Maxwellian distribution function, the number of slower particles (in any interval around the phase velocity) is greater than the number of faster particles, as is shown in Figure 1.4, upper panel. Therefore, energy gained from the waves by slower particles is greater than the energy given to the waves by faster particles, thus leading to net damping of the waves. Consequently, Landau damping provides dissipation for a collisionless plasma. In a non-Maxwellian plasma, for example, a beam-plasma system, one can create a situation where in a given velocity interval around the phase velocity of the wave, there is a greater number of faster particles than of slower particles. Such a case is shown in Figure 1.4, lower panel. This situation corresponds to the inverse Landau damping or plasma (Cherenkov) instability, as the waves grow by gaining energy from the particles. For this latter situation, one can say that there is "free energy" available for wave growth.

Beam–plasma interactions play a crucial role in various fields of physics and in the theoretical study of the linear and nonlinear regime of beam-plasma instabilities. The long-standing academic development of this field is being revived and challenged by technological progress making accessible new physical regimes by new observational data and theories in astrophysics.

An extended discussion and mathematical derivation of Landau damping from the collisionless Boltzmann equation (also called Vlasov equation, see footnote 1 on page 70) is given in Appendix A.

## 1.4 Bursty Electric Fields

*In situ* observations of extremely bursty waves with widely varying electric fields are quite

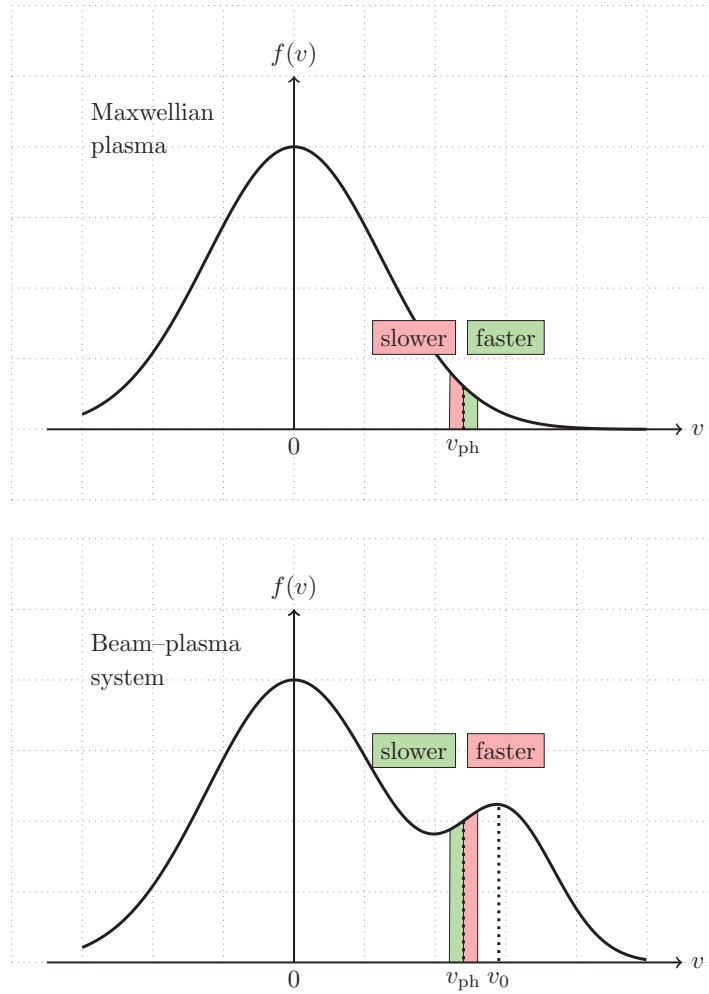


**Figure 1.4:** Schematic of a group of particles interacting resonantly with waves in an unmagnetized plasma. Upper panel: Maxwellian plasma (in thermal equilibrium). The energy gained from the waves by the slower particles (red area) is more than the energy given to the waves by the faster particles (green area). Lower panel: beam-plasma system where the phase velocity of the wave,  $v_{ph}$ , is less than the beam speed  $v_0$ . The energy gained from the waves by the slower particles (green area) is less than the energy given to the waves by the faster particles (red area).

common in space physics. Examples include Langmuir waves seen in type II and III solar radio sources, the Earth's foreshock, Langmuir, beam, and z-mode waves in polar cap and auroral regions of the magnetosphere, and electromagnetic ion cyclotron and mirror-mode waves in the magnetosheath. Fields can rapidly fluctuate by orders of magnitude, (as can be seen in Fig. 1.5 for Langmuir waves associated with a type III burst) leading to extremely broad probability distributions of field strength. Herein, we discuss the physical meaning of a probability distribution that could stand behind the observed electric field pattern and one of the theoretical approaches, namely the Stochastic Growth Theory.

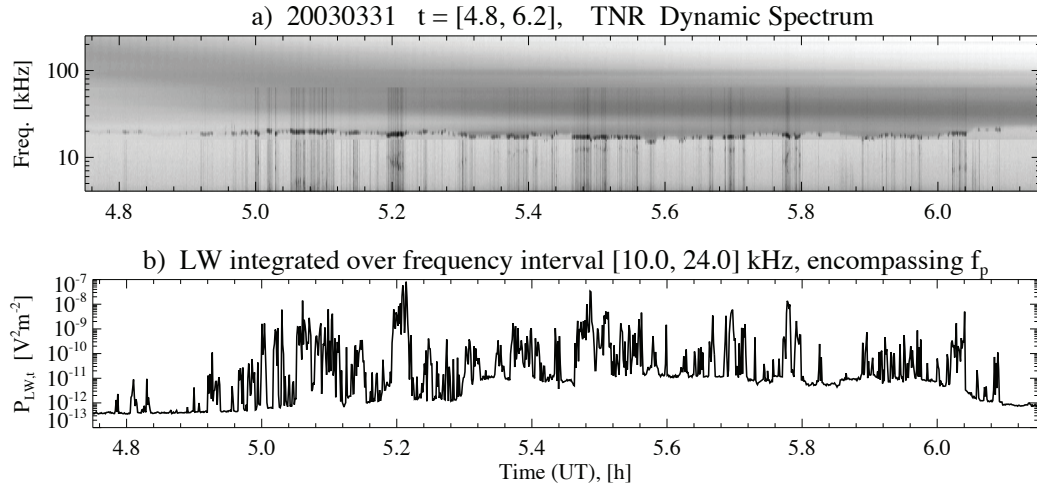


**Figure 1.5:** Rapidly fluctuating electric field of Langmuir waves recorded by TNR receiver on 31<sup>st</sup> March 2003. Panel a) part of type III radio burst in the upper part and intensive Langmuir waves about plasma frequency ( $f_p \approx 18$  kHz) in the lower part of the panel on dynamic spectrum can be seen. Panel b) Bursty Langmuir waves integrated over narrow frequency range around plasma frequency.

### Why lognormal variability?

The lognormal shape of statistical distribution has a deep physical meaning. In statistical theory it arises in the case of multi-step cascade processes where each step multiplies the previous outcome. A variable  $q$  with lognormal distribution can originate from a specific multiplication generator. The multiplication coefficient of that generator can be represented as  $q = e^y$ , where  $y$  is distributed normally with the mode  $\mu$  and with standard deviation  $\sigma$ . In other words, the variable with lognormal distribution is a result of numerous multiplications of random variables. A very important feature of this distribution is its dimension-independence, for example: if the diameter follows this distribution, so will also the surface, volume and any further power function of these quantities. What is the difference between normal and lognormal variability? Both forms of variability are based on a variety of “forces” acting independently of one another. A major difference is that the effect can be additive or multiplicative, thus leading to normal or lognormal distribution, respectively.

The lognormal statistical distributions of the solar wind parameters and interplanetary magnetic field might indirectly point toward the multiplicative transformation of local characteristics under alternating random amplification and weakening of waves, compression and rarefaction of inhomogeneities in turbulent processes of transfer of plasma mass, energy and

momentum on the Sun and in the heliosphere. For example, in the downstream region of fast interplanetary shock, the values of plasma density and magnetic field are multiplied by compression. We can assume that the solar wind plasma density and IMF intensity might be generated and/or modulated in the regions of alternate compression/decompression in the solar atmosphere. On the other hand the lognormal distribution itself is not sufficient for conclusions about predominantly random and irregular nature of a multiplicative process because regular processes with very high levels of complexity and multi-dimensions are rather difficult to distinguish from the random process. Both of those possibilities do not seem excluding each other in interpretation of observations. They rather supplement the interpretation from different points of view.

The fact that statistical properties of heliospheric parameters do not correspond to normal distribution is not surprising. Normal distribution is suitable for modeling equilibrium and stationary processes. On the contrary, the solar wind plasma and IMF are not in equilibrium and they are not stationary. They change with distance and with heliographic latitude and longitude, i.e. they are characterized by various spatial gradients. Moreover, the heliosphere is populated by various kinds of large-scale transient events, interaction regions and waves. They are characterized by meaningful temporal variations within solar cycle and from cycle to cycle. However, those variations are not completely random but reveal specific spatial and temporal patterns. The lognormal distribution is more proper for such non-equilibrium and non-stationary random processes with characteristic spatial and temporal scales. In the solar wind, as a collisionless plasma system, the particle velocity distribution function is not restricted to be Maxwellian. Thus, it is not in an equilibrium, but may exhibit strong distortions. These distribution function distortions may be source of an energy that supports the development of different kinds of kinetic instabilities. Concerning the study in this thesis, one such example are bursty Langmuir waves associated with type III radio bursts produced by electron beam interaction with ambient plasma. Theoretical results show that the resulting electric field of Langmuir waves is in an exponential form (see, for example, form of Eq. A.9 in Appendix A), which implies that underlying processes might be of multiplicative character.

### Lognormal distribution

The lognormal distribution (see, e.g. [Aitchison and Brown, 1957](#)) is obtained for any cascade-like process where the final result of the entire process is a product, rather than a sum, of the partial results from the individual steps in the cascade. To such a process an attribute “lognormal” can be assigned. Thus, a lognormal process is one in which the random variable of interest results from the product of many independent random variables multiplied together. Formally, the outcome is a stochastic variable  $q$  given by a product of stochastic variables  $a_i$ , corresponding to the various steps  $i$ , that is  $q = \prod_{i=1}^N a_i$ . By taking logarithms this product is turned into a sum,  $\ln q = \sum_{i=1}^N \ln a_i$ . The central-limit theorem can now be applied, provided that the number of terms  $N$  is large and that each term  $\ln a_i$  fulfils the regularity condition of having a finite variance. This leads to a normal distribution in positive random variable  $\ln q$  with mean  $\mu$  and standard deviation  $\sigma$ ,  $\mathcal{N}(\ln q|\mu, \sigma^2)$  or shorter  $\mathcal{N}(\mu, \sigma^2)$ . Transforming to the original variable  $q$ , one obtains its probability density function:

$$P(q) = \begin{cases} \frac{1}{q\sigma\sqrt{2\pi}} e^{-\frac{1}{2}\left(\frac{\ln q - \mu}{\sigma}\right)^2} & q > 0 \\ 0 & q \leq 0 \end{cases}, \quad (1.3)$$

which is known as the lognormal distribution denoted by  $\mathcal{L}(q|\mu, \sigma^2)$  or  $\mathcal{L}(\mu, \sigma^2)$  bearing in mind that  $\mu$  and  $\sigma$  are parameters for the corresponding normal distribution of  $\ln q$ . The

mean and width of lognormal distribution are given by

$$\mu_q = e^{(2\mu + \sigma^2)} \quad \text{and} \quad \sigma_q = \mu_q \sqrt{e^{\sigma^2} - 1} \quad (1.4)$$

in terms of  $\mu$  and  $\sigma$ , which here take the role of two parameters. It is interesting to note that no detailed information is needed about the distributions pertaining to the individual steps, that is of the  $a_i$ , since the final result will always approach the lognormal as long as the central-limit theorem holds. The lognormal distribution, which is more peaked and has a longer tail than both the negative binomial and the gaussian, has been found applicable in a number of different contexts. For example, the distribution of abundances of various species in population ecology is well fitted, and the variations of the productivity of individuals in research follow a lognormal distribution, as also do the observed distributions of income and wealth in some economies. The essential point for all these applications is that the outcome is a product of many random factors, rather than a sum, and hence a lognormal distribution takes place instead of a normal one.

### Stochastic Growth Theory

Stochastic Growth Theory (SGT) is a theory for explaining bursty waves with widely varying fields that persist with the associated particle distributions far from their source (e.g. Robinson, 1992, 1993). Plasma theory has long recognized the tendency for wave-particle interactions to lead a system toward marginal stability (e.g. Stix, 1962), so the wave emission and damping are balanced. SGT describes a self-consistent interaction between particle distribution and waves in an inhomogeneous plasma and the evolution to a state in which (i) the particle distribution is close to time and volume averaged marginal stability but with stochastic fluctuations that (ii) cause the wave gain  $G$  to vary stochastically in time and space. The gain  $G(t)$  at time  $t$  is defined by

$$G = \int_{-\infty}^t dt' \Gamma(t') \quad (1.5)$$

and is related logarithmically to the electric field  $E(t)$  by

$$G = \ln \left( \frac{E(t)}{E_0} \right), \quad (1.6)$$

where  $\Gamma(t')$  is the linear growth rate at time  $t'$  and  $E_0$  is a reference field strength.

The hypothesized random walk in  $G$  and the logarithmic relation between  $E(t)$  and  $G(t)$  provide an immediate and natural qualitative explanation for the burstiness and widely varying nature of the wave fields. Similarly, the closeness to marginal stability provides an immediate qualitative explanation for the persistence of the waves and unstable particle distribution far from the source of the unstable distribution. In contrast, the “uniform secular” model for wave growth in plasmas (e.g. Stix, 1962), of homogeneous exponential “linear” growth with constant growth rate until saturated by nonlinear processes, encounters major problems explaining the burstiness and widely varying fields of the waves and the persistence of the waves and driving distributions that are characteristic for space plasmas (Robinson *et al.*, 1993). SGT is formulated as a general theory, which can potentially apply to arbitrary combinations of wave modes, free energy source, and inhomogeneous background plasma that satisfy hypotheses (i) and (ii) above. The detailed route by which a given system evolves to an SGT state presumably depends upon the system. However, the qualitative physics is supposed to be as follows: preexisting inhomogeneities in the plasma cause wave growth to be more effective in some regions than the others, this wave growth induces

spatiotemporal fluctuations in the driving particle distribution by quasi linear relaxation, and the resulting interactions of the fluctuating particle distribution and waves in the inhomogeneous background plasma lead to the waves and particles evolving to an SGT state. Next, consider the relation  $E(t) = E_0 \exp G(t)$  from (ii) and rewrite the integral Eq. 1.5 as a sum  $G(t) = \sum_i \Delta G_i = \sum_i \Gamma \Delta t_i$  over multiple successive fluctuations  $\Delta G_i = \Gamma_i \Delta t_i$  of the wave gain, the growth rate, and the particle distribution function. Then, requiring only that sufficiently many fluctuations in  $\Delta G_i$  occur during some characteristic time, the Central Limit Theorem provides  $G(t)$  to be a gaussian random variable as assumed in hypothesis (ii), irrespective of the particular distribution of the fluctuations  $\Delta G_i$ . Thus, since hypothesis (i) is justified by the tendency for all unstable wave-particle systems to approach marginal stability, the qualitative physical justifications for the SGT hypotheses are simple and natural. Accordingly, SGT has the potential to be widely applicable.

SGT is a statistical theory and hence the relevant theoretical quantities and associated observational and theoretical tests involve the statistics of the waves and driving particles. Examples are the probability distributions  $P(G)$  and  $P(\log E)$  of  $G$  and  $\log E$ , respectively. For pure SGT systems, in which thermal waves and nonlinear processes can be neglected, the Central Limit Theorem predicts that  $P(G)$  and  $P(\log E)$  should be gaussian in  $G$  and  $\log E$  respectively:

$$P(\log E) = \frac{1}{\sqrt{2\pi}\sigma} \times \exp\left[-\frac{1}{2} \frac{(\log E - \mu)^2}{\sigma^2}\right], \quad (1.7)$$

where  $\mu$  and  $\sigma$  are the mean and standard deviation of  $\log E$ . This is the simplest, most fundamental test for SGT which is easily amenable to observational testing.

The observed electric field of the type III Langmuir waves (LW) appears to be very spiky and bursty with time. In order to explain this property, Robinson (1992, 1993) developed a theory (the so called stochastic growth theory – SGT) in which the Langmuir waves growth rate is assumed to fluctuate randomly. This hypothesis is based on the fact that waves and electrons are interacting in an inhomogeneous plasma environment. Assuming that the effective number of growth rate fluctuations undergone by a given wave is large enough, the central limit theorem can be applied to the probability distribution function of the field. A consequence of the SGT is thus that the probability distribution of the logarithm of wave energy density should be normal. In order to verify this strong assumption, Robinson *et al.* (1993) performed a fitting of the Langmuir waves spectral power density recorded by the ISEE 3 spacecraft during several *in situ* type III events (see Figures 5 and 6 in Robinson *et al.* (1993)). Although the authors claimed a good agreement with a lognormal distribution for the Langmuir waves power, their conclusions are not fully convincing. The main reason is that the fit of the observed power distributions, which was performed without removing the background (instrumental and natural) levels, was only valid for the large values of the power, at and above the mean values of the power distributions.

Indeed when examining whether Langmuir waves in the Earth’s electron foreshock satisfy SGT, electric fields observed *in situ* by the CLUSTER spacecraft have been statistically analyzed by Krasnoselskikh *et al.* (2007) and Musatenko *et al.* (2007). These authors have shown that the observed distributions for the logarithm of the wave intensities or power spectral densities (PSD) belong to the Pearson system of distributions (Pearson, 1895) rather than being normal. They concluded that the disagreement with the SGT prediction could be the result of an insufficient number of amplifications/dampings in typical Earth’s electron foreshock conditions, so that the central limit theorem can not be applied.

The aim of the study is to perform an extensive statistical analysis of the locally generated Langmuir waves that are associated with the *in situ* observations of type III solar radio bursts. For this purpose all the 16 years Wind observations were examined, from the

end of 1994 to the beginning of 2010, during periods when the spacecraft was far from the Earth's bow shock. By using strict selection criteria and a careful analysis, we produce a high-quality data base consisting of 36 events. This dataset is numerous enough to allow statistical studies such as, for instance, the variations of the observed Langmuir waves properties with ambient solar wind conditions or with the characteristics of the energetic electron beams that generate them.

# Langmuir Waves Distribution

---

## Contents

---

<b>2.1</b>	<b>Observations and Sample Events Selection</b>	<b>25</b>
<b>2.2</b>	<b>Stochastic Growth Theory Predictions</b>	<b>28</b>
<b>2.3</b>	<b>Applying Pearson's System of Distributions</b>	<b>34</b>
<b>2.4</b>	<b>Effect of the TNR Instrument</b>	<b>38</b>
2.4.1	The input distributions for the Langmuir waves amplitudes	38
2.4.2	The TNR instrumental transfer function and integration time	41
2.4.3	Simulations of the TNR response to various input distributions of the Langmuir waves power	43
<b>2.5</b>	<b>Conclusions</b>	<b>49</b>

---

## 2.1 Observations and Sample Events Selection

In this study we use the measurements obtained by means of four different experiments onboard the Wind spacecraft, a laboratory for long-term solar wind measurements, launched on 1 November 1994 (Harten and Clark, 1995). The Wind spacecraft is placed in the solar wind, often near the L1 Lagrangian point about 200 Earth radii in the sunward direction of Earth. The radio and electric field observations that we use, and that are the main focus of this work, have been obtained by the WAVES experiment (Bougeret *et al.*, 1995). On this instrument the locally generated Langmuir waves are recorded by both the Time Domain Sampler (TDS) module, which captures short waveform snapshots of the waves electric field; and by the Thermal Noise Receiver (TNR), which performs onboard spectra of the electric fluctuations in a large frequency domain including the local  $f_p$ . While the TDS transmits to ground, due to telemetry allocation issues, only a small part of the Langmuir waves snapshots that are observed (generally the most intense ones), the TNR records them in the spectral domain and transmits them continuously.

The TNR is a double multi-channel receiver covering the frequency range from 4 kHz to 256 kHz in 5 logarithmically-spaced frequency bands. Each band covers 2 octaves with one octave overlap. Each of these bands is divided into either 32 or 16 logarithmically-spaced channels. TNR provides rapid measurements of the plasma electric field fluctuations.

In the radio domain, where the electromagnetic type III bursts are observed, we use data from the RAD1 and RAD2 radio receivers. The RAD1 frequency range, from 20 to 1040 kHz, is divided into 256 linearly spaced channels of 3 kHz bandwidth each. The frequency range of the RAD2 radio receiver, from 1075 to 13825 kHz, is divided in the same number of channels as RAD1, but with 20 kHz bandwidth.

For the selection of a sample event we use, in addition to the WAVES data: (1) one minute averaged measurements of the interplanetary magnetic field vector in GSE (Geocentric Solar Ecliptic) cartesian coordinates from the Magnetic Field Investigation (MFI), Leping *et al.* (1995); (2) full three-dimensional distribution of suprathermal electrons recorded

by the 3-D Plasma and Energetic Particle (3DP) Investigation, [Lin \*et al.\* \(1995\)](#); (3) solar wind data from the Solar Wind Experiment (SWE), [Ogilvie \*et al.\* \(1995\)](#) which provides three-dimensional velocity, density and temperature of the solar wind protons. All these measurements, taken simultaneously by the four experiments, allow us to perform a qualitative analysis and selection of the events of interest.

The selection procedure was performed very carefully and thoroughly in two phases. The first phase of the selection was a purely visual recognition of the events. In the second phase, proceeding with additional criteria, inadequate events selected in the first phase were eliminated.

Type III solar radio bursts are easily recognizable on dynamical spectra plots such as the one displayed on [Figure 1.3](#). They are intense and have fast, nearly vertical, frequency drifts from higher to lower frequencies. Looking at dynamical spectra we can see sometimes a lot of type III bursts, but only rarely do the generating electrons pass over the spacecraft so that we can observe the Langmuir waves directly, *in situ*. Locally generated Langmuir waves can be recognized as intense narrowband emissions around  $f_p$ . The increase in electrostatic energy around  $f_p$  that persists on dynamical spectra throughout the day varying between approximately 10 and 40 kHz (the typical variation range for  $f_p$  at  $\approx 1$  AU) is due to the quasi thermal noise observed *in situ* ([Meyer-Vernet and Perche, 1989](#)). For the selection we look for times when very sharp intensity increases around the plasma frequency occur at approximately the same time when a type III burst is observed to reach frequencies close to  $f_p$ . [Figure 1.3](#) displays a daily dynamical radio spectrum from the WAVES instrument with several potential event candidates.

In this [Figure](#) several type III bursts can be seen, together with several periods of intensity enhancement around the plasma frequency which is slowly increasing from about 10 to 18 kHz during that day. The criteria that were used in the visual selection of the bursts associated with Langmuir waves were the following: (1) the burst should be isolated in time from other bursts, (2) the intensity of the burst radiation should be much above the background, (3) the burst should be present in a majority of frequencies, (4) series of intense Langmuir waves should start approximately at the same time as the radio burst reaches frequencies close to  $f_p$  and finally (5) the series of Langmuir waves should last at least 10-15 minutes to ensure enough measurements for a statistical analysis. The first criterion ensures that the radio emission is related to a single beam of electrons. The second and third criteria restrict the analysis to those bursts with well defined characteristics of radio flux and frequency drifts. Criteria (1) and (4) ensure that the Langmuir waves are associated with a given burst. Finally criterion (5) ensures that the distribution of the Langmuir wave energy is defined with enough statistics. In the example in [Figure 1.3](#) only one of these bursts can satisfy our visual criteria. It starts at  $\sim 4:30$  UT, and drifts downwards from about 10 MHz to 20 kHz with strong intensification of plasma line, i.e. Langmuir waves, around 11 kHz at  $\sim 5$  UT. The Langmuir waves last about two hours. The second burst at 12 h, although very intense followed by Langmuir waves, does not satisfy the criteria because it is not well isolated (multiple burst), being very weak at higher frequencies. The periods of Langmuir waves enhancements between  $\sim 0$  and  $\sim 4$  UT and between  $\sim 10$  and  $\sim 12$  UT, even if they may be of solar origin, have been dismissed since they do not seem to be directly associated to a radio burst reaching frequencies close to the plasma line.

We apply the above defined criteria to the Wind Waves data recorded from November 1994 to the beginning of 2010. We obtain a subset of about 180 events, in which Langmuir waves and type III bursts occur more or less at the same time. Then we apply another set of criteria that is described below.

For each of the events selected in the first phase, a set of four plots is produced. As an example, the event on 21 October 2002 is shown in [Figure 2.1](#). These four plots summarize

the additional requirements for the selection of events.

Firstly, we calculate the power of the Langmuir waves. For this purpose, we perform the integration of the TNR power spectral density on a frequency interval  $(f_1, f_2)$  encompassing the plasma frequency ( $f_p$ ):

$$P_{LW}(t) = \frac{1}{(\Gamma L_{\text{eff}})^2} \int_{f_1}^{f_2} S(t, f) df, \quad f_1 < f_p < f_2. \quad (2.1)$$

In this expression  $S(t, f)$  is the power spectral density in  $\text{V}^2\text{Hz}^{-1}$  measured by TNR as a function of time and frequency. Typically one TNR spectrum is approximately measured every 4 or 7 seconds. This power spectral density is represented as spectrogram on panel a) in Figure 2.1.  $\Gamma L_{\text{eff}}$  is the Wind dipole reduced effective antenna length the value of which has been taken to 43 meters before collision with a micro-meteorite on 3 August 2000, and to 30.1 meters afterwards (Bale, 2011) [Bale, private communication]. The total electric field power for the Langmuir waves  $P_{LW}$  is therefore given in  $\text{V}^2\text{m}^{-2}$  and is only a function of time. Strictly speaking  $P_{LW}$  is not a power in physical dimensions term. We will however use this denomination as it is commonly done in the literature.

The integration, eq. (2.1), is done numerically by applying a trapezium method.  $f_p$  has been determined using a computer program based on a neural network algorithm developed by Richaume (1996). The frequency interval on which our integration is performed is 10 – 40% of plasma frequency above and below the  $f_p$  depending on how far is type III signature in frequencies (for exact values for each event see Table 2.1). The result of the integration is shown in Figure 2.2, also on panel b) of Figure 2.1. In these figures the sharp peaks with several orders of magnitude in intensity above the smoothly varying background, indicate the locally generated Langmuir emissions. Only those events, where the intensity is much above the background and with enough data points (more than 40-50), are selected for the statistical analysis.

Secondly, in order to see if an increase of the energetic electron flux is associated with the *in situ* type III burst, we have plotted on panel c) of Figure 2.1) omni directional electron energy fluxes in the range from about 30 to more than 500 keV. This energy range has been chosen in order to avoid electrons originating from the Earth bow shock and which have usually lower energies. The electron flux event beginning at 4:30 UT is easily recognizable by its velocity dispersion, with faster electrons arriving earlier, as expected if the electrons of all energies are simultaneously accelerated at the the same point and travel the same distance along the interplanetary field to reach the spacecraft.

Finally in order to be sure that we exclude events caused by foreshock electrons back-streaming from the Earth's bow shock and ensure that the previous analysis is correct, we have calculated the average position of the Earth's bow shock applying Filbert and Kellogg's bow shock model, Filbert and Kellogg (1979). These authors proposed the following simple paraboloid model with rotational symmetry about Earth-sun direction:

$$\frac{x}{14.6} = 1 - \frac{y^2 + z^2}{25.6^2}. \quad (2.2)$$

The coordinates  $(x, y, z)$  are in the Earth's radii expressed in the GSE (Geocentric Solar Ecliptic) coordinate system. The 3-dimensional measurements of the magnetic field are taken from the MFI experiment and the corresponding solar wind velocities from the ion measurements of the SWE experiment. The aberration angle due to Earth's motion with respect to the solar wind–Sun direction is included in calculation, but the solar wind dynamic pressure scaling of the shock model is not included because a precise shape of the bow shock is not relevant/necessary for the analysis. We have calculated the distance,

$A$ , which is a measure of how far from the Earth should be the nose-cone point (vertex) of the paraboloid, in the case when the magnetic field line passing through the spacecraft is the tangent of the paraboloid. Values of  $A$  greater than 14.6 Earth's radii (position of the vertex of the modeled paraboloid along  $x$ -axis) indicate that the spacecraft is far from being connected to the Earth's bow shock. The distance  $A$  is represented on panel d) in Figure 2.1 and the dotted red line indicates  $A = 14.6$  Earth's radii.

At the end of our selection process, after an initial visual inspection and after rejecting all those events that do not meet additional requirements we have set, a total of 36 high-quality events remained to be analysed. The list of these events is given in Table 2.1.

**Explanation of Table 2.1:** Calendar date is represented in the form YYYYMMDD (year, month, day), approximate starting time (UT),  $t_1$ , and approximate ending time (UT),  $t_2$ , of Langmuir waves in the form hh (hour). In the next 3 columns are: approximate plasma frequency,  $f_p$  and frequency interval for the integration (Eq. 2.1),  $f_1$  and  $f_2$ . The next column presents the modulus of the solar wind velocity vector in GSE coordinates from the SWE instrument obtained as an average over time of the event duration,  $V_{SW}$ .  $T_e$  and  $n_e$  are electron temperature and electron number density from 3DP key parameters averaged over the event duration.

**Explanation of Table 2.2:** Calendar date is represented in the form YYYYMMDD (year, month, day). The number of points that remain after the background removal is denoted  $n$ . The type of Pearson's distribution, T, is followed by two dimensionless parameters of the distribution: square of skewness,  $\beta_1$ , and kurtosis,  $\beta_2$  (Eq. 2.7). The next 4 columns present quantiles of cumulative distribution and corresponding values of  $P_{LW,t}^0$ . The first is:  $q^{\max}$  – quantile for  $\log(P_{LW,t}^0)$  value where maximum of the probability distribution occurs. The next three columns present  $\log(P_{LW,t}^0)$  for quantiles  $q^{\max}$ ,  $q = 0.1$  and  $q = 0.9$ , respectively.

**Explanation of Fig. 2.1:** Wind observations extracted from Fig. 1.3 in the time interval from 4.5 to 7.0 h encompassing the data when Langmuir waves occur: a) dynamical spectra, only TNR receiver observations (4–256 kHz), b) power spectral density integrated over a narrow frequency band (8–40 kHz) around the plasma frequency ( $\sim 12$  kHz), c) omni directional spectrum of energetic electron fluxes, 3DP experiment. The energies are indicated on the right-hand side of the panel (the units on the left-hand side of the panel are  $(\text{cm}^2 \text{s keV sr})^{-1}$ ), d) energetic electron flux ratio  $F(0^\circ < \vartheta < 40^\circ)/F(140^\circ < \vartheta < 180^\circ)$  where  $\vartheta$  is pitch angle, e) magnetic field intensity. The color of "+" symbols indicates the direction of the magnetic field vector from the Sun (red) or from the Earth (blue). The solid and dashed lines indicate two spherical coordinates  $(\vartheta, \varphi)$ , respectively, f) parameter  $A$  of Filbert and Kellogg's model of the Earth's bow shock. The red dotted line indicates the distance along  $x$ -axis from the Earth to the nose-cone (vertex of the paraboloid) of the Earth's bow shock in steady state. If  $A$  is greater than 14.6 Earth's radii, it means that Wind spacecraft is outside of the Earth's bow shock.

## 2.2 Stochastic Growth Theory Predictions

The burstiness of the *in situ* Langmuir waves electric field has been observed for a long time, during type III bursts or in the electron foreshock. Theories have been developed to reproduce the observations, based, as initially proposed by Melrose (1990), Muschietti (1990), Robinson (1992) for example, on the fact that the presence of large scale density fluctuations in the solar wind could strongly modify the interaction processes between the beam and the plasma waves. The idea is that the random density fluctuations induce changes in the wave vector  $\mathbf{k}$  of the waves, resulting in a diffusion of the wave-field in  $\mathbf{k}$ -

**Table 2.1:** List of sample events.(Explanation of the Table see on p. 28.)

No.	Date	$t_1$ [h]	$t_2$ [h]	$f_p$ [kHz]	$f_1$	$f_2$	$V_{\text{SW}}$ [km s <sup>-1</sup> ]	$T_e$ [eV]	$n_e$ [cm <sup>-3</sup> ]
1	19950306	09.80	10.80	17.5	16	22	538	8.36	4.86
2	19950402	11.75	12.75	24.0	20	30	360	7.62	8.12
3	19950402	15.05	15.50	24.0	20	30	355	7.51	7.68
4	19971104	06.90	08.10	28.0	21	36	328	7.87	9.39
5	19971123	10.65	11.60	22.5	18	26	502	7.49	9.00
6	19971123	14.50	15.50	15.0	10	20	475	4.89	9.70
7	19980712	00.30	01.90	14.5	11	19	384	4.69	12.44
8	19980712	01.95	02.83	13.5	10	19	384	4.46	12.52
9	19980712	06.50	07.00	23.0	19	30	405	6.34	11.62
10	19980712	08.90	09.65	21.0	19	26	407	6.10	11.32
11	19980712	16.95	17.38	16.5	10	20	420	4.91	11.59
12	19980713	12.05	12.75	25.5	20	40	374	5.75	11.21
13	19980906	07.05	08.20	28.0	16	30	350	8.60	12.08
14	19990129	15.80	16.60	24.5	20	30	400	3.97	2.82
15	19990613	02.52	03.15	16.0	12	20	391	3.14	25.04
16	19990613	06.00	06.50	17.0	13	21	385	3.16	25.27
17	19990618	12.70	14.60	23.0	20	31	383	3.94	24.84
18	19990618	15.50	17.10	23.5	20	30	375	3.91	25.24
19	19990629	13.00	14.90	10.0	06	16	540	3.05	25.52
20	19990919	14.90	15.05	18.5	16	25	391	3.13	24.81
21	20000404	15.80	16.40	27.0	21	31	380	3.96	25.43
22	20000504	11.49	11.67	20.0	16	25	465	3.11	23.82
23	20000515	17.48	17.73	23.5	20	30	379	3.49	26.09
24	20000617	03.70	04.55	18.0	16	21	480	3.44	25.85
25	20020322	11.65	13.35	22.0	16	30	440	3.60	23.62
26	20021019	22.05	23.05	14.0	08	20	650	3.23	20.51
27	20021020	14.50	16.00	13.5	08	18	650	3.16	20.26
28	20021021	04.50	06.90	12.0	08	18	583	3.18	20.20
29	20021212	13.35	15.20	21.5	17	28	362	4.10	19.70
30	20030123	03.03	03.18	21.0	16	26	618	3.83	19.42
31	20030331	04.75	06.15	18.0	10	24	630	3.42	20.89
32	20030401	00.75	02.65	24.0	10	20	520	3.33	19.87
33	20040605	07.20	08.55	23.5	20	30	449	3.81	17.25
34	20040627	16.04	16.40	20.0	16	25	318	3.61	17.14
35	20040829	03.55	04.14	17.5	16	24	416	3.16	16.73
36	20050316	20.65	21.43	22.0	16	29	376	4.55	15.84

**Table 2.2:** List of sample events, continuation. (Explanation of the Table see on p. 28.)

No.	Date	$n$	T.	$\beta_1$	$\beta_2$	$q^{\max}$	$\log(P_{LW,t}^0)$ for quantiles:		
							$q^{\max}$	$q = 0.1$	$q = 0.9$
1	19950306	58	I	0.21	2.50	0.66	-9.49	-11.80	-8.73
2	19950402	276	I	0.23	3.08	0.58	-9.63	-11.75	-8.44
3	19950402	71	I	0.49	3.07	0.31	-11.34	-12.06	-8.79
4	19971104	413	I	0.13	2.73	0.57	-8.85	-11.01	-7.56
5	19971123	96	XI	0.01	3.02	0.50	-11.03	-12.78	-9.30
6	19971123	198	I	0.07	2.31	0.41	-10.87	-12.33	-8.32
7	19980712	348	IV	0.11	3.33	0.46	-11.35	-12.39	-9.98
8	19980712	347	I	0.01	2.67	0.52	-9.60	-11.44	-8.03
9	19980712	84	IV	0.55	4.37	0.42	-11.64	-12.50	-10.12
10	19980712	42	XI	0.04	2.70	0.50	-11.13	-12.49	-9.78
11	19980712	44	I	0.00	2.26	0.49	-12.00	-13.26	-10.69
12	19980713	111	IV	0.09	3.97	0.47	-11.01	-12.07	-9.73
13	19980906	145	I	0.00	2.51	0.48	-11.61	-13.21	-9.89
14	19990129	192	I	0.16	2.76	0.42	-11.50	-12.87	-9.15
15	19990613	75	I	0.21	2.75	0.39	-11.31	-12.46	-9.00
16	19990613	135	I	0.32	2.72	0.67	-9.14	-12.38	-8.14
17	19990618	58	I	0.85	4.02	0.34	-12.50	-13.13	-10.52
18	19990618	222	I	0.03	2.58	0.46	-10.74	-12.42	-8.67
19	19990629	265	I	0.43	3.20	0.36	-10.75	-11.69	-8.42
20	19990919	46	I	1.22	4.13	0.82	-8.54	-11.13	-8.36
21	20000404	188	I	0.02	2.11	0.57	-9.12	-11.73	-7.49
22	20000504	122	VI	1.60	5.50	0.68	-9.89	-11.76	-9.44
23	20000515	46	I	0.00	1.90	0.56	-10.22	-12.54	-8.56
24	20000617	446	I	0.01	2.46	0.51	-10.07	-12.00	-8.35
25	20020322	338	I	0.07	2.90	0.54	-9.26	-11.11	-7.91
26	20021019	293	IV	0.44	4.86	0.55	-10.19	-11.23	-9.51
27	20021020	460	IV	0.04	3.20	0.47	-10.09	-11.34	-8.62
28	20021021	723	I	0.14	2.57	0.40	-11.09	-12.34	-8.70
29	20021212	436	I	0.08	2.40	0.41	-10.54	-12.17	-7.79
30	20030123	62	I	0.01	2.57	0.52	-11.30	-12.59	-10.19
31	20030331	613	XI	0.03	3.03	0.50	-10.36	-11.93	-8.81
32	20030401	741	XI	0.01	3.05	0.50	-10.47	-12.05	-8.91
33	20040605	240	I	0.26	3.34	0.42	-11.27	-12.57	-9.13
34	20040627	44	I	0.01	1.85	0.59	-11.31	-13.54	-9.97
35	20040829	165	I	0.08	2.54	0.57	-9.63	-11.68	-8.35
36	20050316	539	I	0.04	2.87	0.53	-9.52	-11.32	-8.10

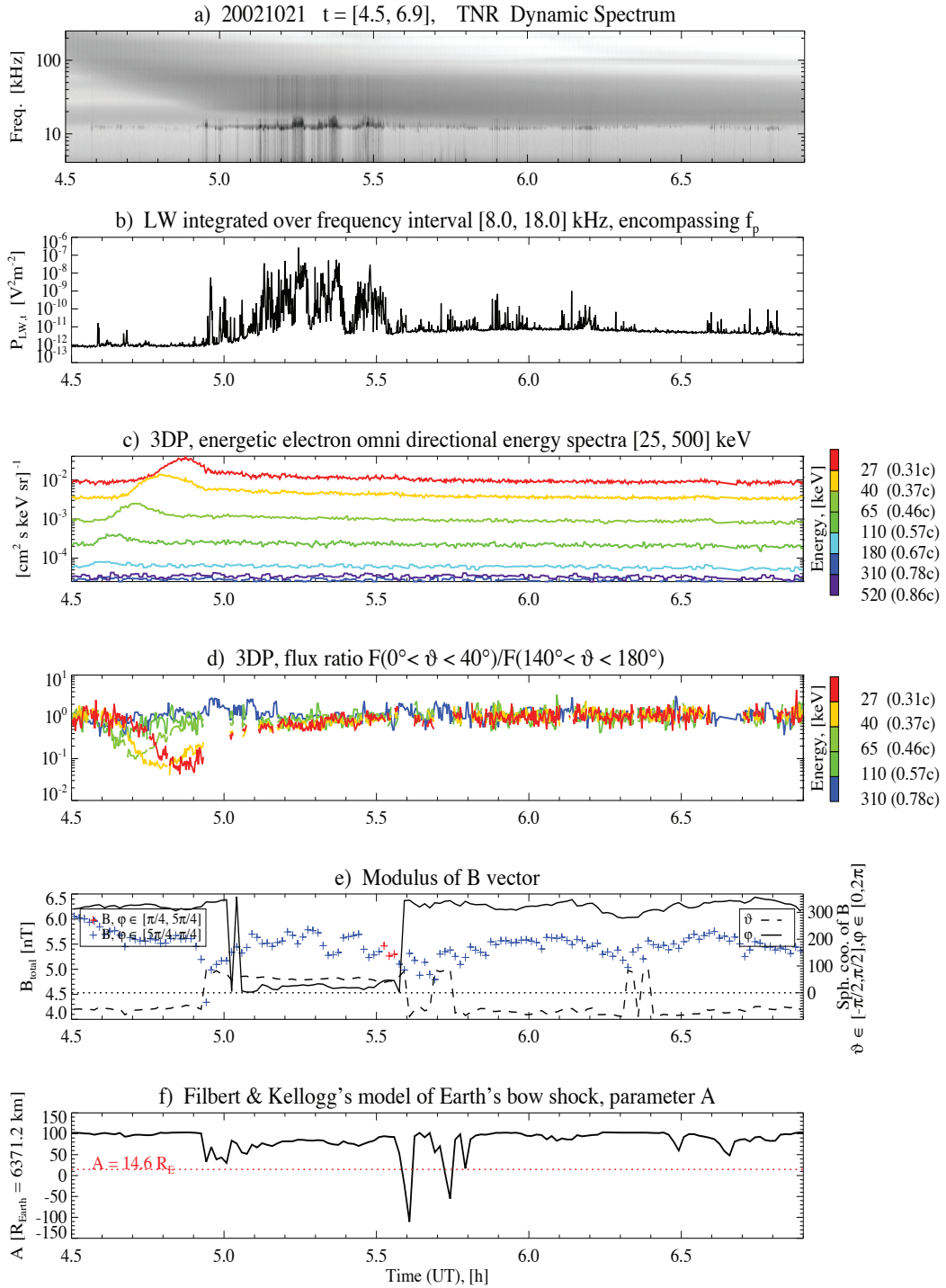


**Figure 2.1:** Wind observations extracted from Fig. 1.3 in the time interval from 4.5 to 7.0 h encompassing the data when Langmuir waves occur “seen” by different Wind experiments. (Explanation of the Figure see on p, 28.)

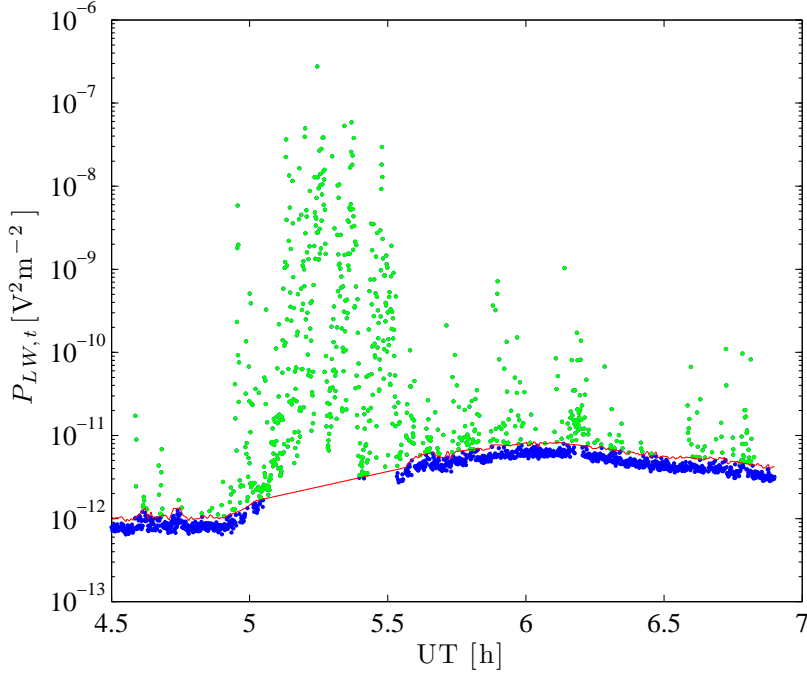


**Figure 2.2:** The power of Langmuir waves obtained by integration of the power spectral density over frequencies from 8 to 18 kHz around the plasma frequency  $f_p = 12$  kHz (21 October 2002 event). The red line separates the power of Langmuir waves (green points) from the background (blue points).

space. If this diffusion happens on a time scale smaller than the inverse wave growth-rate, the waves are scattered out of the beam resonance cone before having the time to grow, and the instability is, on average, suppressed.

Nevertheless, a non-zero probability still exists that some density fluctuations are arranged in such a way that plasma waves can grow on a particular path. Starting from this idea, the stochastic growth theory (see Ch. 1.4 for details), assumes the electric field of the waves to be produced by succession of exponential growth/decays, so that their associated power is

$$P_{LW} = P_0 \prod_{i=1}^N e^{2\gamma_i \Delta t_i}, \quad (2.3)$$

the growth rate of the electric field  $\gamma_i$ , and interaction times  $\Delta t_i$  being random variables. Taking the logarithm of this equation one obtains:

$$\log P_{LW} = \log P_0 + \sum_{i=1}^N 2\gamma_i \Delta t_i. \quad (2.4)$$

Then assuming that the number  $N$  of random interaction is large compared to 1, the central limit theorem can then be applied to the probability distribution  $f(\log P_{LW})$  which is thus a normal distribution (e.g. [Robinson \(1992\)](#)):

$$f(\log P_{LW}) = \frac{1}{\sqrt{2\pi}\sigma} \times \exp \left[ -\frac{1}{2} \frac{(\log P_{LW} - \langle \log P_{LW} \rangle)^2}{\sigma^2} \right], \quad (2.5)$$

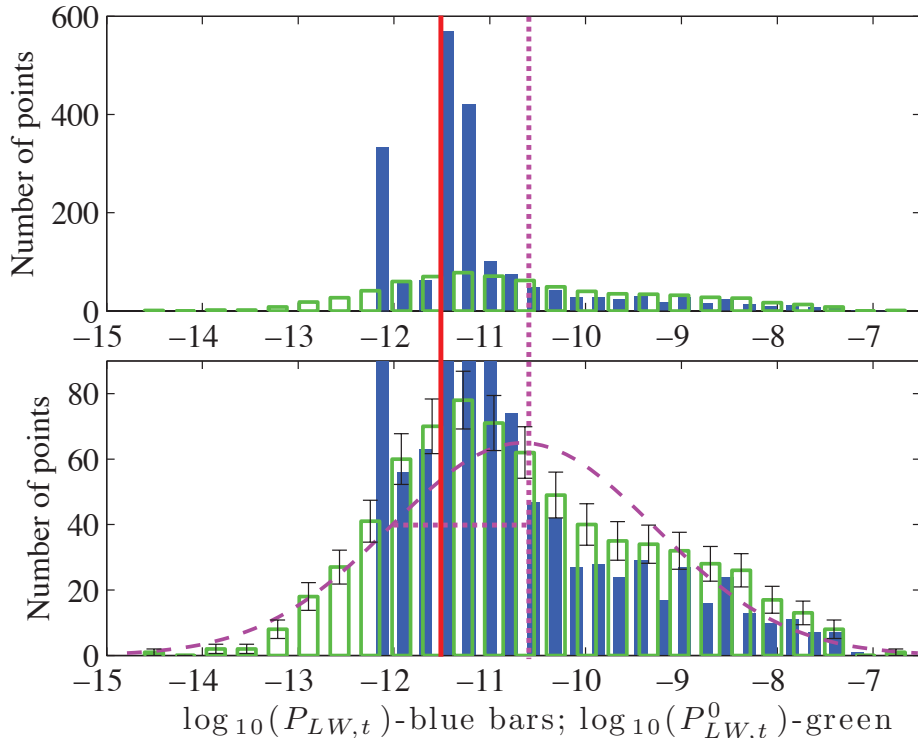


**Figure 2.3:** Histograms of the logarithm of Langmuir waves power (21 October 2002 event). Upper panel: Before (filled blue bars) and after (empty green bars) background removal. Lower panel: part of upper panel, dashed line represents Gaussian fit of the logarithm of Langmuir waves power histogram after background removal. Dotted lines represent parameters of Gaussian distribution: mean  $\mu = -10.6$  and standard deviation  $\sigma = 1.4$ . Vertical red line represent mean of removed background,  $\langle \log(P_{bg}) \rangle = -11.5$ .

where the parameters  $\langle \log P_{LW} \rangle$  and  $\sigma$  are the mean and standard deviation, respectively. The first comparisons between the above SGT prediction and observations were done by Robinson *et al.* (1993). From the Figures 5 and 6 of that article, the authors claim that the distributions of the Langmuir waves spectral power density, recorded by the ISEE 3 spacecraft during several *in situ* type III events, could be well fitted with lognormal distributions. It has to be noted, however, that these fittings were performed without removing the background (instrumental and natural) levels. The good agreement between observations and SGT predictions was therefore only valid for the large values of the power, at and above the mean values of the power distributions. Actually when one performs correctly the same kind of fitting by removing the background, as it is described in the following section, then the resulting distributions have to be fitted with a generalized Pearson's system of probability distributions (Pearson, 1895) and the agreement with the SGT theory is no longer satisfactory.

In order to see if the Langmuir waves associated with type III solar bursts satisfy the predictions of the SGT, we perform the statistical analysis described hereafter.

For each of the 36 events given in Table 2.1, we compute the integral of the TNR

power spectral density on a given frequency interval encompassing the plasma frequency as described by equation (2.1). When doing so, the background of the obtained signal is composed of the slowly varying thermal noise and type III radio emissions that are present over the integration frequency range. As an example of such integration, the event No 28 from Table 2.1 (21 October 2002) is represented in Figure 2.2. This figure illustrates the burstiness nature of the integrated Langmuir waves power  $P_{LW}(t)$  that can vary up to five orders of magnitude above the slowly varying background level. As described previously, it is necessary to remove the background before fitting the distribution of  $P_{LW}(t)$ . A heuristic algorithm for defining this background has been used. This algorithm, which provides the background level represented by the red line in Figure 2.2, is described by a pseudocode in Appendix D.

After subtracting the background noise defined above from  $P_{LW}(t)$ , we obtain  $P_{LW}^0(t)$ , what we consider to be the Langmuir waves power only. Histograms of  $P_{LW}(t)$  and  $P_{LW}^0(t)$  for event No 28 are displayed in the upper panel of Figure 2.3 as filled blue bars and empty green bars, respectively. These histograms have been computed over the whole time interval on which the event is defined (columns 3 and 4 from Table 2.1). The effect of removing the background level can be clearly seen with  $P_{LW}^0$  reaching values lower than those of  $P_{LW}$  by two orders of magnitude. For illustration, a fit of the histogram of  $P_{LW}^0$  with a lognormal distribution is displayed as a pink dashed line on the lower panel of Figure 2.3. On this panel the error bars of the histogram are calculated as standard deviation of counting statistics.

As one can see in Figure 2.3, while a lognormal distribution fits nicely the histogram of  $P_{LW}^0$  for values lower than  $10^{-12} \text{ V}^2\text{m}^{-2}$ , this is not the case for higher values and other functions are needed to better represent the observed histogram of  $P_{LW}^0$ . If a variable is driven by some process that is a product of a number variables, it will have a lognormal distribution (see Subsec. Lognormal distribution, p. 21 for more details), *but*, if some of these factors could be dominant, or correlated, it could lead to distributions with longer tails!

In the next section, we use the more general Pearson family of distributions (Pearson, 1895) providing variety of distribution shapes to perform such a fitting.

## 2.3 Applying Pearson's System of Distributions

When dealing with empirical data with significant skewness and kurtosis, the normal distribution is not the best choice for modeling. The four parameter Pearson's system of distributions is a better choice. It represents a wide class of distributions with a wide variety of shapes and thus provides more accurate representations of the observed data. On the other hand, it includes, as special cases, some well known distributions (normal, beta, gamma, Student's t-distribution etc.). Pearson (1895) defined this distribution system by the following ordinary first order differential equation for the probability density function  $p(x)$ :

$$-\frac{p'(x)}{p(x)} = \frac{b_0 + b_1x}{c_0 + c_1x + c_2x^2} \quad (2.6)$$

where  $b_0$ ,  $b_1$ ,  $c_0$ ,  $c_1$  and  $c_2$  are five real parameters. After normalizing the fraction with any of them, only four independent parameters remain. The form of the solution of this differential equation depends on the value of these parameters, resulting in several distribution types.

The classification of distributions in the Pearson system is entirely determined by the first moment (mean- $\mu_1$ ) and the next three central moments (variance- $\mu_2$ , skewness- $\mu_3$  and kurtosis- $\mu_4$ ). Pearson proposed two dimensionless parameters, i.e. the two moment

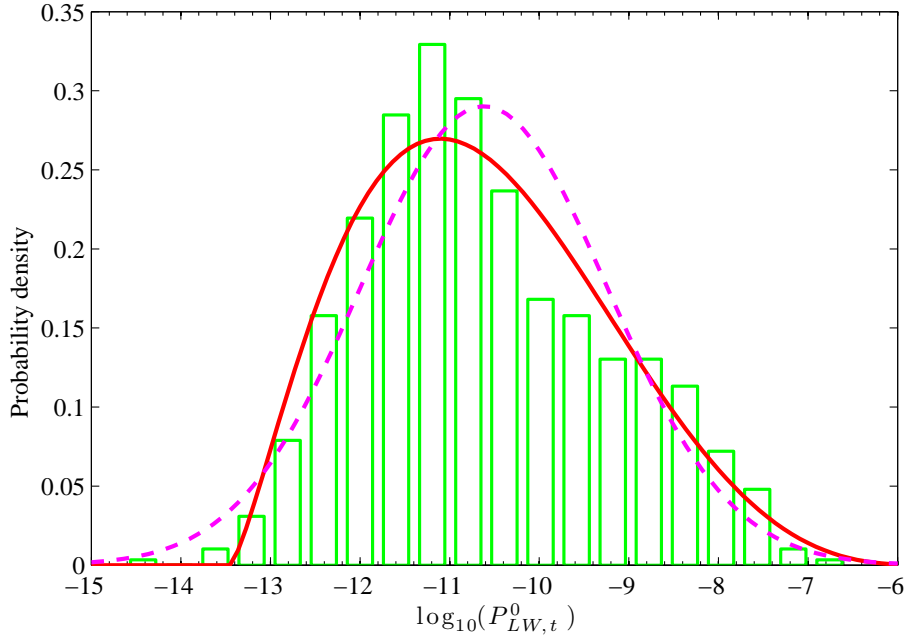


**Figure 2.4:** Pearson type I (solid red line) and normal (dashed line) probability density distribution of the logarithm of Langmuir waves power (21 October 2002 event). Normalized histogram is also shown (green bars).

ratios associated with the square of the skewness ( $\beta_1$ ) and kurtosis ( $\beta_2$ ):

$$\beta_1 = \frac{\mu_3^2}{\mu_2^3}, \quad \beta_2 = \frac{\mu_4}{\mu_2^2}. \quad (2.7)$$

These two parameters characterize the asymmetry and the peakedness of the distribution, respectively, and entirely determine the type of the Pearson distribution system through one parameter,  $\kappa$ , defined as:

$$\kappa = \frac{\beta_1(\beta_2 + 3)^2}{4(2\beta_1 - 3\beta_1 - 6)(4\beta_2 - 3\beta_1)}. \quad (2.8)$$

For  $\kappa < 0$ ,  $0 < \kappa < 1$  and  $\kappa > 1$ , the distributions are called type I, type IV and type VI, respectively. These three cases are known as "the main types" because they occupy areas in the  $(\beta_1, \beta_2)$  space, contrary to the other types which are represented by lines or points. Type III ( $\kappa = \pm\infty$ ) lies on the boundary between type I and type VI. Type V ( $\kappa = 1$ ) lies on the boundary between type IV and type VI. If  $\kappa = 1$ , an additional condition is needed for the classification. The distribution is classified as type II if  $\beta_1 = 0$  and  $\beta_2 < 3$ , type VII if  $\beta_1 = 0$  and  $\beta_2 > 3$ , and as a normal, also known as type XI, if  $\beta_1 = 0$  and  $\beta_2 = 3$ .

When the type of Pearson distribution is specified, all parameters (three or four depending on the type) of the distribution can be determined from the mean, variance, skewness and kurtosis, i.e. from the first four moments. This theoretical result and transformation formulas are given by Nagahara (2004) or by Johnson *et al.* (1994). (The explicit formulas are given in Appendix B.)

The values of the distribution parameters can be estimated from observations through two different procedures. The first one is called the method of moments. For each type of

Pearson distribution, each of the parameters can be expressed as a function of the first four moments of the distribution. For our Langmuir waves histograms we first compute the first four moments, then we determine the type of Pearson distribution according to the value of  $\kappa$  in eq. 2.8, and values of  $\beta_1$  and  $\beta_2$  in eq. 2.7, to which the distribution belongs. Finally we obtain the values of three or four parameters (depending of the type of the distribution) from explicit formulas (Nagahara, 2004).

The other method by which the parameters can be determined is the Maximal Likelihood Estimation method. The parameters of each Pearson distribution type are determined so that they maximize the likelihood function of the sample data. For the maximization of the likelihood function we use the standard Nelder-Mead and Levenberg-Marquardt methods Press *et al.* (2007). The best result, i. e. result with maximal likelihood function, over all types is chosen.

We apply each of the two procedures defined above to the LW power distributions of all of the 36 events from Table 2.1. They both give very similar results. As an illustration, we present in Fig. 2.4 the outcome of such an analysis for the event No 14. The best probability function that yields the best fit of the Langmuir waves power distribution is Pearson I type. A lognormal probability distribution provides clearly a less accurate model for the observations.

We find that our 36 events belong to the "main types" of Pearson's distributions: type I (beta), type IV (not related to any standard distribution) and type VI (beta prime). The positions of all 36 events in the  $\beta_1 - \beta_2$  plane are shown in Fig. 2.5. The areas of different "main" Pearson's distribution types are separated by blue lines. Pearson type I area is additionally separated in three subareas by the red dotted lines corresponding to the unimodal, J-shaped and U-shaped distributions, respectively going from the top to the bottom of the figure. The area under the bottom blue line is impossible area for any of Pearson distributions. Even if most of the events are close to the normal distribution, which is represented by the point  $(\beta_1, \beta_2) = (0, 3)$ , they statistically differ from it.

To check whether the observed Langmuir waves power distributions are really different from a normal distribution we have computed the uncertainties  $\delta_{\beta_1}$  and  $\delta_{\beta_2}$  of their  $\beta_1$  and  $\beta_2$  parameters and verified if the  $(\beta_1 = 0, \beta_2 = 3)$  is included in the  $(\delta_{\beta_1}, \delta_{\beta_2})$  uncertainty ellipse centered at  $(\beta_1, \beta_2)$ .

In order to evaluate the uncertainties  $\delta_{\beta_1}$  and  $\delta_{\beta_2}$  we used two methods: a Monte Carlo simulation and a method of moments (described in Appendix B) proposed by Karl Pearson (Pearson, 1895). The uncertainties calculated by the latter method are greater than the one obtained by the Monte Carlo simulation. We retained therefore the greater values, and the error bars shown in Fig. 2.5 are thus calculated by the method of moments.

When evaluating the uncertainties  $\delta_{\beta_1}$  and  $\delta_{\beta_2}$  for all of our 36 events, we find that for 32 events the point  $(\beta_1 = 0, \beta_2 = 3)$  is not contained within the  $(\delta_{\beta_1}, \delta_{\beta_2})$  uncertainty ellipse of the event. Only 4 out of the 36 events can be considered statistically to be well represented by a lognormal (in linear scale) Langmuir waves power distribution.

For the Langmuir waves background we used a heuristic definition described in Appendix D. As we have seen (Fig. 2.3), variations of determined background levels are reflected only in variations of the far left-side values of the Langmuir waves histogram, while the central and right-side values remain almost unchanged due to the logarithmic scale. In order to examine if our heuristic background determination affects the shapes of the Langmuir waves power distributions we have used the following procedure. We have checked if the variations in the left side of the histogram reflect on the distribution type, i.e. on the position of events on  $\beta_1 - \beta_2$  diagram, we perform the following. From the histogram data points, we have gradually excluded the points from the left side of the histogram. To start with, we excluded all data which were less than  $(\bar{m} - 3\sigma)$ , where  $\bar{m}$  is a mean value, and

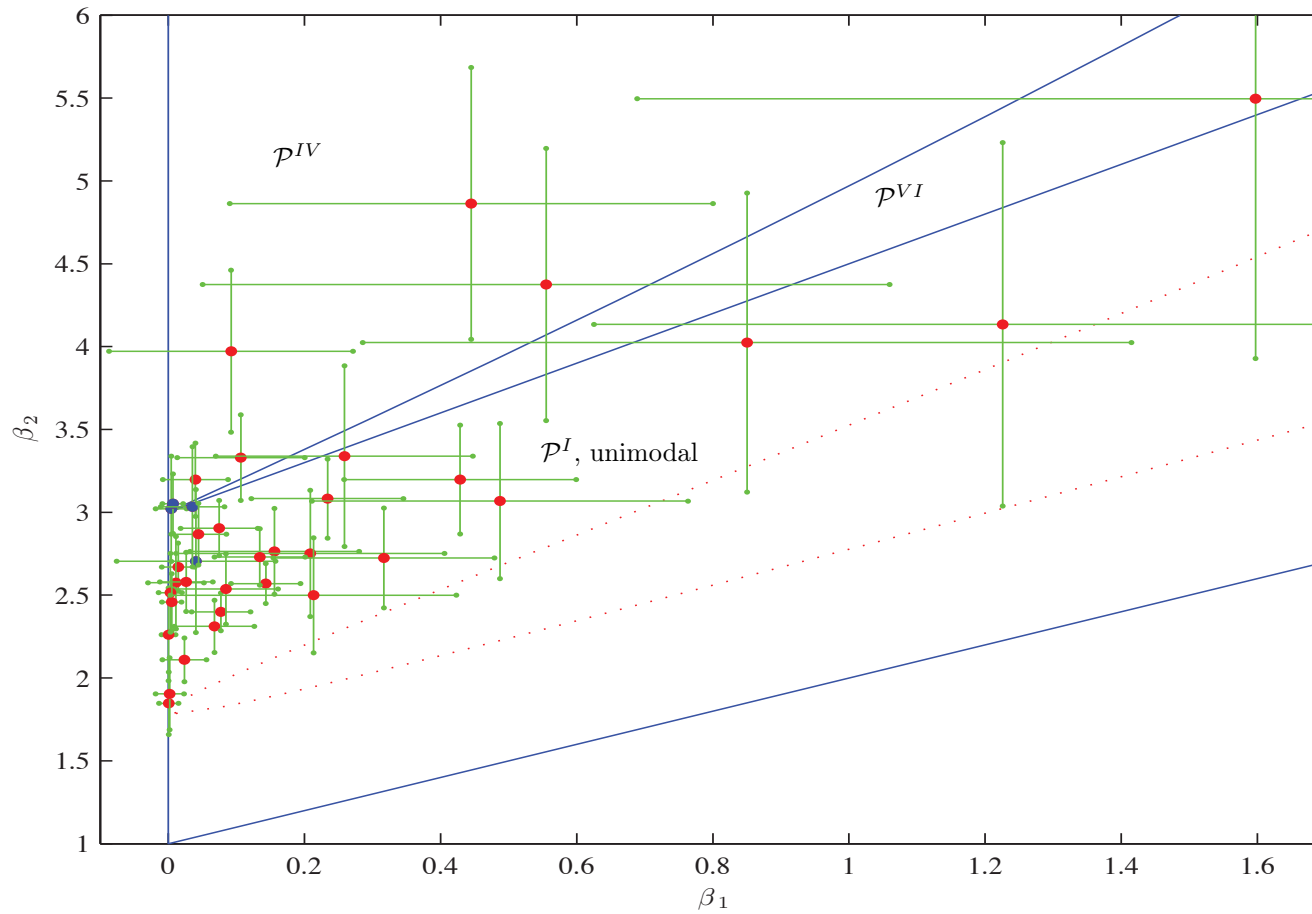


**Figure 2.5:** Beta plane  $(\beta_1, \beta_2)$ . Out of the 36 events: 28 belong to Pearson's type I ( $\mathcal{P}^I$ ), 1 to type VI ( $\mathcal{P}^{VI}$ ) and 7 to type IV ( $\mathcal{P}^{IV}$ ) probability distribution. Only 4 (blue dots) out of the 36 events can be statistically considered to be well represented by a lognormal Langmuir waves power distribution in linear scale (or by a normal in logarithmic scale) – the point  $(\beta_1 = 0, \beta_2 = 3)$ , corresponding to the lognormal distribution, is situated within the  $(\delta_{\beta_1}, \delta_{\beta_2})$  uncertainty ellipse of the event.

recalculated  $\beta_1$  and  $\beta_2$ . The results remained the same: only four events with lognormal distribution, the same ones as for complete histogram points. In the same manner we have recalculated  $\beta_1$  and  $\beta_2$  excluding points less than  $(\overline{m} - 2\sigma)$ , and lastly, less than  $(\overline{m} - 1\sigma)$ . Again, the results remain unchanged - only four events with lognormal distribution. From this analysis we confirm the robustness of the above results and confirm that the variations of determined background levels do not affect significantly the shapes of Langmuir waves power distributions.

It is now well known that the Langmuir waves electric field observed as a function of time during a type III burst or in the terrestrial electron foreshock actually appears as a series of short-duration ( $\sim$  tens of milliseconds) wave packets (Bale *et al.*, 1997; Zaslavsky *et al.*, 2010). These intense wave packets are separated from each other by a time interval difficult to evaluate since the waveform data available onboard the spacecraft are usually limited to samples of  $\sim 100$  ms. The question then naturally arises whether the statistics performed on the electric field spectral power provided by the TNR (and integrated on  $\sim 4$  seconds time-windows) reflects or not the statistics of the amplitude of these wave packets. The answer to this question is crucial for the interpretation of the *in situ* TNR observations of Langmuir waves that has been performed in the previous sections and in a number of previous publications (e.g. Robinson *et al.*, 1993; Cairns and Robinson, 1999).

## 2.4 Effect of the TNR instrumental integration time and transfer function on the LW electric field statistics

In this section, we investigate the question described above by performing numerical simulations of the response of the TNR to series of Langmuir wave packets, and adapt the input parameters in order to recover results similar to the Wind's observation presented above. The results are discussed in the last section (Sec. 2.5).

### 2.4.1 The input distributions for the Langmuir waves amplitudes

As mentioned previously and because of telemetry limitations, there are no measurements available of the actual and precise distributions for the Langmuir waves amplitudes or intensities within *in situ* type III bursts events. The probably best data up to date have been recorded by the Time Domain Sampler (TDS) onboard the Stereo WAVES instruments (Bougeret *et al.*, 2008). The two STEREO TDS provide short snapshots of rapid sampling (up to 250 kilosamples per second) of the three orthogonal antennas electric potentials (see Appendix C).

Typical examples of TDS Langmuir waves snapshot events are displayed in Fig. C.1 in Appendix C. These Langmuir waves waveforms, even though they present different morphologies, are characterized as bursty wave packets which are localized spatially and temporally and which are probably linked to solar wind density fluctuations (Zaslavsky *et al.*, 2010). In Appendix C are described the statistical methods that have been used to retrieve the STEREO TDS distributions of the Langmuir waves snapshots amplitudes and durations within *in situ* type III events.

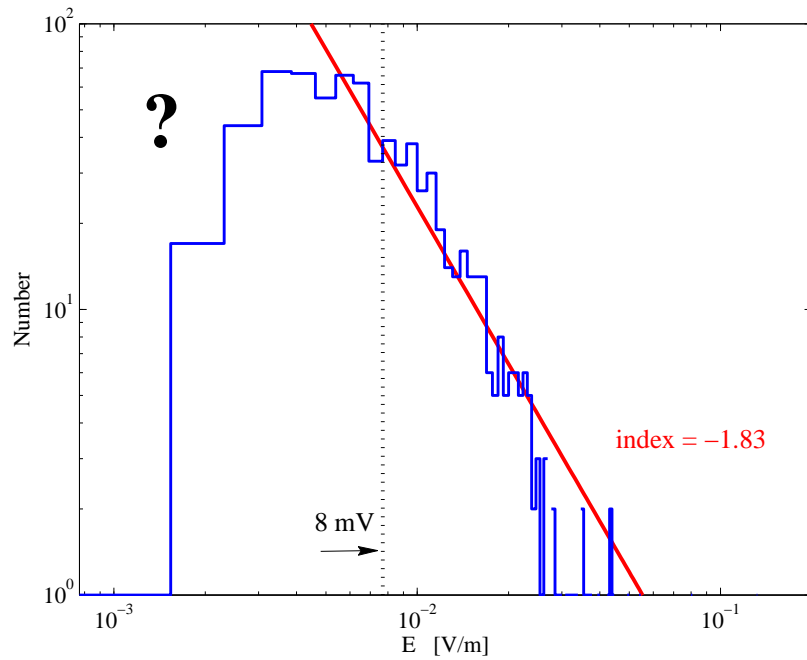


**Figure 2.6:** Distribution of the Langmuir waves amplitudes as they have been recorded by the Time Domain Sampler (TDS) on the STEREO/WAVES instrument. The red line presents the best linear fit in logarithmic scale with an index of -1.83. The values of  $E$  less than 4.6 mV/m were excluded from the fitting procedure. (Figure provided by courtesy of Arnaud Zaslavsky; see Appendix C for more details.)

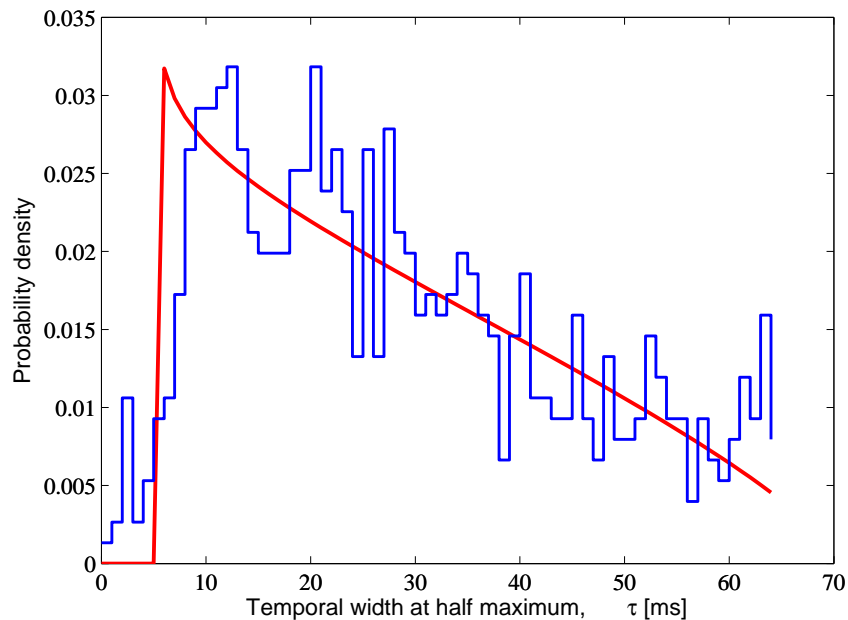


**Figure 2.7:** Distributions of the Langmuir waves snapshots distribution of half maximum height as they have been recorded by the TDS on the STEREO/WAVES instrument. The red line presents the best fit by Pearson type I distribution. (Figure provided by courtesy of Arnaud Zaslavsky; see Appendix C for more details.)

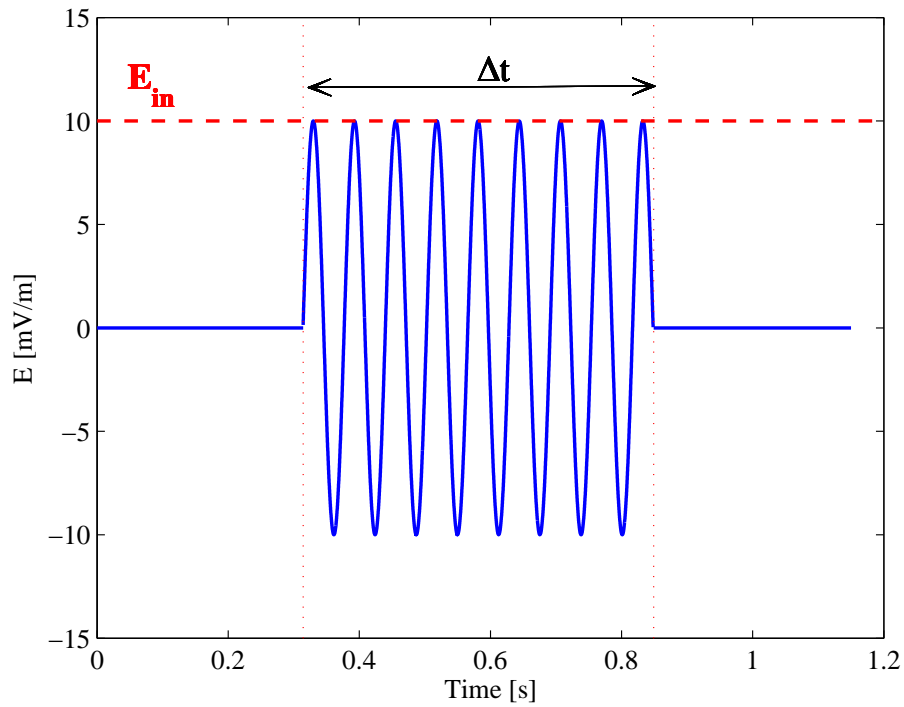


**Figure 2.8:** Monochromatic sinusoidal electric field wave packet injected at the port of the TNR antenna (see text for more details). The signal is defined over a duration  $\Delta t$  shorter than the 1.15 s integration time in band A.

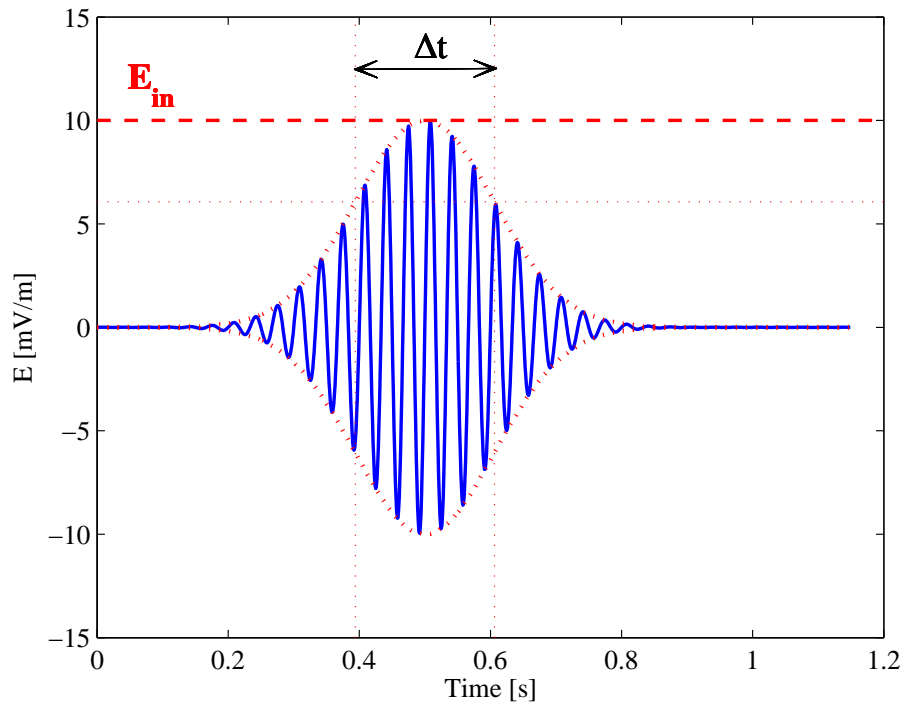


**Figure 2.9:** The same as Fig. 2.8 but the wave packet with a Gaussian envelope as that defined in Eq. 2.9.

Figure 2.6 displays the observed number distribution of the Langmuir waves snapshot amplitudes in  $\text{Vm}^{-1}$ . As described in Bougeret *et al.* (2008), there is a selection criteria for the TDS events which is based on the intensity of the signal. Basically, and depending on the available telemetry, among all the observed TDS waveform snapshots only a few dozen of the most intense ones are transmitted to the Earth. Therefore and because of this selection criteria, the distribution displayed in Fig. 2.6 is not the real one. Only the part of the distributions with amplitudes that are larger than  $\sim 8 \text{ mV m}^{-1}$  are probably close to the reality. The portion of the distribution with amplitudes lower than  $\sim 8 \text{ mV m}^{-1}$  is probably affected by the TDS selection criteria. It is therefore not possible to provide a firm conclusion on the actual Langmuir waves amplitude distributions from STEREO TDS data. The amplitude distribution can as well be fitted by either a lognormal or a Pearson type I or even by a power law for the part of the distribution corresponding to the most intense signals (red line on Fig. 2.6 for which the fitting procedure is described in Appendix C).

Note finally that the amplitudes displayed in Fig. C have not been properly corrected for the orientation between the antenna and the Interplanetary Magnetic Field direction and should therefore be considered as a preliminary result (Zaslavsky, 2012, private communication).

Fig. 2.7 displays the number of observed distributions of the Langmuir waves snapshot durations in milliseconds at half maximum height (see Appendix C for more details). The most probable Langmuir waves snapshot duration is around 10 to 20 ms. Since there is no noticeable correlation between the Langmuir waves snapshot amplitudes and durations (Zaslavsky, 2012, private communication) we can conclude that the distribution is not biased by the TDS selection criteria based on the most intense signals. This distribution can be well fitted with a Pearson Type I function that is represented by the red line in Fig. 2.7 (see more details in Appendix C).

Based on the STEREO TDS observations described above and in Appendix C we model therefore the Langmuir wave electric field  $E(t)$  as a sum of Gaussian wave packets, with random amplitudes, durations, and center time :

$$E(t) = \sum_{i=1}^N E_i e^{-(t-t_{0i})^2/2\Delta t_i^2} \cos(2\pi f_{pi}t + \varphi_i). \quad (2.9)$$

In this equation  $N$  is the total number of wave packets observed over the duration of the simulation  $T_{sim}$ ,  $E_i$  are the electric wave packet maximum amplitudes,  $t_{0i}$  the time on which the wave packets are centered,  $\Delta t_i$  their typical duration,  $f_i$  the frequency of the wave and  $\varphi_i$  the phase of the wave. All of the parameters with an “ $i$ ” index are random variables. According to the Stereo observations the density probability that we should use for  $E_i$  is either lognormal (normal distribution for  $\log E_i^2$ ) or Pearson Type I (Pearson distribution for  $\log E_i^2$ ) or a power law ( $\propto E_i^\beta$ ). The density probability for the  $\Delta t_i$  should be similar to the one displayed in Fig. 2.7. Finally we have used normal distributions for  $f_{pi}$  and  $\phi_i$  and Poisson distribution for  $t_{0i}$ .

### 2.4.2 The TNR instrumental transfer function and integration time

From the electric field  $E(t)$  given by Eq. 2.9, the voltage  $V(t)$  actually measured by the TNR through the antenna effective length  $L_{eff}$  and the receiver gain  $\Gamma$  is

$$V(t) = \Gamma L_{eff} E(t) \cos(\theta(t)) \quad (2.10)$$

where  $\theta(t)$  is the angle between the dipole and the wave electric field. This angle varies significantly as Wind is spinning over a period  $\sim 3$ s. The value of the product  $\Gamma L_{eff}$  is obtained through the calibration of the instrument (Zaslavsky *et al.*, 2011).

As already mentioned, the TNR is a double multi-channel receiver covering the frequency range from 4 kHz to 256 kHz in 5 logarithmically-spaced frequency bands (A, B, C, D & E; see Bougeret *et al.* (1995) for more details). For the 36 *in situ* type III events described in Table 2.1 and 2.2 the typical plasma frequencies are recorded either by the band A of TNR (4 to 16 kHz) or by band C (16 to 64 kHz), each of these bands being divided into 32 logarithmically-spaced frequency channels. For the events studied here, the entire (4 kHz to 256 kHz) TNR spectrum is recorded every 4.4 or 7.36 seconds depending on operational mode of the instrument.

Another characteristic of the TNR receiver is that a wavelet-like transform, using Remez filters, has been implemented onboard the receiver. This has been done instead of a classical Fourier transform scheme, in order to compute the signal power spectral densities with less computational resources (Sitruk and Manning, 1995).

For a broadband and temporally extended signal  $V_{BB}(t)$  the TNR measures the voltage power spectral density in  $V^2/\text{Hz}$ , that is equivalent to the Fourier transform of the autocorrelation function of the voltage:

$$V_f^2 = 2 \int_{-\infty}^{+\infty} \langle V_{BB}(t)V_{BB}(t+\tau) \rangle e^{i2\pi f\tau} d\tau, \quad (2.11)$$

For monochromatic and especially temporally localized signals such as those expected for the Langmuir wave packets (Eq. 2.9) it can be shown that the TNR provides outputs which are affected by the specific transfer function and integration time of the instrument. These outputs are described below with more details.

Typically for an event detected in the band A of TNR, the input signal  $V(t)$  is recorded on a time window  $t_{win}$  every 4.4 or 7.36 sec. If one injects a purely monochromatic sinusoidal wave electric field  $E_{in} \cos(2\pi f_p t)$  with a duration  $\Delta t$  at the port of the antenna, as illustrated by Fig. 2.8, then it can be shown, by implementing the wavelet like transform described by Sitruk and Manning (1995), that the TNR output is given by :

$$v_{out}^2(f) \left[ \frac{V^2}{\text{Hz}} \right] = h(f, f_p) (\Gamma L_{eff})^2 \frac{\Delta t}{t_{win}} E_{in}^2 \left[ \frac{V^2}{\text{m}^2} \right], \quad (2.12)$$

where  $h(f, f_p)$  is a transfer function in  $\text{Hz}^{-1}$  which is due to the use of the Remez filter for the wavelet-like transform.

Integrating this equation over all the TNR frequency channels in the corresponding band and multiplying both sides by  $(\Gamma L_{eff})^2$  yields the total power measured by TNR around the frequency  $f_p$  :

$$v_{out}^2 \left[ \frac{V^2}{\text{m}^2} \right] = H(f_p) \frac{\Delta t}{t_{win}} E_{in}^2 \left[ \frac{V^2}{\text{m}^2} \right], \quad (2.13)$$

where  $H(f_p)$  is a dimensionless normalization coefficient obtained by integrating  $h(f, f_p)$  over the frequency channels.  $H(f_p)$  is slightly varying with  $f_p$  and is roughly equal to 0.3. From this equation it can be seen that the total power is linearly proportional to  $\Delta t$ . In the case when  $\Delta t$  is larger than the Band A integration time (1.15 s every 4.4 or 7.36 s) then one measures the total power  $E_{in}^2$  of the incident wave (only normalized by  $H$ ).

Let assume now that one injects, as illustrated by Fig. 2.9, a single localized monochromatic wave packet with Gaussian envelope similar to those defined by Eq. 2.9. Then it can

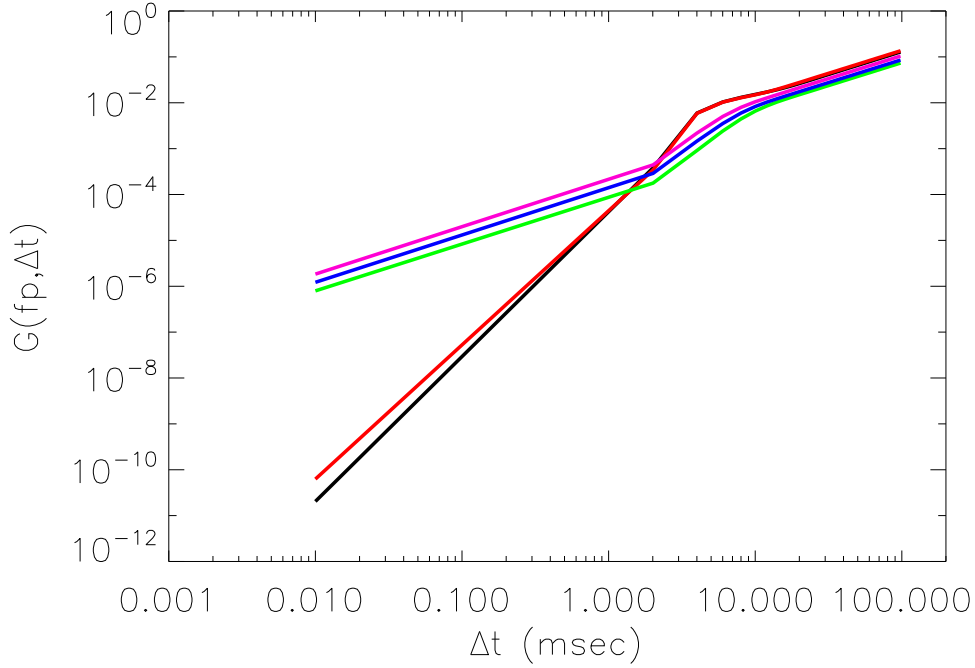


**Figure 2.10:** TNR normalization function  $G(f_p, \Delta t)$  for a single monochromatic wave packet (see text for more details). The black, red, green, blue and magenta lines represent the variations of  $G$  as a function of  $\Delta t$  for  $f_p = 11, 15, 19, 23$  and  $27$  kHz, respectively.

be shown, using a similar procedure as described above, that the total power measured by TNR for this single wave packet is given by :

$$v_{out}^2 \left[ \frac{\text{V}^2}{\text{m}^2} \right] = G(f_p, \Delta t) E_{in}^2 \left[ \frac{\text{V}^2}{\text{m}^2} \right], \quad (2.14)$$

where the normalization function  $G(f_p, \Delta t)$  is displayed in Fig. 2.10. The black, red, green, blue and magenta lines in this Figure represent the variations of  $G$  as function of  $\Delta t$  for  $f_p = 11, 15, 19, 23$  and  $27$  kHz, respectively. For values of  $\Delta t$  larger than 0.1 s,  $G$  tends to the values of  $H$  which are roughly equal to 0.3. (Actually only a few frequency channels around  $f_p$  are sufficient.) Note that the difference between the  $G$  function for 11 and 15 kHz on one hand and 19, 23 and 27 kHz on the other one is due to the fact that the first two frequencies belong to the band A, while the other ones belong to band C.

### 2.4.3 Simulations of the TNR response to various input distributions of the Langmuir waves power

In this section we simulate the TNR response to various input distributions of the Langmuir waves power. As described in the previous section we assume that the input Langmuir wave electric field  $E(t)$  is given by equation 2.9 where  $N$  is the total number of wave packets present over the duration of the simulation  $t_{sim}$ . From the average duration times of the observed 36 Wind events we have set  $t_{sim}$  to be equal to 30 minutes. The total number of wave packets will therefore be  $N = \lambda t_{sim}$  where  $\lambda$  is the rate of wave packets per second

and  $t_{\text{sim}}$  is expressed in seconds. From an examination of STEREO TDS data, described in Appendix C, it appears that there is usually one, sometimes two, Langmuir waves wave packet observed over  $\sim 130$  ms which is the maximum TDS temporal window. This means that the maximum value for the number rate of wave packet per second  $\lambda$  is roughly equal to 10. We have thus performed all our simulations for the four different values  $\lambda = 0.1, 1, 5$  and 10.

Concerning the electric wave packet amplitudes  $E_i$  and according to the previous section, we have used as inputs either lognormal (normal distribution for  $\log E_i^2$ ) or Pearson Type I (Pearson distribution for  $\log E_i^2$ ) or a power law ( $\propto E_i^\beta$ ). Fig. 2.11 displays three examples of the three types input distributions. The distributions have been chosen so that  $E_i^2$  varies over six decades, that is three decades for  $E_i$ . Note also that we have performed several sets of simulations by keeping the same distribution shapes, but by changing the maximum values for  $E_i^2$  or  $E_i$ .

The fitting procedure we have performed is the following. In order to compare with the Wind observations described in Section 2.1 we have performed 36 different simulations of 30 minutes of input data, as defined by Eq. 2.9, for each of the three types (lognormal, Pearson I or power law) of Langmuir waves power distributions and for each of the values of  $\lambda$  described above. For the 36 fittings the  $f_{pi}$  values of Eq. 2.9 have normal distributions centered on the 36  $f_p$  values listed in Table 2.1. Finally, as said previously, the density probability for the  $\Delta t_i$  has been set to the one displayed in Fig. 2.7 and we have used Poissonian distributions for  $t_{0i}$ .

Given the above definitions we have then computed, for each of the  $N$  wave packets defined in Eq. 2.9, the output energy  $v_{out,i}^2$  using Eq. 2.14. Finally, in order to compare with the TNR output, we have averaged these  $v_{out,i}^2$  over the TNR observational windows, that is over  $t_{\text{win}} = 1.15$  s, every 4.4 s. The final output simulation values are named  $V_{out,j}^2$ , distributed all over the 30 minutes of simulation, with a time resolution of 4.4 seconds. The  $V_{out,j}^2$  data points are thus the simulated versions of the observational data displayed in Fig. 2.2 (green points). The number of  $V_{out,j}^2$  data points depends, of course, on  $\lambda$ . When  $\lambda = 10$  there is always at least one Langmuir waves input wave packet in a  $t_{\text{win}}$  interval every 4.4 seconds. In such a case there are 409 ( $30 \times 60/4.4$ )  $V_{out,j}^2$  data points for the output power distribution. For  $\lambda = 0.1$  or 1 there are cases with no input wave packet inside some of the  $t_{\text{win}}$  intervals and there is less than 409 data points for the output. Once we have obtained a simulated set of the  $V_{out,j}^2$  values, we can compute  $P_{LW}^{\text{max}}$  which is the value of  $v_{out}^2$  for which the distribution of all the  $V_{out,j}^2$  is maximum. We can also compute  $P_{LW}^{10}$  and  $P_{LW}^{90}$  which are respectively the 10% and 90% values of the  $V_{out,j}^2$  distributions. Finally we can compute the  $\beta_1$  and  $\beta_2$  values, as defined in Section 2.1, of the  $V_{out,j}^2$  output distributions.

Fig. 2.12 displays a first set of comparisons between the Wind observations and our simulations. For this Figure we have normalized the maximum value of all the input  $E_i$  distributions to the value of  $E_{\text{max}} = 30 \times 10^{-3} \text{ V m}^{-1}$ , which corresponds to the maximum observed value by the STEREO TDS and displayed in Fig. 2.6. The upper panel represent the results for all the lognormal inputs of the Langmuir waves power (in blue), while the middle and the bottom ones represent the results for Pearson (in red) and power law (in magenta) inputs respectively. On these panels the solid lines represent the variation, as a function of the parameter  $\lambda$ , of the median value of the 36  $P_{LW}^{\text{max}}$  values as defined above. For comparison the solid horizontal black line, repeated on all the three panels, corresponds to the median value of the 36 observational Wind  $q^{\text{max}}$  values listed in Table 2.2. The dotted and dashed lines represent the variations of the median values of respectively the 36  $P_{LW}^{10}$  and  $P_{LW}^{90}$  values defined above. The black dotted and dashed horizontal black lines, repeated on all the three panels, represent the median values of the 36 observational Wind 10% and 90% values listed in Table 2.2.

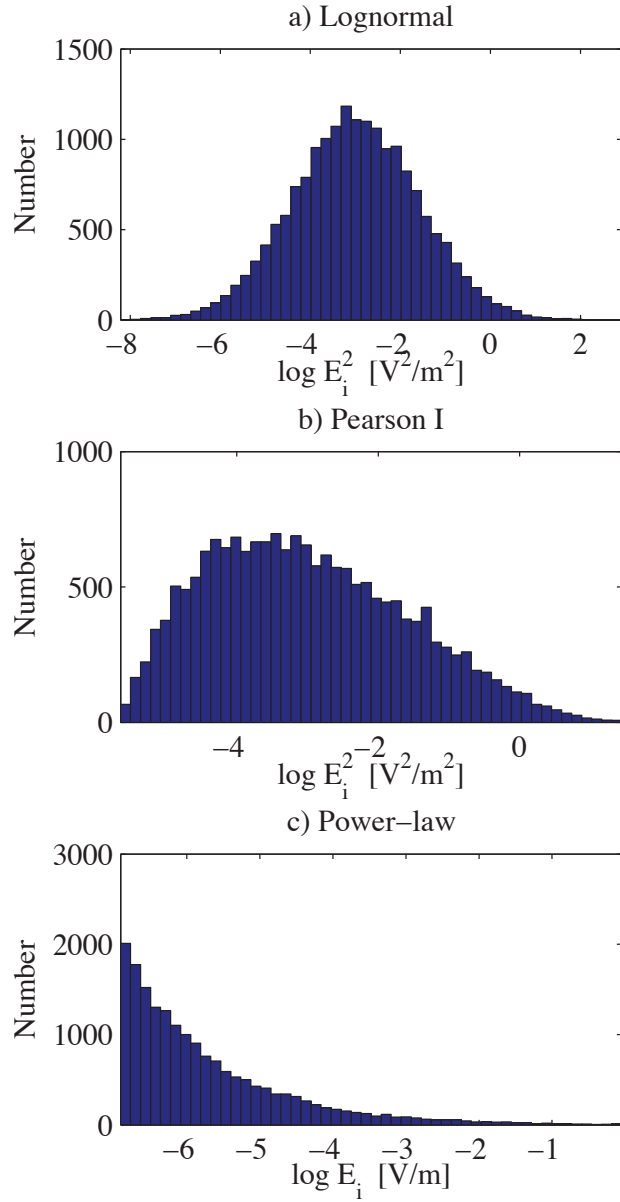


**Figure 2.11:** Distributions of electric wave packet amplitudes  $E_i$  used as simulation inputs: a) lognormal (normal distribution for  $\log E_i^2$ ), b) Pearson Type I (Pearson distribution for  $\log E_i^2$ ), and c) power law ( $\propto E_i^\beta$ ).

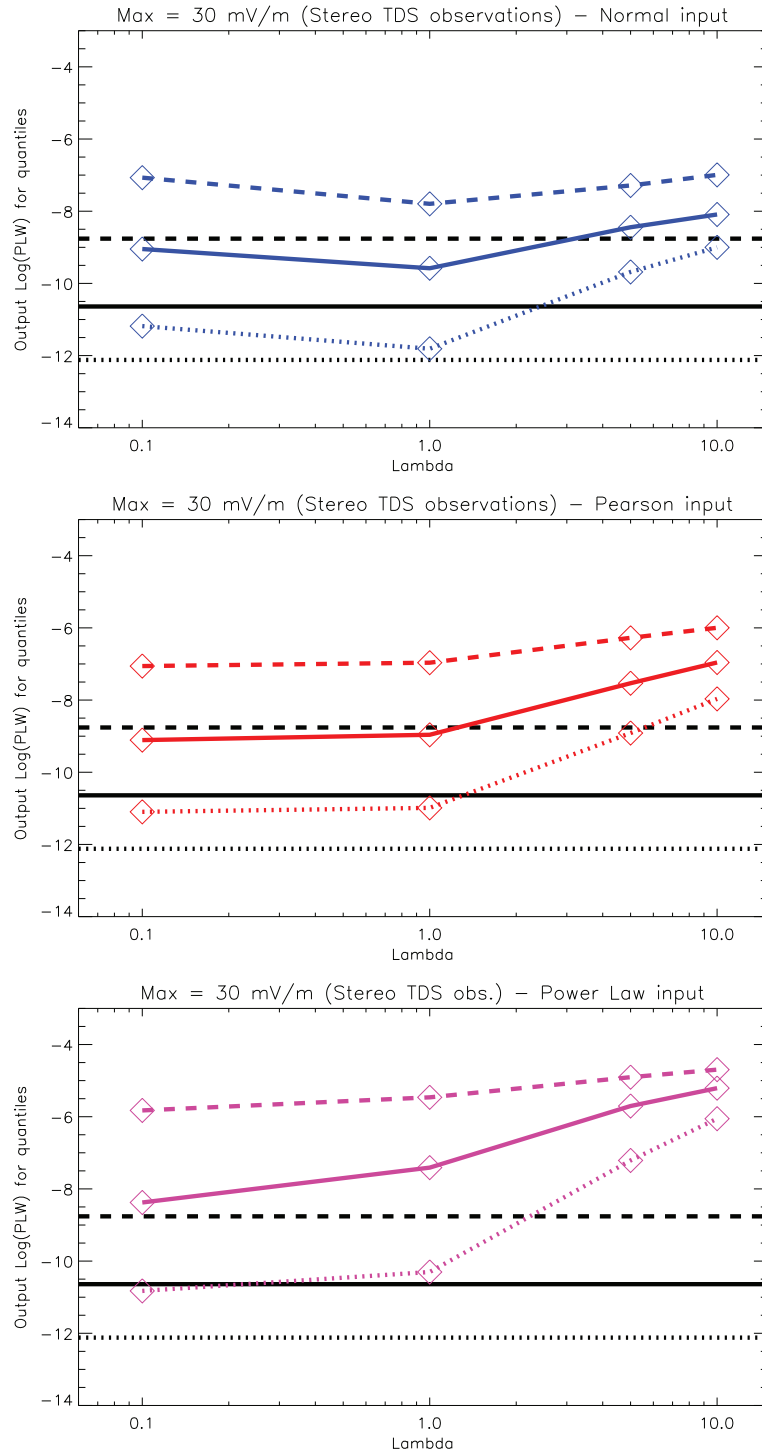


**Figure 2.12:** Comparisons between the Wind observations and our simulations, first set. The maximum value of all input  $E_i$  distributions is normalized to the value of  $E_{max} = 30 \times 10^{-3} \text{ V m}^{-1}$ , which corresponds to the maximum observed value by the STEREO TDS and displayed in Fig. 2.6. The diamonds correspond to the different values of  $\lambda$  included in the simulations ( $\lambda = 0.1, 1, 5$  and  $10$ ). Dotted, solid and dashed lines correspond to the medians of the distribution quantiles  $P_{LW}^{10}$ ,  $P_{LW}^{max}$  and  $P_{LW}^{90}$ , respectively. The black lines are for the actual 36 Wind observations, while the colored lines are for the simulated data with different distributions of electric field input amplitudes ( $E_i$ ) as it is indicated in the titles of the panels.

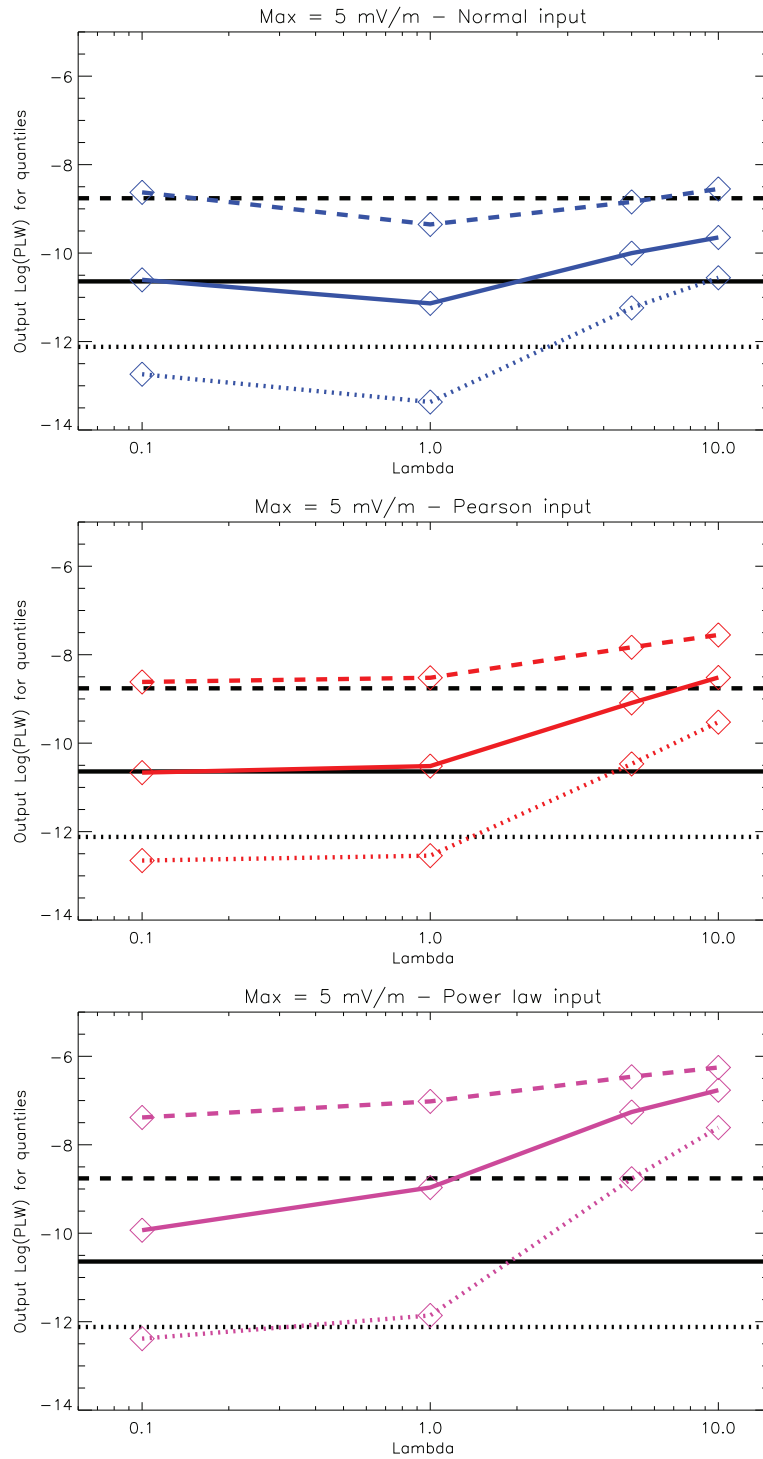


**Figure 2.13:** Comparisons between the Wind observations and our simulations, second set. The same as Fig. 2.12, but the maximum value of all input  $E_i$  distributions is normalized to the value of  $E_{max} = 5 \times 10^{-3} \text{ V m}^{-1}$ .

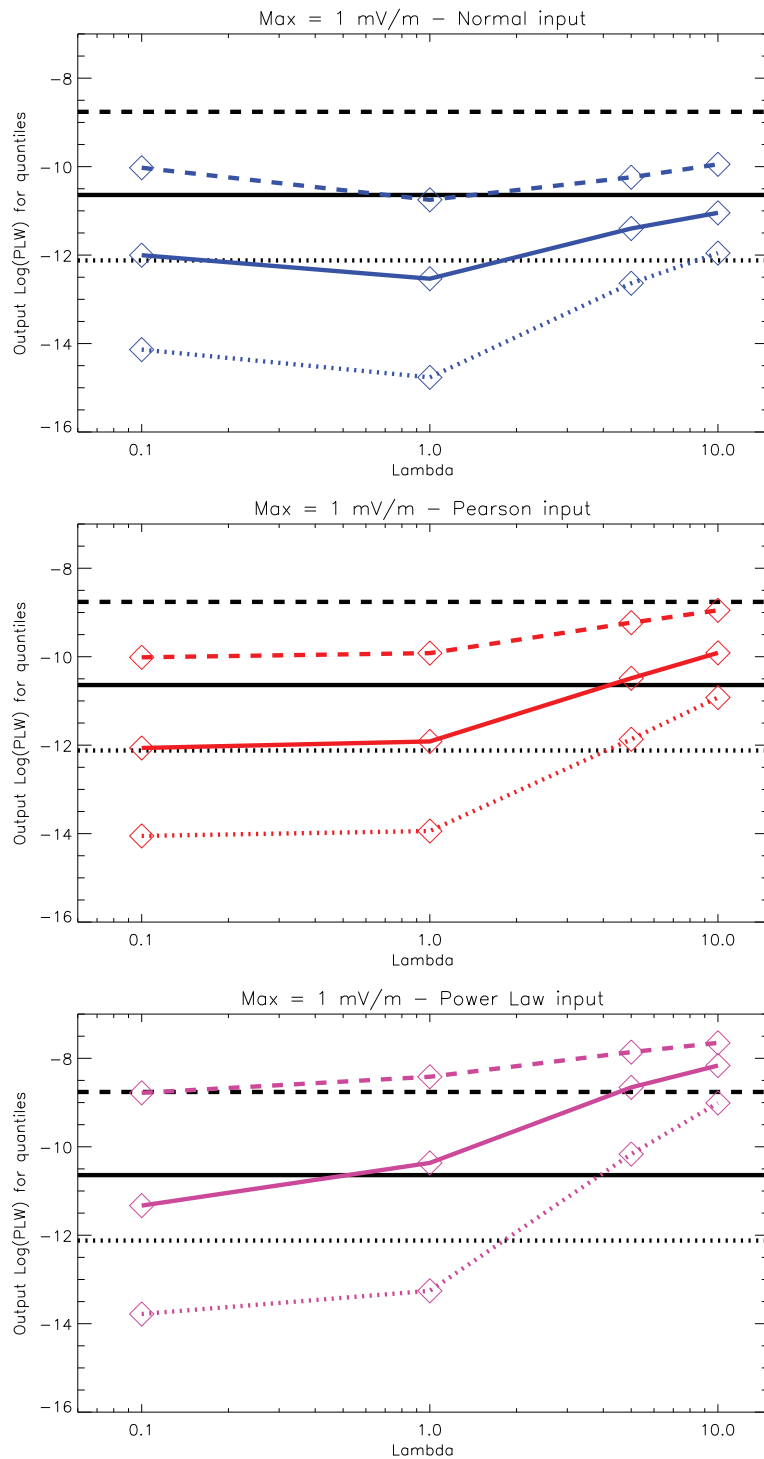


**Figure 2.14:** Comparisons between the Wind observations and our simulations, third set. The same as Fig. 2.12, but the maximum value of all input  $E_i$  distributions is normalized to the value of  $E_{max} = 10^{-3} \text{ V m}^{-1}$ .

Two main conclusions can be made according to Fig. 2.12, which are valid whatever is the type of the input  $E_i$  distribution. Firstly, all of the  $P_{LW}^{10}$ ,  $P_{LW}^{\max}$  and  $P_{LW}^{90}$  values globally increase with  $\lambda$ . This trend is understandable since the more numerous the input wave packets are, the more intense is the output energy from Wind. Secondly, there is no agreement between the  $P_{LW}^{10}$ ,  $P_{LW}^{\max}$  and  $P_{LW}^{90}$  values and Wind 10%,  $q^{\max}$  and 90% observational values. A normalization to  $E_{\max} = 3 \times 10^{-3} \text{ V m}^{-1}$  of all the input Langmuir waves distributions does not seem to fit with the Wind observations.

Fig. 2.13 displays exactly the same kind of information as Fig. 2.12, but with a normalization of all the input  $E_i$  distributions to the value of  $E_{\max} = 5 \times 10^{-3} \text{ V m}^{-1}$ . This time there are values of  $\lambda$  for which there are agreements between the variation ranges of output distributions and the Wind observations. For instance the agreement between the  $P_{LW}^{10}$ ,  $P_{LW}^{\max}$  and  $P_{LW}^{90}$  values and Wind 10%,  $q^{\max}$  and 90% observational values is quite good for  $\lambda = 0.1$  and the lognormal distributions for the input LW power (upper panel). The agreement is also quite good in the case of an input Pearson distribution and for  $\lambda$  ranging between 0.1 and 1. For the case of a power law for the input there is actually no matching for the amplitudes of variations between the simulated outputs and the Wind observations.

Finally, Fig. 2.14 displays exactly the same kind of information as the previous two figures but with a normalization of all the input  $E_i$  distributions to the value of  $E_{\max} = 10^{-3} \text{ V m}^{-1}$ . This time and as for the  $E_{\max} = 30 \times 10^{-3} \text{ V m}^{-1}$  normalization case, there is no agreement between the simulated and the observed Wind outputs.

Another way of comparing the Wind simulated outputs and observations, in addition to comparing the dynamical ranges of the output distributions as we did above, is to compare their shape through the values of their  $\beta_1$  and  $\beta_2$  parameters as defined in Eq. 2.7. The Fig. 2.5 displays the  $\beta_1$ ,  $\beta_2$  values of the observed 36 Wind distributions. The coordinates of the black dot in Fig. 2.15 (in all four panels) represent the median values of  $\beta_1$ ,  $\beta_2$  of the 36 observed Wind distributions together with the variances represented by the error bars. The coordinates of the blue, red and magenta diamonds represent the medians of the  $\beta_1$ ,  $\beta_2$  parameters for all the 36 simulated outputs which correspond respectively to lognormal, Pearson I and power law distributions of the input  $E_i$ . The main conclusion that can be made from Fig. 2.15 is that the two cases of the best agreement between the simulated and the observed Wind outputs is when the input Langmuir waves power distribution is Pearson with  $\lambda = 0.1$  or 1.

## 2.5 Conclusions

We have built an extensive list of type III events detected *in situ*, for which all the three the Langmuir waves, the associated energetic electrons and the type III radio bursts are present. This is the first time such an exhaustive data set is built since the similar studies have been done on much more restricted data sets. The main characteristics of our events are given in Table 2.1 and can be used for further statistical studies.

For each of the 36 events of our list we have built accurate Langmuir waves power distributions by removing correctly the background. Most of these distributions appeared not to be accurately fitted by log-normal distributions. A Pearson type I distribution seemed instead to be the best choice to fit the distribution of the logarithm of the electric field power provided at TNR output. It is to note that the Pearson type I distributions obtained are characterized by an asymmetry in the direction of large electric field powers, a result in qualitative agreement with the one obtained by Bale *et al.* (1997) in the terrestrial electron foreshock.

In order to explore the meaning and the possibility of a physical exploitation of these

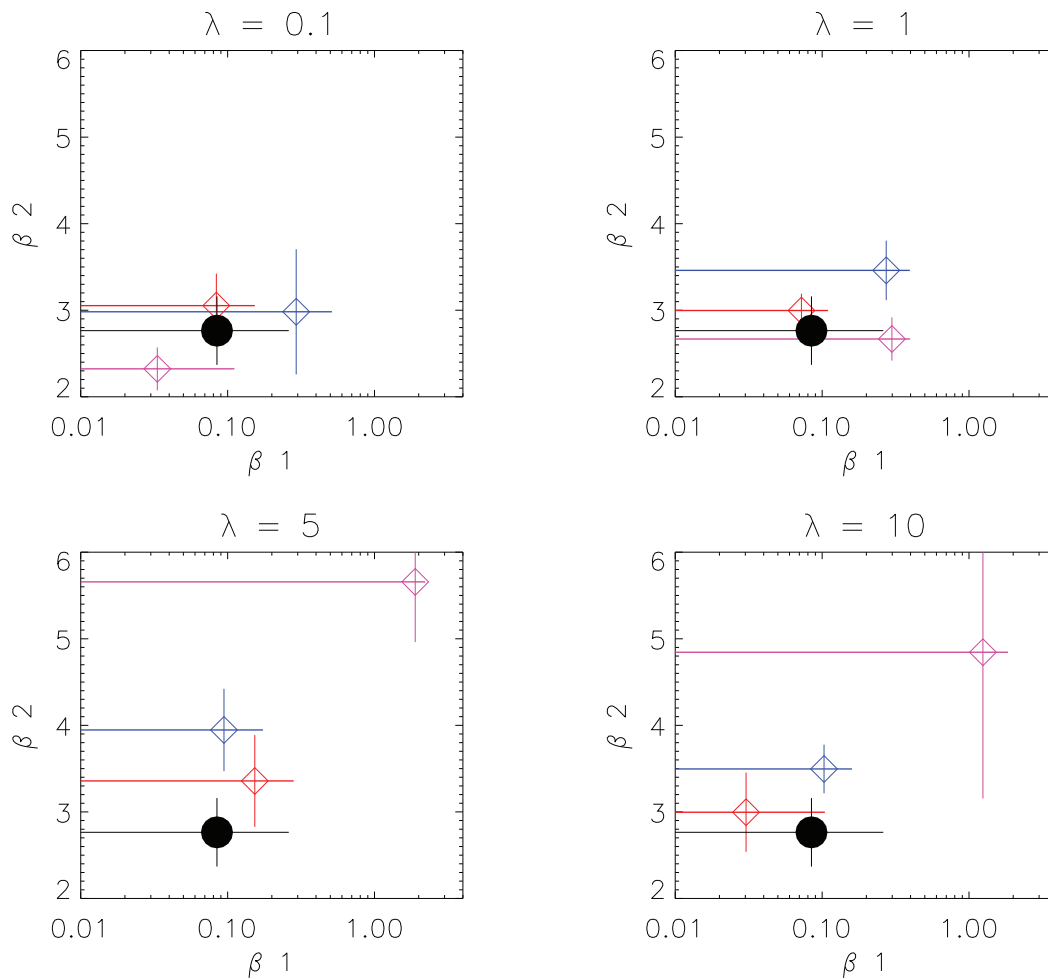


**Figure 2.15:** The values of  $\beta_1$  and  $\beta_2$  parameters from the the Wind observations compared to the corresponding values from our simulations. The coordinates of the black dot (in all four panels) represent the median values of  $\beta_1$ ,  $\beta_2$  of the 36 observed Wind distributions together with the variances represented by the error bars. The coordinates of the blue, red and magenta diamonds represent the medians of the  $\beta_1$ ,  $\beta_2$  parameters for the sets of 36 simulated outputs which correspond respectively to the lognormal, Pearson I and power law distributions of the input  $E_i$ , respectively.

electric field probability distributions, we became interested, in Section 2.4, in the effect of the TNR instrumental transfer function and integration time on a Langmuir wave field which is known to be composed of short duration wave packets. We have thus performed numerical simulations reproducing the response of TNR to various types of input Langmuir waves power distributions and for different values of the rate  $\lambda$  of wave packets per second. By comparing the amplitudes of variations of the simulated output distributions and their shapes (through the values of the  $\beta_1, \beta_2$ ) with the one derived from the Wind observations we can conclude that the best agreement between simulations and observations is achieved when:

- (1) the shape of the input distributions is rather Pearson I or lognormal than a power law which should be definitively excluded;
- (2) the parameter  $\lambda$  lies between 0.1 and 1;
- (3) the maximum value of the input wave packet amplitude is about  $5 \times 10^{-3} \text{ V m}^{-1}$ .

Concerning the last point one can note that this value is lower than the maximum value which can be observed from the Stereo TDS data (Fig. 2.6). This disagreement, which could be due to some intercalibration issues between the Wind TNR and the TDS and to the fact that the TDS amplitudes should be analyzed in a more detailed way, deserves further investigation.

Note that a better agreement is globally obtained with a Pearson I.

A consequence of the wave packet nature of the Langmuir wave field and of our simulations is the fact that the power in output of the TNR is actually smaller than the “instantaneous” power in the wave packets. By examining the maxima of the input Langmuir waves power in the case of lognormal or Pearson distributions with the maxima of the Wind TNR output distributions it appears that there is an overall normalization factor of about 100 (maybe more if the Wind & STEREO TDS discrepancy is solved in the future) that should be applied to the Wind data in order to retrieve the actual Langmuir waves power.



# Other Relationships Between Particles, LW and Type III

## Contents

<b>3.1 Langmuir Waves vs Particles</b> . . . . .	<b>53</b>
3.1.1 Observations . . . . .	54
3.1.2 Relationships between particles and LW power . . . . .	58
<b>3.2 LW vs Type III Power at <math>2f_p</math></b> . . . . .	<b>62</b>

## 3.1 Langmuir Waves vs Particles

The Langmuir electrostatic waves and electromagnetic radio waves, generated locally by the propagation of an electron beam in a surrounding plasma, are some of the basic and fundamental problems in plasma physics. The understanding of the conversion mechanisms by which an electron beam produces Langmuir waves and radio waves is of essential importance to explain some of the strong emissions in plasma astrophysics. Unfortunately, for the distant objects in situ measurements are available only for radio emission and, sometimes, indirect measurements for the source - electron beam. The unique opportunity to study the entire conversion processes, with simultaneously observed energetic electrons and associated Langmuir and radio waves in the regions where these radio waves are generated (*in situ*), is provided by the solar radio bursts thanks to the numerous solar space missions during the last few decades.

Energetic electron beams, ejected and accelerated from the Sun by some violent processes - usually flares or coronal mass ejections, interact with interplanetary plasma to produce Langmuir waves and radio emissions - type III radio bursts (e.g. [Lin, 1985](#); [McLean and Labrum, 1985](#)), see Chapter 1.3 for more details. The main characteristics of solar type III radio bursts is a fast negative frequency drift within very wide range of frequencies, from a few kHz to hundreds of MHz. As the electron beam travels away from the Sun along magnetic field lines, the density of the surrounding plasma decreases, so consequently the frequency of type III bursts decreases in time,  $f_p = 9\sqrt{n_e}$  ( $n_e$  is the electron number density in  $\text{cm}^3$ ,  $f_p$  in kHz). Langmuir waves and energetic electron events measured *in situ* are directly associated with type III solar radio bursts and well-documented by many authors (e.g. [Lin, 1970, 1974](#); [Frank and Gurnett, 1972](#); [Lin et al., 1973](#); [Gurnett and Anderson, 1976, 1977](#)).

The first theoretical explanation of the processes responsible for the type III radio bursts generation was proposed by [Ginzburg and Zhelezniakov in 1958b](#) as a two steps mechanism, now known as a “standard type III model” (see Chapter 1.2 for more details and Appendix A for mathematical review of derivation of the equations). Shortly, the mechanism consists of the following. Firstly, excitation of intense Langmuir waves at the local electron plasma

frequency by electron beam through a “bump-on-tail” velocity distribution instability. The “bump-on-tail” instability mechanism is actually the Landau growth mechanism (inverse of Landau damping, Landau 1946) caused by velocity dispersion where higher energy electron fluxes rise ahead of lower energy electron fluxes creating a positive slope in velocity distribution,  $\partial f(v_{\parallel})/\partial v_{\parallel} > 0$ . Secondly, subsequent conversion of these Langmuir waves into radio emissions at plasma frequency,  $f_p$ , and its first harmonic,  $2f_p$ , through nonlinear wave-wave interactions.

A strong support to the standard type III model is provided by the observations of type III solar radio bursts and energetic particles (Lin *et al.*, 1981; Ergun *et al.*, 1998; Gosling *et al.*, 2003; Krucker *et al.*, 2007), by the theoretical development (Zheleznyakov and Zaitsev, 1970a,b; Zaitsev *et al.*, 1972; Takakura and Shibahashi, 1976; Melnik, 1995) and numerical simulations (Magelssen and Smith, 1977; Kontar *et al.*, 1998; Yoon *et al.*, 2000; Kontar, 2001; Li *et al.*, 2006; Krasnoselskikh *et al.*, 2007; Reid and Kontar, 2010, 2012).

Despite the great interest and work already done, the electron beam propagation and plasma radio emission are far from being well understood. This is mostly because these processes are essentially a nonlinear multiscale problems, hardly or non-solvable.

The intention of this study is: (1) to examine how the characteristics of electron beam are related to the locally generated Langmuir waves that are associated with the observations of type III solar radio bursts; (2) to find relations between Langmuir waves power and electron beam fluxes, energies and densities. For this purpose we use the data set described in Section 2.1 (16 years of Wind observations, from the end of 1994 to the beginning of 2010, during periods when the spacecraft was far from the Earth’s bow shock). By using additional strict selection criteria and a careful analysis, we extracted a high-quality database consisting of 19 events. This dataset is numerous enough to perform studies of the variations of the observed Langmuir waves properties with the variations on the energetic electron beams that generate them.

### 3.1.1 Observations

The main experiment of interest is the 3-D Plasma and Energetic Particle (3DP) Investigation (Lin *et al.*, 1995) that provides the full three-dimensional distribution of suprathermal electrons. For the impulsive electron events the data detected with the electrostatic analyzers (EESAs) from  $\sim 0.2$  keV to  $\sim 27$  keV in 15 energy channels are used. The electron energy flux spectra are produced by summation over angular bins – omnidirectional flux. The energetic electron events are easily recognizable by their velocity dispersion, with faster electrons arriving earlier, as expected if the electrons of all energies are simultaneously accelerated at the same point and travel the same distance along the interplanetary field to reach the spacecraft.

In addition to the TNR (see Section 2.1 for more details about TNR instrument) and EESAs data, for the selection of sample events, measurements from a few instruments were used: (1) WAVES experiment – in the radio domain, where the electromagnetic type III bursts are observed, the data from the RAD1, that cover frequency range from 20 to 1040 kHz, and RAD2, from 1075 to 13825 kHz, radio receivers were used; (2) one minute averaged measurements of the interplanetary magnetic field vector in GSE (Geocentric Solar Ecliptic) cartesian coordinates from the Magnetic Field Investigation (MFI) experiment, Lepping *et al.* (1995); (3) solar wind data from the Solar Wind Experiment (SWE), Ogilvie *et al.* (1995), which provides three-dimensional velocity, density and temperature of the solar wind protons and electrons.

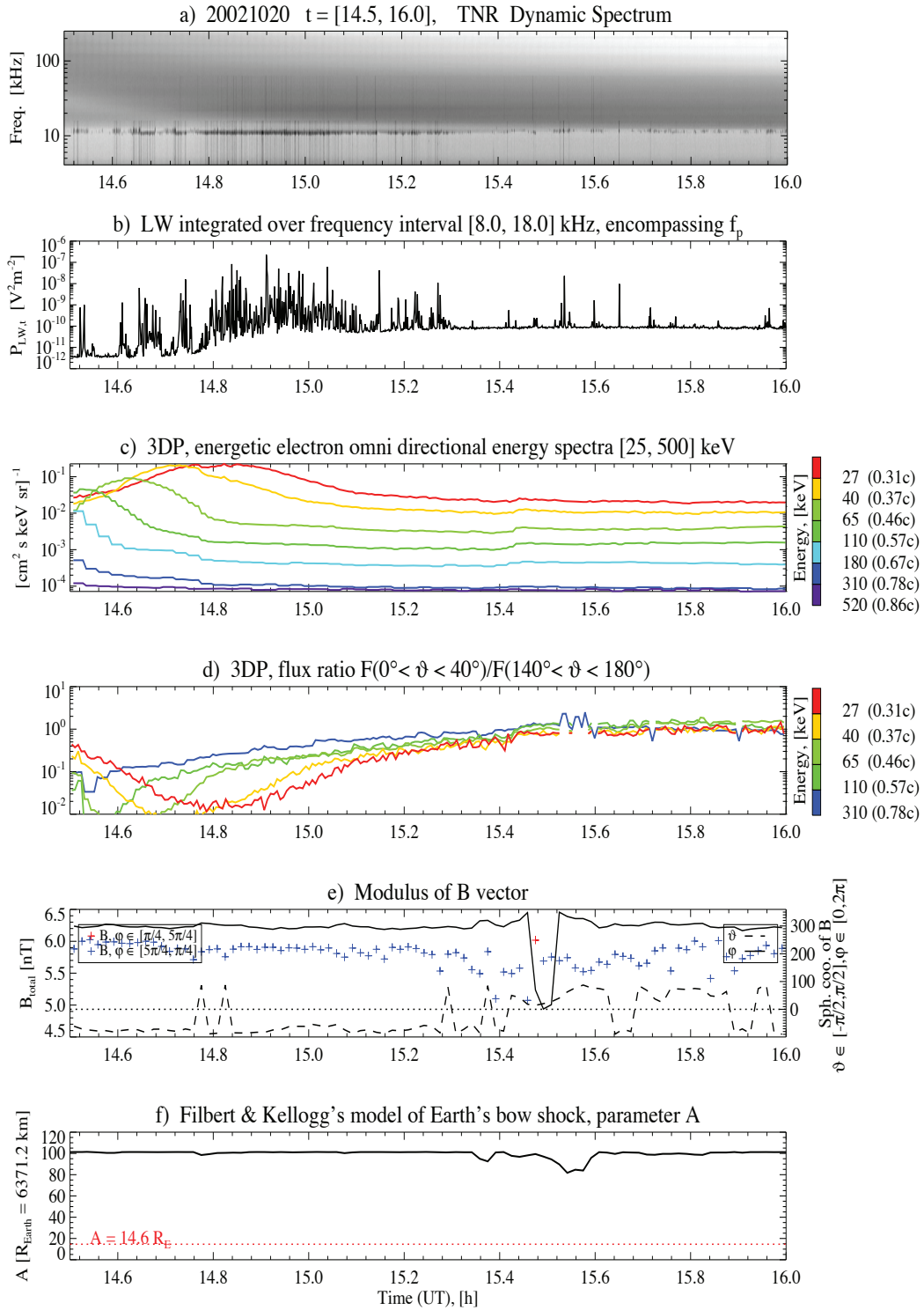


**Figure 3.1:** Wind observations on 20 October 2002 within a time interval from 14.5 to 16.0 h encompassing the data when Langmuir waves occur. (See explanation of the figure on page 56.)

**Table 3.1:** List of impulsive (energetic) events. (See explanation of the Table on page 56.)

No.	Date	$t_1$	$t_2$	$f_p$	$f_1$	$f_2$	$V_{SW}$ [km s <sup>-1</sup> ]	$T_e$ [eV]	$n_e$ [cm <sup>-3</sup> ]	Ch.	$\bar{E}_{ch}$ [keV]
		[h]	[h]	[kHz]							
2	19950402	11.75	12.75	24.0	20	30	360	7.62	8.12	1-5(5)	14.9
3	19950402	15.05	15.50	24.0	20	30	355	7.51	7.68	2-3(2)	15.9
5	19971123	10.65	11.60	22.5	18	26	502	7.49	9.00	1-5(5)	14.9
6	19971123	14.50	15.50	15.0	10	20	475	4.89	9.70	1-3(3)	19.8
7	19980712	00.30	01.90	14.5	11	19	384	4.69	12.44	1-8(8)	10.4
8	19980712	01.95	02.83	13.5	10	19	384	4.46	12.52	1-5(5)	14.9
13	19980906	07.05	08.20	28.0	16	30	350	8.60	12.08	1-6(6)	13.1
21	20000404	15.80	16.40	27.0	21	31	380	3.96	25.43	2-7(6)	8.9
22	20000504	11.49	11.67	20.0	16	25	465	3.11	23.82	2-8(7)	7.9
24	20000617	03.70	04.55	18.0	16	21	480	3.44	25.85	3-8(6)	6.1
25	20020322	11.65	13.35	22.0	16	30	440	3.60	23.62	2-6(5)	10.2
27	20021020	14.50	16.00	13.5	08	18	650	3.16	20.26	4-5(2)	7.4
28	20021021	04.50	06.90	12.0	08	18	583	3.18	20.20	2-4(3)	13.5
29	20021212	13.35	15.20	21.5	17	28	362	4.10	19.70	1-5(5)	14.9
31	20030331	04.75	06.15	18.0	10	24	630	3.42	20.89	1-4(4)	17.1
32	20030401	00.75	02.65	24.0	10	20	520	3.33	19.87	2-6(5)	10.2
33	20040605	07.20	08.55	23.5	20	30	449	3.81	17.25	1-4(4)	17.1
35	20040829	03.55	04.14	17.5	16	24	416	3.16	16.73	1-3(3)	19.8
36	20050316	20.65	21.43	22.0	16	29	376	4.55	15.84	1-6(6)	13.1

All these measurements, taken *in situ* simultaneously by the four Wind experiments, allow to perform a high-quality selection and analysis of the events of interest.

**Fig. 3.1** describes the basic data we use: a) dynamical spectra, only TNR receiver observations (4–256 kHz); b) power spectral density integrated over a narrow frequency band (8–18 kHz) around the plasma frequency ( $\sim 13.5$  kHz); c) omnidirectional spectrum of energetic electron fluxes, 3DP experiment; the energies are indicated on the right-hand side of the panel; d) energetic electron flux ratio  $F(0^\circ < \vartheta < 40^\circ)/F(140^\circ < \vartheta < 180^\circ)$  where  $\vartheta$  is pitch angle; e) magnetic field intensity; color of "+" symbols indicates the direction of the magnetic field vector from the Sun (red) or from the Earth (blue); solid and dashed lines indicate two spherical coordinates ( $\vartheta, \varphi$ ), respectively; f) parameter  $A$  of Filbert and Kellogg's model of the Earth's bow shock; the red dotted line indicates distance along x-axis from the Earth to the nose-cone (vertex of the paraboloid) of the Earth's bow shock in steady state; if  $A$  is greater than 14.6 Earth's radii, it means that Wind spacecraft is outside of the Earth's bow shock.

### Selection of sample events

From the sample of 36 events selected in Ch. 2, those events where impulsive electron events can be seen at the same time as Langmuir waves were extracted. Several additional criteria had to be satisfied: (1) a clear velocity dispersion; (2) high enough signal-to-noise ratio; (3) a clear separation from surrounding events to avoid multiple events. The analysis of the data detected with the electrostatic analyzers (EESAs) showed that these conditions are satisfied for 19 out of 36 previously selected events. An overview of the 19 events selected for the present investigation is shown in Table 3.1. The ordinal numbers of the events are preserved as they are in Table 2.1.

**Table. 3.1** contains: calendar date is represented in form YYYYMMDD (year, month, day), approximate starting time (UT),  $t_1$ , and approximate ending time (UT),  $t_2$ , of Lang-

**Table 3.2:** Electron energies of 15 logarithmically spaced channels (steps) of electrostatic analyzers (EESAs). The electron speed is calculated with relativistic correction, it is presented in speed of light units,  $c$ .

Ch. no	Energy [eV]	Speed in $c$
1	27662.75	0.316
2	18944.42	0.265
3	12965.75	0.221
4	8874.877	0.184
5	6076.481	0.153
6	4161.270	0.127
7	2849.213	0.105
8	1952.315	0.087
9	1339.371	0.072
10	920.2957	0.060
11	634.3848	0.050
12	432.7296	0.041
13	292.0642	0.034
14	200.0561	0.028
15	136.8446	0.023

muir waves in form hh (hour). In the next 3 columns are: approximate plasma frequency ( $f_p$ ) and frequency interval ( $f_1$  and  $f_2$ ) used for the integration in Eq. 2.1. The next column presents the modulus of the solar wind velocity vector ( $V_{SW}$ ) in GSE coordinates from the SWE instrument obtained as an average over time of the event duration.  $T_e$  and  $n_e$  are electron temperature and electron number density from 3DP key parameters averaged over the event duration. Ch. – the channels of electrostatic analyzers (EESAs) where energetic electron event can be seen – where signal-to-noise ratio is high enough. The 15 EESAs channels are numerated from highest energies (27 keV) to lowest (0.13 keV), see Table 3.2. The total number of channels where energetic electron event can be seen is given in parentheses.  $\overline{E}_{ch}$  is energy of channels averaged over the channels where energetic electron event can be seen (previous column).

### Background removal from the energetic particles data

To remove the background from the omnidirectional electron flux data obtained in a particular channel of the EESAs instruments, the following procedure was performed: (1) the electron flux data were smoothed out by moving average method; (2) a quiet period around the impulsive electron event was identified, usually 1 hour or less, but not less than half an hour before the impulsive electron event; (3) the electron flux was averaged over the quiet time period - this was considered to be the background level; and (4) the background was subtracted from electron flux, that only electrons belonging to the beam remained.

In order to perform the planned analysis, three dimensional points are created ( $E_{ch}, n_{ch}, P_{LW}$ ).  $E_{ch}$  is the energy of a particular channel of EESA instrument in [keV] (see Table 2 for electron energies of particular channel),  $n_{ch}$  is electron flux in  $[\text{cm}^2\text{s sr eV}]^{-1}$  integrated over time interval of 12 minutes centered on electron flux maximum and  $P_{LW}$  is power of Langmuir waves in  $[\text{V}^2\text{m}^{-2}]$  integrated over the same time interval as the electron

flux. The numerical integration is performed using the trapezium method in both cases. The time interval of 12 minutes was chosen empirically to avoid overlapping in Langmuir waves power series and, on the other hand, to get a rough approximation, fair enough for a preliminary analysis, of electron flux measured by a particular channel belonging to the electron beam. It turns out that energetic electron fluxes can be seen only in the first 8 most energetic EESAs channels that spawn electron energies from  $\sim 2$  to  $\sim 27$  keV. This fact indicates that the energies of electrons responsible for Langmuir waves emission are within range [2,27] keV. It should be noted that [Lin \*et al.\* \(1996\)](#) have reported Wind observations of an impulsive solar electron event (associated with type III radio burst, solar flare and weak soft X-ray burst) spanning the entire energy range from solar wind plasma to several hundreds keV – the energy spectrum of the electrons escaping to 1 AU extends down to 0.5 keV. The energies of channels averaged over the channels where energetic electron events can be seen ( $\overline{E}_{\text{ch}}$ ) are presented in [Table 3.1](#), last column.

Finally, for 19 events where energetic electron events and Langmuir waves are associated with type III solar radio bursts, 90 three-dimensional points ( $E_{\text{ch}}, n_{\text{ch}}, P_{\text{LW}}$ ) in 8 different EESA instrument channels were obtained.

### 3.1.2 Relationships between particles and LW power

In this section we examine the relationships between the Langmuir waves power and the energetic particle energies and fluxes.

A strong linear dependence between two of the variables: logarithms of  $E_{\text{ch}}$  and  $n_{\text{ch}}$  (see [Fig. 3.2](#)) was found, so it is investigated in more details. The averages of electron fluxes over energy channels are indicated by red circles (they correspond to  $\overline{n}_{\text{ch}}$ ). The error bars are calculated as  $1\sigma$  standard deviations. The red line is the best linear fit obtained by the least-square method:

$$\overline{n}_{\text{ch}} = bE_{\text{ch}}^{\gamma}. \quad (3.1)$$

The value of the power-law index,  $\gamma$ , was found to be  $-2.47 \pm 0.06$ . This result is in good agreement with the results obtained by [Krucker \*et al.\* \(2009\)](#) for a statistical survey of the spectral shapes of 62 solar impulsive electron events detected within 1 to 300 keV, not necessarily accompanied by type III radio bursts, and [Lin \*et al.\* \(1982\)](#) for nine events seen within 10 keV to 10 MeV almost all accompanied by type III radio bursts. This power law is actually the remnant of the shape of the energy distributions of the electrons that are accelerated at the Sun.

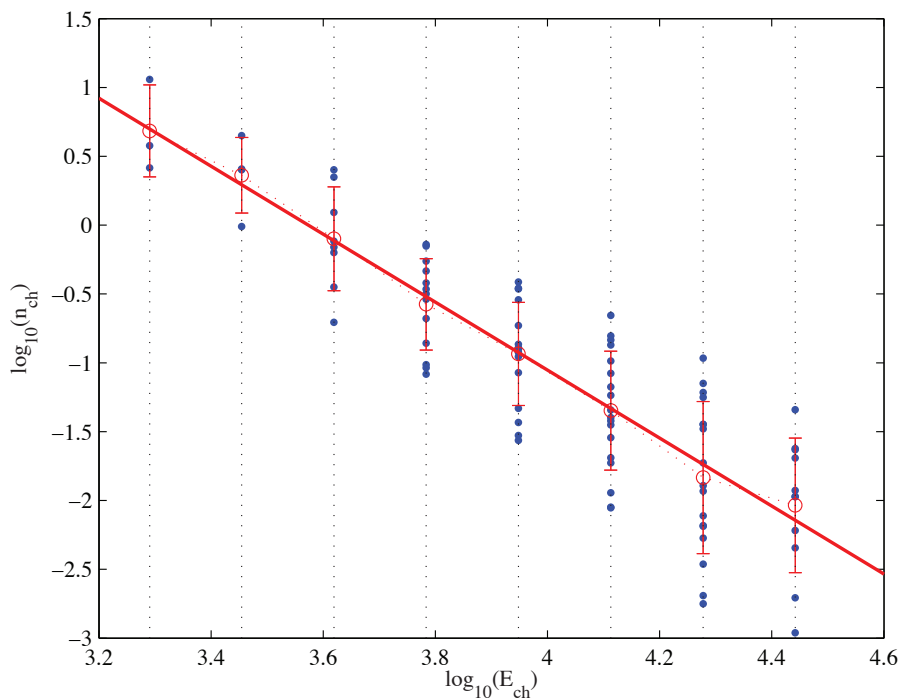
If we examine now the variations of the Langmuir waves power  $P_{\text{LW}}$  as a function of the energy  $E_{\text{ch}}$  of the beam particles only, we will obtain the results presented in [Figure 3.3](#).  $P_{\text{LW}}$  seems to be a clearly increasing function of  $E_{\text{ch}}$  in the range  $\sim 2$  to 7 keV. Above this latter energy value,  $P_{\text{LW}}$  is presenting a “plateau” to be constant with electron-energy increase. Concerning the results displayed in [Figure 3.3](#) we have initiated a strong collaboration with the authors of the following articles [Reid and Kontar \(2010, 2012\)](#). These articles provide full comprehensive simulations of electron beam propagation from the Sun to the Earth in the weak turbulent regime taking into account the self-consistent generation of Langmuir plasma waves and subsequent wave interaction with density fluctuations from low-frequency MHD turbulence. Two main conclusions already appear. Firstly, the strong power-law dependence that we observe between electron flux and electron energies with power-law index  $\gamma = -2.47 \pm 0.06$  agrees quite well with the [Reid and Kontar \(2010, 2012\)](#) simulations. In particular, starting with a  $(E_0/E)^{3.5}$  for the energy spectrum at the solar flare, [Reid and Kontar \(2010, 2012\)](#) show that at low energy (in the range of our observations) the particles interact with the Langmuir waves and the slope of the particles spectra decreases to smaller values that we observe in this study. Secondly, the Langmuir waves

“plateau” that we observe in the experimental data (Fig. 3.3) is quite well represented by the simulations by Reid and Kontar (2010, 2012) as it can be seen in Fig. 3.4. The detailed comparison of our observational findings with the Reid and Kontar (2010, 2012) simulations will be the subject of a future work.

Another way of representing these results is to plot  $P_{LW}$ , normalized to the electron plasma pressure ( $n_e k_B T_e$ ), where  $n_e$  and  $T_e$  are the ambient electron density and temperature, as a function of the electron beam speed  $v_b$  (with relativistic correction included), normalized to the ambient electron thermal speed  $v_{th}$ . The speeds are calculated using equations 3.2.

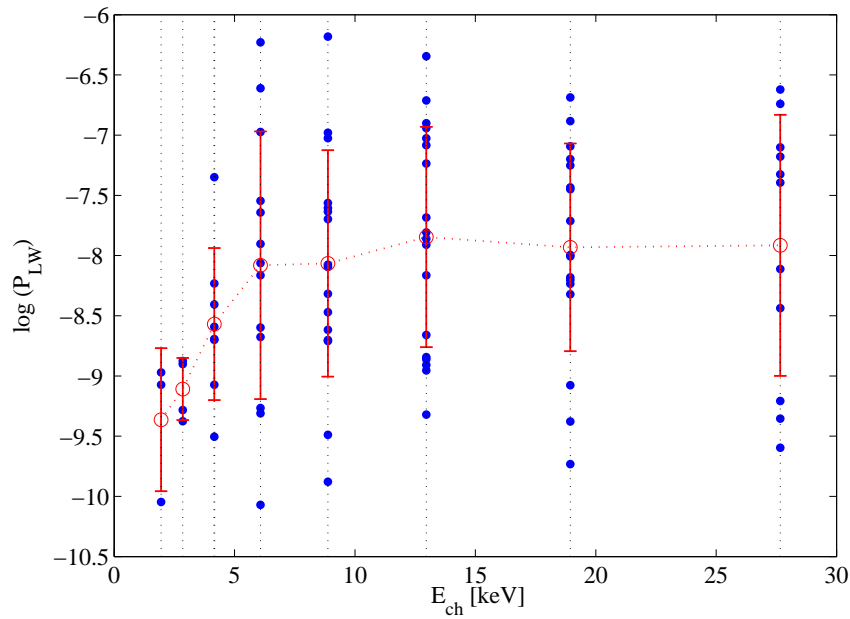
$$v_b = c \sqrt{1 - \frac{1}{\left(\frac{E_b}{E_0} + 1\right)^2}}, \quad v_{th} = \sqrt{\frac{2k_B T_e}{m_e}} \quad (3.2)$$

Figure 3.5 represents these normalizations. Similar trend as in Fig. 3.3 is notable – as the ratio  $v_b/v_{th}$  increases, normalized  $P_{LW}$  also increases.



**Figure 3.2:** The electron flux in  $[\text{cm}^2 \text{s sr eV}]^{-1}$  integrated over time interval of 12 minutes centered on electron flux maximum versus energy of the EESA instrument channels (in [keV]) where energetic electron events can be seen – both in logarithmic scale (blue dots). The averages of electron fluxes over energy channels are indicated by red circles (they correspond to  $\bar{n}_{ch}$ ). The error bars are calculated as  $1\sigma$  standard deviations.

The latter aspect of the relations between Langmuir waves power and energetic electrons examined in the thesis, was the relation between normalized Langmuir waves power and electron beam number density ( $n_b$ ). The transformation from the spectral fluxes measured by 3DP instrument in units  $[\text{cm}^2 \text{s sr eV}]^{-1}$  to number density in  $\text{cm}^{-3}$  was done using the following procedure (Krucker (2012), private communication). To eliminate steradians (sr) it was assumed that the electrons arrive from the Sun, thus integration over half the sphere is probably a reasonable approximation. Since the flux is measured at particular



**Figure 3.3:** Logarithm of Langmuir waves power integrated over time interval of 12 minutes centered at the time of electron flux maximum versus energy of the EESA instrument channels (in [keV]) where energetic electron events can be seen – blue dots. The averages of Langmuir waves power are indicated by red circles (they correspond to logarithm of  $\overline{P}_{LW}$ ). The error bars are calculated as  $1\sigma$  standard deviations.

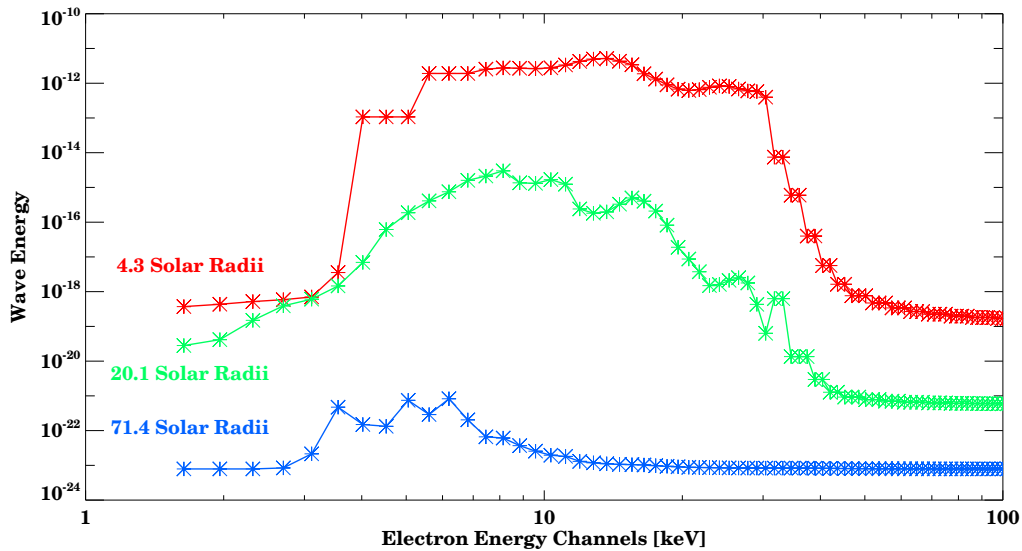


**Figure 3.4:** Results of quasilinear simulations of an electron beam propagating through the interplanetary medium. Langmuir wave energy [ $\text{erg s cm}^{-4}$ ] is plotted on the y-axis as a function of phase velocity. The x-axis represents the kinetic energy of an electron with the same velocity as the phase velocity of the Langmuir waves. Figure provided by courtesy of Hamish Reid.

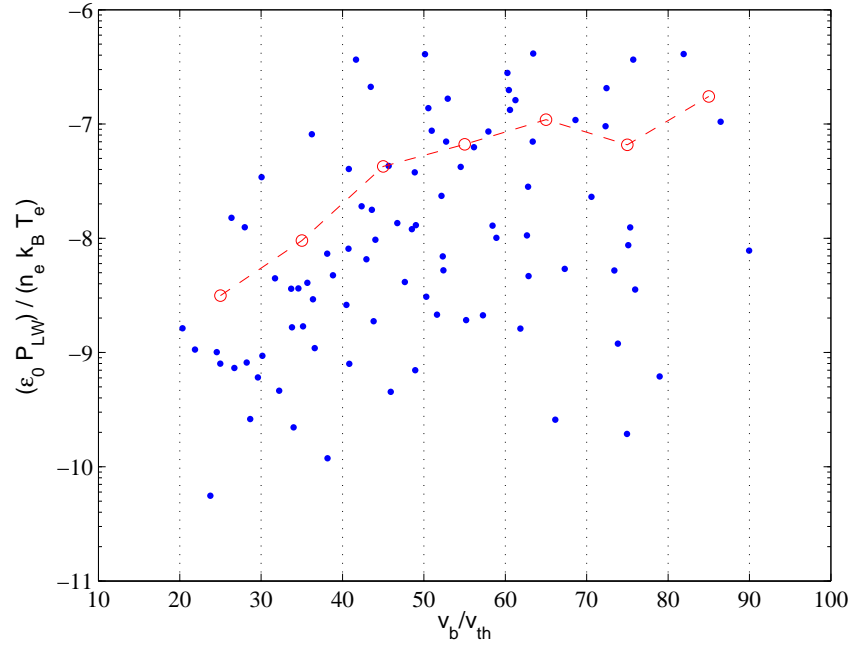


**Figure 3.5:** Langmuir waves power  $P_{LW}$ , normalized to the electron plasma pressure ( $n_e k_B T_e$ ) as a function of the electron beam speed  $v_b$ , normalized to the ambient electron thermal speed  $v_{th}$  (blue points). Red circles represent the averages of normalized Langmuir waves power over the bins of  $10 v_b/v_{th}$  indicated by dotted vertical lines.

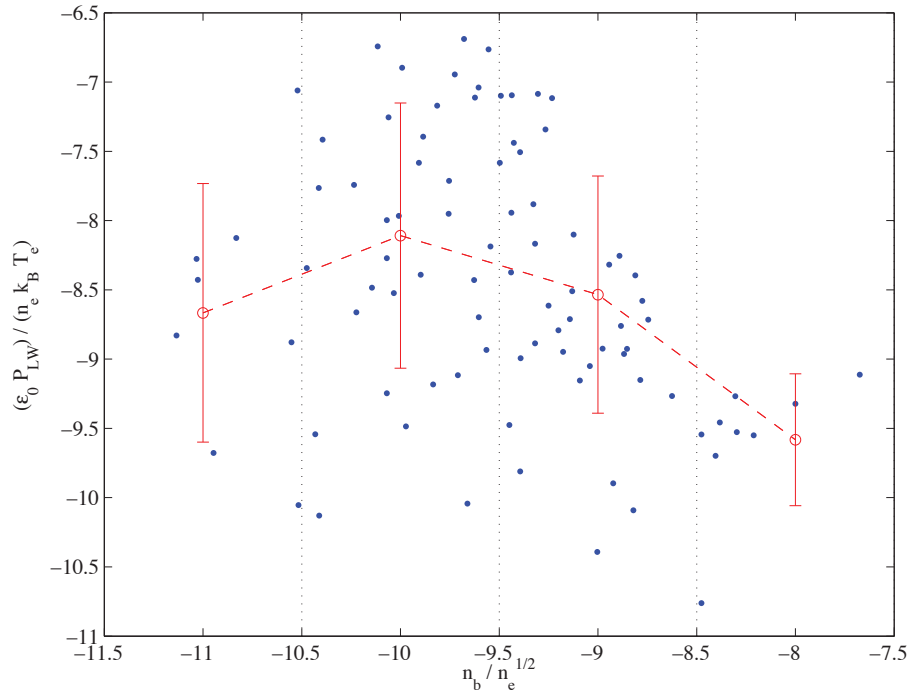


**Figure 3.6:** Scaled power of Langmuir waves,  $P_{LW}$ , as a function of the rate at which the Langmuir waves are generated (inverse of the quasilinear relaxation time),  $n_b/\sqrt{n_e}$ . The quantities are presented in logarithmic scale.

energies, electron-volts (eV) are eliminated multiplying the flux by energy of particular channel. Similarly, seconds (s) are eliminated dividing the flux by speed of the electrons corresponding to the energy channel.

The Langmuir waves excited by the electron beam flatten the electron velocity distribution function. Thus, for the characteristic time of electron–wave interaction (quasilinear relaxation time)

$$\tau_{QL} \approx \frac{1}{\omega_p} \left( \frac{n_b}{n_e} \right)^{-1} \quad (3.3)$$

where  $n_b$ ,  $n_e$  are the beam and plasma density, and  $\omega_p$  is the electron plasma frequency, a plateau is formed at the electron distribution function (see for example Mel'nik and Kontar, 2000 or Kontar, 2001 and reference therein). Thus, substituting  $\omega_p \sim \sqrt{n_e}$  in the previous equation, the rate at which the Langmuir waves are generated (inverse of the quasilinear relaxation time) can be expressed as:

$$P_{LW} \sim \frac{1}{\tau_{QL}} \sim \frac{n_b}{\sqrt{n_e}}. \quad (3.4)$$

Fig. 3.6 displays  $P_{LW}$  as a function of  $n_b/\sqrt{n_e}$ . As it can be seen, the two quantities are not proportional to each other. We observe that  $P_{LW}$  is proportional to  $n_b/\sqrt{n_e}$  up to a value of this ratio of  $10^{-10}$  where it reaches a maximum and then decreases. As the rate of Langmuir waves generation increases, we expect the Langmuir waves power to do the same, but we do not observe such a trend in the figure. We can try to improve the procedure by taking total density of the beam over all energy channels for the certain moment of time, but hardly that it will do better because Eq. 3.4 is just a very rough approximation – the processes are much more complicated. Ideally, we need the instrument with subsecond time resolution to be able to measure positive gradient in velocity space of the electrons, so then we could calculate the real growth rate of the Langmuir waves. On the other hand, an instrumental effect of  $\Delta E/E$  may be the cause for an inadequate/biased measurement of  $n_b$ , or electron beam propagation effect (Bale, 2011, private communication).

### 3.2 LW vs Type III Power at $2f_p$

The existence of electromagnetic waves emission at multiple of the local electron plasma frequency ( $nf_p$ , where  $f_p$  represents electron plasma frequency and  $n$  is a positive integer number) is confirmed by numerous observational measurements. Particularly, the substantial theoretical and observational work has been done on electromagnetic plasma emission at twice the electron plasma frequency and how it scales with Langmuir waves energy. The examples of electromagnetic  $2f_p$  emission are found at Earth's bow shock, the solar type II and III radio bursts from interplanetary shocks and the solar corona (e.g. Gurnett and Frank, 1975; Kasaba *et al.*, 2000; Henri *et al.*, 2009, etc). The most probable mechanism of the electromagnetic  $2f_p$  emission is thought to consist of two sequential three-wave steps during an electron-beam-plasma interaction (e.g. Cairns and Melrose, 1985). First, backscattered Langmuir waves are excited by parametric decay of large amplitude Langmuir waves, i.e.,  $L \rightarrow L' + I$ , where  $L$ ,  $L'$  and  $I$  represent forward Langmuir waves, backscattered Langmuir waves, and ion acoustic waves, respectively. Second, electromagnetic  $2f_p$  waves are excited by a wave-wave coupling of forward and backward Langmuir waves,  $L + L' \rightarrow T$ , where  $T$  represents transverse electromagnetic waves. Because of the three-wave coupling condition ( $\omega_L + \omega_{L'} = \omega_T$  and  $\kappa_L + \kappa_{L'} = \kappa_T$ ), the transverse electromagnetic wave  $T$  has a frequency almost equal to twice the plasma frequency.

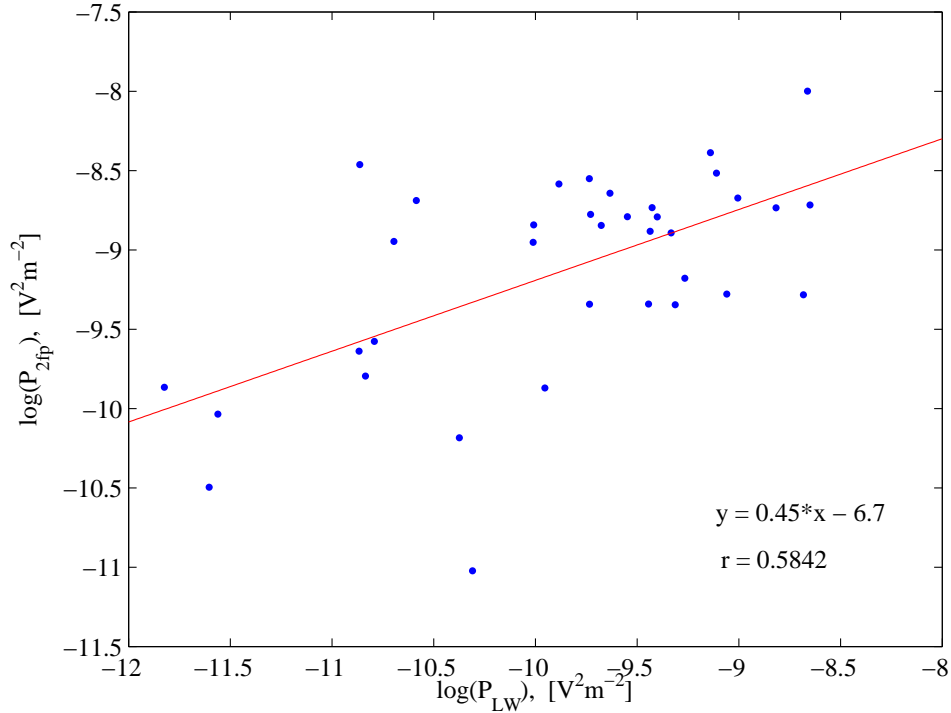


**Figure 3.7:** Type III power at  $2f_p$  vs LW power. Red line is linear fit of logarithms of means ( $P_{LW}$  and  $P_{2f_p}$ ). Correlation coefficient of these two variables is  $r = 0.5842$ .

To investigate the relation between Langmuir waves and type III radio bursts, we used our data set of 36 events described in Ch. 2. According to the “standard type III model”, the Langmuir waves are subsequently converted into radio emissions at the fundamental ( $f_p$ ) and first harmonic ( $2f_p$ ) of plasma frequency through nonlinear wave–wave interactions. Since the intensity of Langmuir waves (at plasma frequency,  $f_p$ ) is much higher than the intensity of the type III radio bursts (only the small part of Langmuir waves energy is converted into the type III bursts), the natural choice was to investigate radiation in type III bursts at the first harmonic of plasma frequency. To get a more reliable picture, the average of the radiation at a frequency nearest to the first harmonic and the next higher one was taken and summed from  $t_1$  to  $t_2$  (see Table 2.1 for time intervals). The obtained values are shown in Fig. 3.7 in logarithmic scale. The best fit by the least-square method gave a slope of 0.45; it is represented by the red line. The correlation coefficient is found to be about 0.6. We consider it fair enough, since the background of type III radiation was not removed. The main conclusion from this figure is that the correlation of the radio power and the Langmuir waves power is actually quite good. Further analyses are necessary to study this dependence in more details.



# General Conclusions

## Contents

4.1 Conclusions . . . . .	65
---------------------------	----

## 4.1 Conclusions

Up to now, only a few studied cases of *in situ* type III bursts have been reported in the literature (Lin *et al.*, 1973; Ergun *et al.*, 1998). The intent of this research was to examine statistically in details the basic and general characteristics of Langmuir waves associated with type III solar radio bursts and electron beams responsible for their generation, all observed *in situ* simultaneously. Thus, we have built an extensive set of type III events detected *in situ* by the Wind spacecraft over 16 years of observations. For each event all the three the Langmuir waves, the associated energetic electrons and the type III radio bursts are present. This is the first time that such an exhaustive data set is built which can be used for further statistical studies.

For each of the 36 events of our set we have constructed accurate Langmuir waves power distributions previously removing correctly the background. A Pearson type I distribution seemed to be the best choice to fit the distribution of the logarithm of the electric field power provided at TNR's output. It is to note that the obtained Pearson distributions are characterized by an asymmetry in the direction of large electric field powers, a result in qualitative agreement with the one obtained by Bale *et al.* (1997) in the terrestrial electron foreshock. In order to explore the meaning and the possibility of a physical exploitation of these electric field probability distributions, we examined the effect of the TNR instrumental transfer function and integration time on a Langmuir wave field. We have performed numerical simulations reproducing the response of TNR to various types of input Langmuir waves power distributions and for different wave packet rates per second. By comparing the amplitudes of variations of the simulated output distributions with those derived from Wind observations, we can conclude that the best agreement between simulations and observations is achieved when:

1. the shape of the input distributions is rather Pearson I or lognormal than a power law which should be definitively excluded;
2. the wave packets rate ( $\lambda$ ) lies between 0.1 and 1;
3. the maximum value of the input wave packet amplitudes is about  $5 \times 10^{-3} \text{ V m}^{-1}$ .

A consequence of the nature of the Langmuir wave packet field and of our simulations is the fact that the power in output of the TNR is actually smaller than the "instantaneous" power in the wave packets. By examining the maxima of the input Langmuir waves power in the case of lognormal or Pearson distributions with the maxima of the Wind TNR output

distributions, it appears that there is an overall normalization factor of about 100 that should be applied to the Wind data in order to retrieve the actual Langmuir waves power.

In the further examination we have found preliminary relations between Langmuir waves power, electron beam fluxes, energies and densities. By using additional selection criteria, we extracted 19 events from the data set of 36 events used in previous analysis, where an increase of electron fluxes was detected by 3DP instrument.

- (i) We found a strong linear dependence between logarithms of electron energies and their fluxes. The value of power-law index was found to be  $-2.47 \pm 0.06$ . This result is in good agreement with results obtained by [Krucker \*et al.\* \(2009\)](#) for a statistical survey of the spectral shapes of 62 solar impulsive electron events detected within 1 to 300 keV, not necessarily accompanied by type III radio bursts, and [Lin \*et al.\* \(1982\)](#) for nine events seen within 10 keV to 10 MeV almost all accompanied by type III radio bursts.
- (ii) For variations of the Langmuir waves power as a function of the energy of the beam electrons, the Langmuir waves power is clearly an increasing function of electron energy within the range  $\sim 2$  to 7 keV. Above this energy, Langmuir waves power is presenting a “plateau” staying constant with energy increase. This experimental result is in quite good agreement with the simulations by [Reid and Kontar \(2010, 2012\)](#). The detailed comparison of our observational findings with their simulations will be the subject of a future work.
- (iii) The next aspect of the relations between Langmuir waves power and energetic electrons examined in the thesis, was the relation between normalized Langmuir waves power and electron beam number density ( $n_b$ ). The rate at which the Langmuir waves are generated (inverse of the quasilinear relaxation time) is roughly proportional to electron beam number density,  $\tau_{QL}^{-1} \propto n_b/\sqrt{n_e}$ . We have observed the proportionality up to a value of this ratio of  $10^{-10}$  where it reaches a maximum and then decreases. But, the expected dependence has not been found. Several reasons can be the cause that we do not obtain the expected functional dependence. This result may be biased by instrumental effects; it needs further consideration.
- (iv) The relation between electromagnetic radiation in type III radio bursts and electrostatic radiation of Langmuir waves was tested for the type III radiation at the first harmonic of the plasma frequency,  $2f_p$ . It is found a rather not too strong linear dependence (in logarithmic scale) with slope of 0.45 and correlation coefficient 0.6, but we consider it good enough taking into account that the background in type III radiation was not removed. This is the first observational statistical evidence of the proportionality between electromagnetic radiation in type III radio bursts at  $2f_p$  and electrostatic radiation of Langmuir waves ( $P_{2f_p} \propto P_{LW}$ ).

These statistical results obtained directly from the measurements can be used as reliable direction guidances for theoretical work, in understanding limitations of existing instruments and in construction of instruments for future missions, as well as in numerical simulations, comparison with solar flares X-ray,  $\gamma$ -ray, ground based radio, optical measurements etc. Additionally, this work is indirectly related to the acceleration of solar energetic electrons: the electron beams are source of electromagnetic emission, therefore the radio bursts can be used to track the escaping electrons from the Sun into the interplanetary medium. Furthermore, they provide possibility to investigate acceleration of electrons during a non-linear stage of beam-plasma instability to the energies greater than the energies at which they were injected.

The research work on the data set of 36 high-quality events, selected for the thesis, is far from exhausted. There is plenty of room for the continuation of the investigation and improvements. For example, it is necessary to refine the analysis already done in many aspects; to understand instrumental effects on electron beam number density; to find relation between total power of Langmuir waves and total power of type III radio bursts; to improve density model of interplanetary medium, and much more.

At the end, the exciting time is yet to come – the time when we will be able to compare theories and results obtained by using measurements at 1 AU (only available for now) and measurements of future missions which will go *close* to the Sun. Particularly, the RPW<sup>1</sup> instrument on Solar orbiter and Fields<sup>2</sup> instrument on Solar probe + will be of crucial importance from the perspective of the research performed in the thesis.

---

<sup>1</sup>The RPW (Radio and Plasma Waves) experiment is unique amongst the Solar Orbiter instruments in that it makes both in situ and remote sensing measurements. RPW will measure magnetic and electric fields at high time resolution using a number of sensors/antennas, to determine the characteristics of electromagnetic and electrostatic waves in the solar wind.

<sup>2</sup>The Fields instrument on Solar Probe + will make direct measurements of electric and magnetic fields, radio emissions, and shock waves which course through the Sun's atmospheric plasma. Fields also turns Solar Probe + into a giant dust detector, registering voltage signatures when specks of space dust hit the spacecraft's antenna.



# Derivation of Landau Damping

## Contents

<b>A.1 Collisionless Boltzmann Equation . . . . .</b>	<b>69</b>
<b>A.2 Solution of the Vlasov Equation . . . . .</b>	<b>70</b>

## A.1 Collisionless Boltzmann Equation

The motion of a particle of mass  $m$  is defined by its position  $\mathbf{r}$  and its velocity  $\mathbf{v}$ . Each particle can therefore be represented by a point  $(\mathbf{r}, \mathbf{v})$  in space called “phase” space. This space is six-dimensional with coordinates  $(x, y, z, v_x, v_y, v_z)$ . The probability density of points in this  $(\mathbf{r}, \mathbf{v})$  space at time  $t$  is proportional to the distribution function  $f(\mathbf{r}, \mathbf{v}, t)$ .  $f(\mathbf{r}, \mathbf{v}, t)d\mathbf{r}d\mathbf{v}$  represents the expected number of particles at time  $t$  in  $d\mathbf{r}$  space with coordinates  $\mathbf{r}$  and  $\mathbf{r} + d\mathbf{r}$  and velocity  $\mathbf{v}$  and  $\mathbf{v} + d\mathbf{v}$ . Plasma instruments flown in space are now capable of measuring directly the distributions of the particles in a localized region.

The distribution function  $f(\mathbf{r}, \mathbf{v}, t)$  is a function of seven independent variables. The total time derivative in phase space of  $f$ , denoted as  $\frac{df}{dt} = \left(\frac{\partial f}{\partial t}\right)_{\text{coll}} = I$ , is:

$$I = \frac{\partial f}{\partial t} + \mathbf{v} \cdot \frac{\partial f}{\partial \mathbf{r}} + \mathbf{a} \cdot \frac{\partial f}{\partial \mathbf{v}}. \quad (\text{A.1})$$

Equation of this type represent kinetic equation in a general form. It is usually called the Boltzmann kinetic equation. The left-hand side of the Boltzmann equation is known as the collisional integral. The kinetic equation takes a real meaning only when the form of the collisional integral is found. Collisional integral of Boltzmann kinetic equation is rather complicated a non-linear integro-differential equation depending on seven variables: time,  $t$ , location,  $\mathbf{r}$ , and velocity,  $\mathbf{v}$ . The non-linearity is explicit in the collision integral which explicitly contains products of the distribution function,  $f$ . The acceleration,  $\mathbf{a}$ , may also depend on the distribution function and result in additional non-linear effects.

If we assume ensemble of electrons without collisions (collisional integral is equal to zero) and the electrons are subject only to electromagnetic force ( $\mathbf{F}$ ), and if we assume motion in one dimension only, Eq. A.1 becomes:

$$\frac{\partial f}{\partial t} + v \frac{\partial f}{\partial r} - \frac{\mathbf{F}}{m} \frac{\partial f}{\partial v} = 0. \quad (\text{A.2})$$

where  $m$  is mass of an electron. This equation, collisionless Boltzmann equation widely referred as Vlasov equation<sup>1</sup>, takes into account the long-range, collective interaction between particles, characteristic of a plasma, but neglects close collisions.

<sup>1</sup>In order to comply with the conventions of the plasma-physics community, we shall use the name Vlasov equation in place of collisionless Boltzmann equation. This equation was introduced and explored in 1913 by James Jeans in the context of stellar dynamics, and then rediscovered and explored by Anatoly Alexandrovich Vlasov in 1938 (Vlasov, 1938) in the context of plasma physics. Plasma physicists have

## A.2 Solution of the Vlasov Equation

The Vlasov equation is not easy to solve. First of all, it must be done under the constraint to fulfil Maxwell's equations, because the source terms of Maxwell's equations ( $\rho, \mathbf{J}$ ) are determined by the distribution function, which, in turn, evolves according to the Vlasov equation. Furthermore, the force term in the Vlasov equation is nonlinear. In fact, the Vlasov equation can be solved analytically only for small perturbations when linearization is possible. Thus we start by writing

$$\begin{aligned} f &= f_0 + f_1, & f_1 &\ll f_0 \\ \mathbf{E} &= \mathbf{E}_0 + \mathbf{E}_1, & \mathbf{E}_1 &\ll \mathbf{E}_0 \\ \mathbf{B} &= \mathbf{B}_0 + \mathbf{B}_1, & \mathbf{B}_1 &\ll \mathbf{B}_0 \end{aligned}$$

and equating the first order terms. The general solution is still very difficult, e.g., the solution for homogeneous plasma in a constant background field was not found until 1958 by Bernstein (Bernstein, 1958). Inclusion of inhomogeneities rapidly leads to practically intractable problems. Landau solved the field-free case in 1946 (Landau, 1946). Consider homogeneous, field-free ( $\mathbf{E}_0 = \mathbf{B}_0 = 0$ ) plasma in electrostatic approximation:  $\mathbf{E}_1 = -\nabla\varphi_1$  and  $\mathbf{B}_1 = 0$ . The linearized Vlasov equation is now:

$$\frac{\partial}{\partial t}f_1 + \mathbf{v} \cdot \frac{\partial}{\partial \mathbf{r}}f_1 + \frac{e}{m} \frac{\partial \varphi_1}{\partial \mathbf{r}} \cdot \frac{\partial}{\partial \mathbf{r}}f_0 = 0, \quad (\text{A.3})$$

where electric field is determined self-consistently from the Poisson equation:

$$\frac{\partial}{\partial \mathbf{r}}\mathbf{E}_1 = -4\pi e \int f_1 d^3v. \quad (\text{A.4})$$

Vlasov had attempted to solve these equations at the end of 1930's using Fourier transformations in space and time. He ended up with an integral of type:

$$\int_{-\infty}^{+\infty} \frac{\frac{\partial}{\partial v}f_0}{\omega - kv} dv, \quad (\text{A.5})$$

which has a singularity along the path of integration. Vlasov did not find the correct way of dealing with the singularity. Landau (1946) was the first to realize that because the perturbation must begin at some instant, one should consider the problem as an initial value problem and make a Laplace transform in time, instead of a Fourier transform. After the initial transients of the initial perturbation have faded away at ( $t \rightarrow \infty$ ) and the normal modes of the plasma dominate, the asymptotic solution gives the internal properties of the plasma, i.e., the dispersion equation. A detailed solving procedure of Vlasov equation can be found in many text books. Here, we skip the procedure and write directly the dispersion relation – the dependence of the frequency on the wave number,  $\varepsilon(\omega_0, \kappa) = 0$ :

$$\varepsilon_{\text{Re}}(\omega_0, \kappa)E_0 + i \frac{\partial \varepsilon_{\text{Re}}}{\partial \omega} \frac{\partial E_0}{\partial t} + i \varepsilon_{\text{Im}}(\omega_0, \kappa)E_0 = 0. \quad (\text{A.6})$$

The roots of the equation are complex ( $\omega_0 = \omega'_0 + i\omega''_0$ ). If the imaginary part of the permittivity is greater than 0, the roots lie in the lower part of the complex  $\omega$ -plane, i.e.  $\omega''_0 < 0$ . The quantity  $\gamma = -\omega''_0$  is the damping rate of the wave. A propagating wave exists

---

honored Vlasov by naming the equation after him. For details of this history, see Henon (1982). An electronic reprint version of the original Vlasov's paper from 1938 in Russian can be found in "Uspekhi Fizicheskikh Nauk", 1967, <http://ufn.ru/ru/articles/1967/11/f/> (accessed in Jun 2012), see reference Vlasov (1967).

only if  $\gamma \ll \omega'_0$ : the damping rate must be much less than the frequency. Such a root can be obtained under the assumption of long wavelength, so that

$$\frac{\omega_0}{\kappa} \gg v_{\text{th}} \quad (\text{A.7})$$

If a monochromatic wave is considered  $E(t) = E_0(t)e^{-i\omega_0 t}$  where  $|\partial \ln E_0 / \partial t| \ll \omega_0$ , the solution of dispersion relation (Eq. A.6) is:

$$\varepsilon_{\text{Re}}(\omega_0, \kappa) = 0 \quad (\text{A.8})$$

$$E_0(t) = \hat{E}_0 e^{-\gamma t} \quad (\text{A.9})$$

$$\gamma = \frac{\varepsilon_{\text{Im}}(\omega_0, \kappa)}{\left. \frac{\partial \varepsilon_{\text{Re}}}{\partial \omega} \right|_{\omega=\omega_0}}. \quad (\text{A.10})$$

Damping of the wave  $E_0(t)$  according to equation A.9 (and A.10) is called Landau damping. It is a genuine collective effect which can be inferred only from microscopic kinetic description, while macroscopic approach does not yield the negative imaginary part of the frequency.

The real part of  $\kappa$ -dependent frequency is:

$$\omega_0 \approx \omega_p (1 + 3\kappa^2 \lambda_{\text{De}})^{\frac{1}{2}} \approx \omega_p \left(1 + \frac{3}{2} \kappa^2 \lambda_{\text{De}}\right) \quad (\text{A.11})$$

and the imaginary part  $-\omega''_0 = \gamma$ :

$$\gamma \approx \sqrt{\frac{\pi}{8}} \frac{\omega_p}{|\kappa^3 \lambda_{\text{De}}^3|} \exp\left(-\frac{1}{\kappa^2 \lambda_{\text{De}}^2} - \frac{3}{2}\right). \quad (\text{A.12})$$

These two equations describe the Langmuir waves (plasma waves). Since  $\kappa \lambda_{\text{De}} \ll 1$ , the damping rate,  $\gamma$ , for plasma waves is exponentially small. It increases with decreasing wavelength, and for  $\kappa \lambda_{\text{De}} \sim 1$ , when Eq. A.12 is no longer valid, it becomes of the same order of magnitude as the frequency, so that the concept of propagating plasma wave ceases to be meaningful.



# Pearson's System

## Contents

<b>B.1 Function of Density Distribution . . . . .</b>	<b>73</b>
B.1.1 Uncertainties in $\beta_1$ and $\beta_2$ estimation . . . . .	74
<b>B.2 Probability Density Functions and Transformation Formulas . .</b>	<b>74</b>

## B.1 Function of Density Distribution

In 1895, Pearson defined this distribution system by the following ordinary first order differential equation for the probability density function  $p(x)$ :

$$-\frac{p'(x)}{p(x)} = \frac{b_0 + b_1x}{c_0 + c_1x + c_2x^2} \quad (\text{B.1})$$

where  $b_0, b_1, c_0, c_1$  and  $c_2$  are five real parameters. After normalizing the fraction with any of them, only four independent parameters remain. The form of the solution of this differential equation depends on the value of these parameters, resulting in several distribution types.

The classification of distributions in the Pearson system is entirely determined by the first moment (mean- $\mu_1$ ) and the next three central moments (variance- $\mu_2$ , skewness- $\mu_3$  and kurtosis- $\mu_4$ ). Pearson proposed two dimensionless parameters, i.e. the two moment ratios associated with the square of the skewness ( $\beta_1$ ) and kurtosis ( $\beta_2$ ):

$$\beta_1 = \frac{\mu_3^2}{\mu_2^3}, \quad \beta_2 = \frac{\mu_4}{\mu_2^2}. \quad (\text{B.2})$$

These two parameters characterize the asymmetry and the peakedness of the distribution, respectively, and entirely determine the type of the Pearson distribution system through one parameter,  $\kappa$ , defined as:

$$\kappa = \frac{\beta_1(\beta_2 + 3)^2}{4(2\beta_1 - 3\beta_1 - 6)(4\beta_2 - 3\beta_1)}. \quad (\text{B.3})$$

For  $\kappa < 0$ ,  $0 < \kappa < 1$  and  $\kappa > 1$ , the distributions are called type I, type IV and type VI, respectively. These three cases are known as "the main types" because they occupy areas in the  $(\beta_1, \beta_2)$  space, contrary to the other types which are represented by lines or points. Type III ( $\kappa = \pm\infty$ ) lies on the boundary between type I and type VI. Type V ( $\kappa = 1$ ) lies on the boundary between type IV and type VI. If  $\kappa = 1$ , an additional condition is needed for the classification. The distribution is classified as type II if  $\beta_1 = 0$  and  $\beta_2 < 3$ , type VII if  $\beta_1 = 0$  and  $\beta_2 > 3$ , and as a normal, also known as type XI, if  $\beta_1 = 0$  and  $\beta_2 = 3$ .

When the type of Pearson distribution is specified, all parameters (three or four depending on the type) of its distribution can be determined from the mean, variance, skewness and kurtosis, i.e. from the first four moments.

### B.1.1 Uncertainties in $\beta_1$ and $\beta_2$ estimation

To calculate errors,  $\delta_{\beta_1}$  and  $\delta_{\beta_2}$ , in  $\beta_1$  and  $\beta_2$ , we need to increase  $\beta$  series using moments to the eighth order:

$$\beta_3 = \frac{\mu_3\mu_5}{\mu_2^4}, \quad \beta_4 = \frac{\mu_6}{\mu_2^3}, \quad \beta_5 = \frac{\mu_7\mu_3}{\mu_2^5}, \quad \beta_6 = \frac{\mu_8}{\mu_2^4}. \quad (\text{B.4})$$

For any type of Pearson's system of probability distributions, the errors in  $\beta_1$  and  $\beta_2$  (Pearson, 1902) could be calculated by:

$$\begin{aligned} n\delta_{\beta_1}^2 &= \beta_1(4\beta_4 - 24\beta_2 + 36 + 9\beta_1\beta_2 - 12\beta_3 + 35\beta_1), \\ n\delta_{\beta_2}^2 &= \beta_6 - 4\beta_2\beta_4 + 4\beta_2^3 - \beta_2^2 + 16\beta_1\beta_2 - 8\beta_3 + 16\beta_1, \end{aligned} \quad (\text{B.5})$$

where  $n$  is a number of measurements.

## B.2 Probability Density Functions and Transformation Formulas

As the first part of Tables B.2 to B.4 the explicit forms of the "main" types of Pearson's system probability density functions (p.d.f.) are shown. Also, the population mean (M), variance (V), skewness (S) and kurtosis (K) explicit forms are given. Second part of the tables contains transformation formulas and procedures to obtain parameters of each type from first four sample moments (estimate from data): mean ( $M_s$ ), variance ( $V_s$ ), skewness ( $S_s$ ) and kurtosis ( $K_s$ ). Pearson's type XI, i.e. normal distribution, is shown In Table B.1 as an example of a simple well known distribution.

Table B.1: Type: Pearson XI (normal).

---

Criteria	$\kappa = 0, \beta_1 = 0, \beta_2 = 3$
Domain	$-\infty < x < \infty$
Restriction	$\sigma > 0$
p.d.f.	$\frac{1}{\sigma\sqrt{2\pi}} e^{-\frac{1}{2}\left(\frac{x-\mu}{\sigma}\right)^2}$
Mean	$M = \mu$
Variance	$V = \sigma^2$
Skewness	$S = 0$
Kurtosis	$K = 3$
.....	
Transform.	$\mu = M_s$
	$\sigma = \sqrt{V_s}$

---

Table B.2: Type: Pearson I (beta type I).

---

Criteria	$\kappa < 0$
Domain	$a \leq x \leq a + b$
Restriction	$b > 0$
p.d.f.	$\frac{(x-a)^{p-1}}{b^p B(p, q)} \left[1 - \frac{x-a}{b}\right]^{q-1}$
	$B(p, q)$ is beta function
Mean	$M = a + \frac{bp}{p+q}$
Variance	$V = \frac{b^2 pq}{(p+q+1)(p+q)^2}$
Skewness	$S = \frac{2(q-p)\sqrt{p+q+1}}{(p+q+2)\sqrt{pq}}$
Kurtosis	$K = \frac{3(p+q+1)[2(q^2-pq+p^2)+pq(p+q)]}{(p+q+3)(p+q+2)pq}$
.....	
Transform.	$r = \frac{6(K_s - S_s^2 - 1)}{6 + 3S_s^2 - 2K_s} (< 0)$
	$r_3 = \frac{1}{2}r + \frac{1}{2}r(r+2)\sqrt{\frac{S_s^2}{S_s^2(r+2)^2 + 16(r+1)}}$
	$r_4 = \frac{1}{2}r - \frac{1}{2}r(r+2)\sqrt{\frac{S_s^2}{S_s^2(r+2)^2 + 16(r+1)}}$
	$q = \max[r_3, r_4] \quad (S_s > 0)$
	$q = \min[r_3, r_4] \quad (S_s < 0)$
	$p = \min[r_3, r_4] \quad (S_s > 0)$
	$p = \max[r_3, r_4] \quad (S_s < 0)$
	$b = (p+q)\sqrt{\frac{V_s(p+q+1)}{pq}}$
	$a = M_s - \frac{bp}{p+q}$

---

**Table B.3:** Type: Pearson IV (not related to any distribution).

---

Criteria	$0 < \kappa < 1$
Domain	$-\infty < x < \infty$
Restriction	$\tau > 0, \quad b > \frac{1}{2}$
p.d.f.	$\frac{\Gamma(b + b\delta i)\Gamma(b - b\delta i)\tau^{2b-1} \exp\left[2b\delta \arctan\left(\frac{x-\mu}{\tau}\right)\right]}{\Gamma(b)\Gamma(b - \frac{1}{2})\pi^{\frac{1}{2}} [(x - \mu)^2 + \tau^2]^b}$ <p><math>\Gamma</math> is gamma function</p>
Mean	$M = \frac{b\delta\tau}{b-1} + \mu$
Variance	$V = \frac{\tau^2}{2b-3} \left[1 + \left(\frac{b}{b-1}\delta\right)^2\right]$
Skewness	$S = \frac{2b(2b-3)^{\frac{1}{2}}}{(b-1)(b-2)}\delta \left[1 + \left(\frac{b}{b-1}\delta\right)^2\right]^{-\frac{1}{2}}$
Kurtosis	$K = \frac{3(2b-3)}{(2b-5)} \left[1 + \frac{b+2}{b-2} \left(\frac{b\delta}{b-1}\right)^2\right] \left[1 + \left(\frac{b}{b-1}\delta\right)^2\right]^{-1}$
.....	
Transform.	$b = \frac{9 + 6S_s^2 - 5K_s}{6 + 3S^2 - 2K_s}$ $\tau = \frac{1}{2} \sqrt{V_s[4(2b-3) - S_s^2(b-2)^2]}$ $\delta = \frac{1}{2} \frac{\sqrt{V_s} S_s(b-1)(b-2)}{b\tau}$ $\mu = M_s - \frac{b\delta\tau}{b-1}$

---

Table B.4: Type: Pearson VI (beta type II).

Criteria	$\kappa > 1$
Domain	$x \geq a$ , (Skewness $> 0$ ) $x \leq a$ , (Skewness $< 0$ )
Restriction	$\alpha > 0, \beta > 0, m > 0$
p.d.f.	$\frac{\alpha^m(x-a)^{\beta-1}}{B(\beta, m)(\alpha+x-a)^{m+\beta}}, \text{ (Skewness } > 0)$ $\frac{\alpha^m(a-x)^{\beta-1}}{B(\beta, m)(\alpha-x+a)^{m+\beta}}, \text{ (Skewness } < 0)$ <p><math>B(\beta, m)</math> is beta function</p>
Mean	$M = a + \frac{\alpha\beta}{m-1}, \text{ (Skewness } > 0)$ $M = a - \frac{\alpha\beta}{m-1}, \text{ (Skewness } < 0)$
Variance	$V = \frac{\alpha^2(m+\beta-1)\beta}{(m-1)^2(m-2)}$
Skewness	$S = \frac{2(2\beta+m-1)\sqrt{m-2}}{(m-3)\sqrt{\beta(\beta+m-1)}}, \text{ (Skewness } > 0)$ $S = -\frac{2(2\beta+m-1)\sqrt{m-2}}{(m-3)\sqrt{\beta(\beta+m-1)}}, \text{ (Skewness } < 0)$
Kurtosis	$K = \frac{6\{[\beta^2 + (\beta+m-1)^2](m-2) + \beta(\beta+m-1)(m-1)\}}{(m-4)(m-3)\beta(\beta+m-1)}$
.....	
Transform.	$r = \frac{6(K_s - S_s^2 - 1)}{6 + 3S_s^2 - 2K_s} (< 0)$ $r_1 = \frac{1}{2}(r-2) + \frac{1}{2}r(r+2)\sqrt{\frac{S_s^2}{S_s^2(r+2)^2 + 16(r+1)}}$ $r_2 = \frac{1}{2}(r-2) - \frac{1}{2}r(r+2)\sqrt{\frac{S_s^2}{S_s^2(r+2)^2 + 16(r+1)}}$ $\beta = \max[r_1, r_2] + 1 \quad m = \min[r_1, r_2] - \beta$ $\alpha = \sqrt{\frac{V_s(m-1)^2(m-2)}{(m+\beta-1)\beta}}$ $a = M_s - \frac{\alpha\beta}{m-1}, \text{ (Skewness } > 0)$ $a = M_s + \frac{\alpha\beta}{m-1}, \text{ (Skewness } < 0)$

# STEREO TDS Observations

---

## Contents

---

<b>C.1 LW Associated with <i>in situ</i> Type III Radio Bursts . . . . .</b>	<b>79</b>
--	-----------

---

## C.1 STEREO TDS observations of LW associated with *in situ* type III radio bursts

STEREO, the third mission in NASA's Solar Terrestrial Probes, consists of two nearly identical spacecrafts (A-ahead and B-behind). Both spacecraft have been launched on October 26, 2006. After series of highly eccentric Earth orbits followed by close flybys of the moon two STEREO escape into orbits about the Sun near 1 AU in the ecliptic. Finally STEREO-A moves ahead of the Earth whereas STEREO-B trails behind. Two STEREO separate at  $\sim 54^\circ$  per year with respect to the Sun.

The Time Domain Sampler (TDS), part of S/WAVES instrument onboard STEREO spacecrafts, makes rapid samples of waveforms and is intended primarily for the study of Langmuir waves, waves at the plasma frequency and the precursors of type II and III radio bursts. The rapid simultaneous sampling of three orthogonal antennas as well as a pseudo-dipole channel obtained by taking the difference of any two monopoles allows the study of waveforms, their distortions, and, through ground-based Fourier analysis, a frequency determination which is far more accurate than any possible onboard filter analysis system. The TDS provides rapid sampling of transient events in the time domain. Its objective is to make very fast samples while also making effective use of the telemetry downlink. The maximum continuous sampling speed of the TDS is 16 million bits per second. The typical TDS share of the S/WAVES downlink rate is only about 500 bits per second. The TDS achieves that large reduction in bit-rate while maintaining high scientific return by choosing events for transmission to the ground intelligently. This introduces an inevitable bias into received data. However, the TDS data from STEREO S/WAVES experiment are used to get starting idea about the amplitude distribution of Langmuir wave packets and the distribution of its temporal width, so they can be used in the simulations, Sec. 2.4. The selection of the wave packets from STEREO TDS waveform sampler was done in following manner:

- TDS data from 2008 - 2011 are used. The first year of STEREO mission data is omitted to avoid Earth's foreshock events.
- Fourier transformation from temporal (131 ms) into frequency domain is done; if a significant increase between 5 and 65 kHz exists, the event is selected as possible Langmuir wave packet. The range of the frequencies corresponds to the range of plasma frequencies at 1AU.

- From STEREO A, 2283 events were selected in such a way, and from STEREO B, 2414.
- Fig. C.1 shows eight TDS wave packages randomly chosen from 2283 STEREO A events.
- To make a decision if particular Langmuir packets are associated with type III bursts or not, a histogram with 1 hour bins is constructed. If the number of selected Langmuir packets in one bin (1 hour) was greater than 10, all Langmuir packets in that hour are selected and considered as Langmuir wave packets associated with type III bursts (maybe the word “associated” is not the most suitable, maybe is better to say “Langmuir waves during type III radio bursts”).
- The number 10, as a decision limit, is determined empirically.
- From the 2283 STEREO A events – 780 were selected, and, from 2414 STEREO B events – 295.
- Finally, only the more numerous set of 780 events recorded by STEREO A is taken into consideration for the further analysis, hence the statistics will be with more confidence.

A histogram of maximums of Langmuir waves electric field is presented in Fig. 2.6. The electric field is scaled to  $\Gamma L_{\text{eff}} = 1.3 \text{ m}$ . The red line presents the best linear (in log scale) or power-law (in linear scale) fit:  $f(E) = aE^b$ . The index  $b$  is found to be  $-1.83$  with 95% confidence interval of  $[-1.91, -1.75]$  and coefficient of determination  $r^2 = 0.96$ . The fitting procedure is performed in linear scale and six leftmost points ( $E \leq 4.6 \frac{\text{mV}}{\text{m}}$ ) were excluded to avoid bias in the distribution due to the low signal intensities (recall that only the most intense wave forms are transmitted to the Earth). Vertical dashed line is drawn at  $E \approx 8 \frac{\text{mV}}{\text{m}}$  dividing the energy range into two areas: greater than  $8 \frac{\text{mV}}{\text{m}}$  where we have quite good linear approximation (even though the selection criteria could have deficiencies), and the area of lower energies, less than  $8 \frac{\text{mV}}{\text{m}}$ , where we actually do not know the distribution of the Langmuir waves amplitudes. This is because of the instrumental limitations: in flight software criteria determine the effective quality of each event and, in general, the events with the highest “quality” are selected for transmission to the ground; with changes in flight software, the quality determination could be any arithmetic evaluation of the event. In this way, the “best” events are sent to the ground. Usually it means that low amplitude events are considered as a part of background noise and they are not selected for the transmission to the ground.

A normalized histogram of temporal width of LW packages at half maximum is presented in Fig. 2.7. The histogram data are fitted by Pearson type I probability distribution:  $\mathcal{P}(m = 26 \text{ mV}, \sigma = 14 \text{ mV}, \beta_1 = 0.5, \beta_2 = 2.8)$ . Automatized determination of the temporal width of LW packages at half maximum is illustrated in eight randomly chosen examples of wave packages in Fig. C.1 (red line). The way of the determination, being imprecise, causes an inaccuracy in right part of the histogram – at greater values of the width (see for example four lower panels of the Fig. C.1).

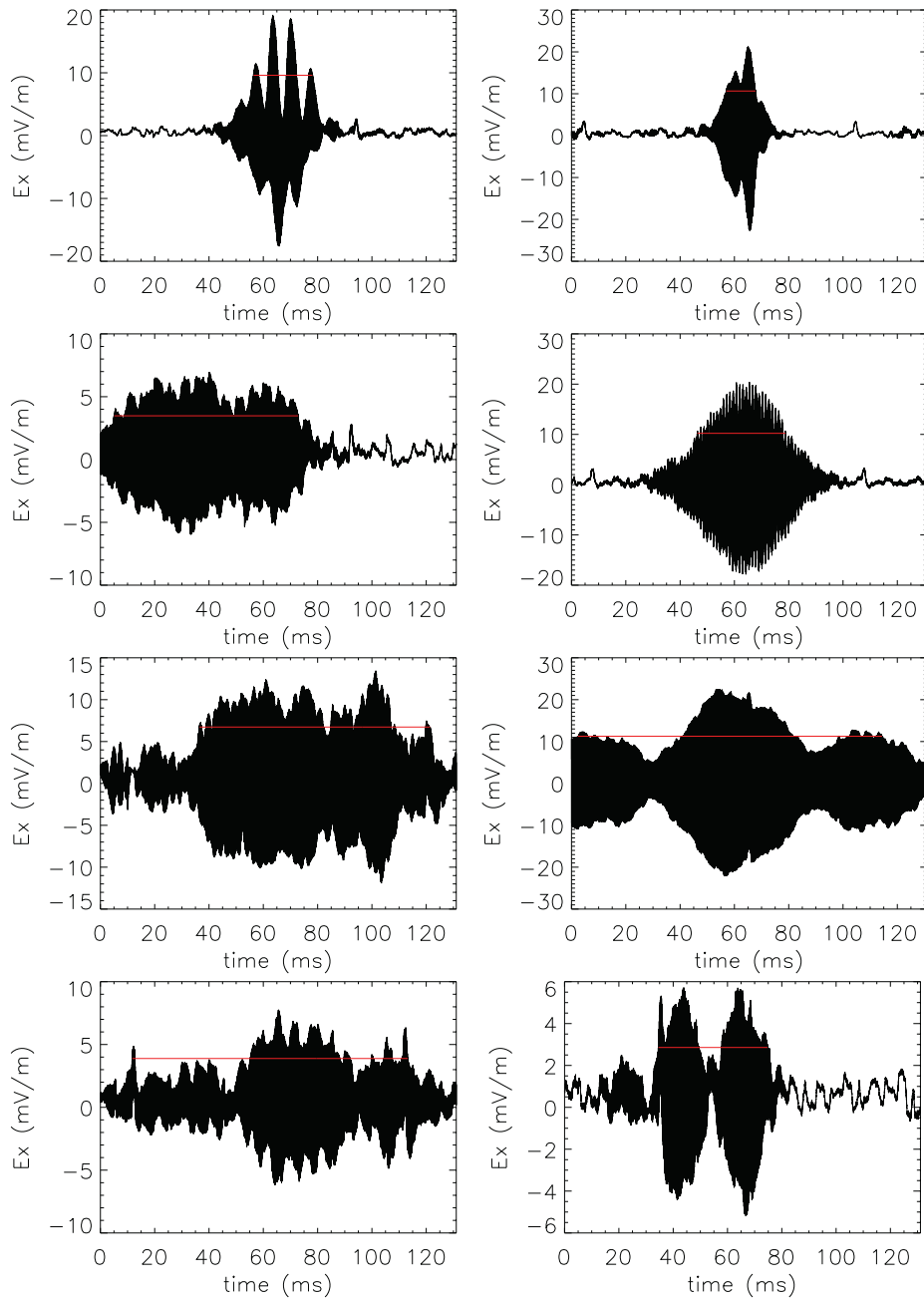


**Figure C.1:** Typical examples of LW snapshots as observed by the TDS onboard STEREO/WAVES. The red lines represent the temporal widths of half maximum size. (Figures provided by courtesy of Arnaud Zaslavsky.)



# Background Removal – Pseudocode

## Contents

<b>D.1 Background Removal</b> . . . . .	<b>83</b>
<b>D.2 Pseudocode</b> . . . . .	<b>85</b>

## D.1 Background Removal

The task of identifying and removing the background noise from the signal is usually done by interactive time consuming hand marking procedure. In order to speed up this task we developed a quick automated heuristic procedure depending only on few parameters which are to be chosen empirically. Due to the automatization, trying several parameters to find the best one is also much less time consuming than the traditional procedure.

The background signal has some fluctuations on log scale graph bounded by some value which can be estimated from the graph. We denote this upper limit of fluctuations by BGWidthTol. Further, on the graph we can identify time intervals where only the background signal is present. Our heuristics looks for those time intervals. In a single time point we shall assume that only the background is present if in a neighborhood of that point (nRadiusBG points to left and to the right) maximal difference of signal values is not greater than BGWidthTol. Consecutive background points form a background interval. After we identified background intervals we first mollify this signal by simple moving average method with radius of nRadiusMA1 points. Next we connect those background graph pieces by interpolating linearly between the background time intervals. After mollifying the whole graph again using nRadiusMA2 we get a good smooth approximation of the background signal. Finally, we shift the whole graph by some value Shift and consider all points lying under the shifted graph to be background signal.

To identify and remove background from the observations of Langmuir waves, the following heuristic algorithm was applied for every event separately. Firstly, on the overall time interval of the event, we identify short time intervals when only the background signal is present. We calculate, in a narrow moving time window, the difference between the maximal and the minimal signal level. The time window is determined by the parameter nRadiusBG, line 02 in pseudocode; if we choose nRadiusBG to be equal 2, the width of the window will be 5 data points - two on the left plus two on the right side of the point. These five points in time scale correspond to an interval of about 20 or 35 seconds depending on resolution of the data, i.e. on the operational mode of the TNR instrument (about 4 or 7 seconds). We assume that the signal is part of the background if this difference is less than an empirically chosen parameter (BGWidthTol, line 02 in pseudocode) carefully tuned for each event and representing the background typical fluctuations (lines 03-09 in pseudocode).

Function `isBG` with parameter `BGWidthTol` was used to identify points belonging to the background. Depending on the shape and value of the background fluctuations, this parameter takes values from the interval  $[0.05, 0.4]$  in logarithmic scale (for the example shown in Fig. 2.2, the value of this parameter is 0.1). Secondly, in each identified background time interval (line 10 in pseudocode), the signal is mollified–smoothed by moving average method (`MovAvg` with `nRadiusMA1` points, lines 11-15 in pseudocode) and linearly interpolated to the whole time domain (lines 16-22 in pseudocode). Finally, after a second mollification (`MovAvg` with `nRadiusMA2` points, lines 23-25 in pseudocode), this approximation of the average noise level is shifted by a value `Shift`, introduced in line 02, again empirically chosen and carefully tuned for each event, that represents the upper limit of what we considered to be the background level (lines 26-28 in pseudocode). The values of this parameter belong to the interval  $[0.1, 0.3]$  in logarithmic scale (for the example shown in Fig. 2.2, the value of this parameter is 0.15). As an example the red line plotted in Figure 2.2 represents the level of background noise determined in described way.

## D.2 Pseudocode

The proposed heuristic procedure can be formalised in a following pseudocode.

Algorithm for background removal	
	<i>/* Initialization */</i>
01	Read a vector Data of nData noisy data values
02	Choose parameters nRadiusBG, BGWidthTol, nRadiusMA1, nRadiusMA2, Shift
	<i>/* Identify BG points and intervals */</i>
03	<b>for</b> i=1 <b>to</b> nData
04	<b>if</b> isBG(Data, i, nRadiusBG, BGWidthTol) <b>then</b>
05	DataBGpoint(i) := true
06	<b>else</b>
07	DataBGpoint(i) := false
08	<b>endif</b>
09	<b>next</b> i
10	Determine intervals $[l_k, r_k], 1 \leq k \leq K$ of data points where DataBGpoint(i) = true for $l_k \leq i \leq r_k$
	<i>/* Motify data in BG intervals */</i>
11	<b>for</b> k=1 <b>to</b> K
12	<b>for</b> i= $l_k$ <b>to</b> $r_k$
13	BGlevel(i) := MovAvg(Data, i, nRadiusMA1)
14	<b>next</b> i
15	<b>next</b> k
	<i>/* Linearly interpolate between BG intervals */</i>
16	<b>for</b> k=1 <b>to</b> K-1
17	L := BGlevel( $r_k$ )
18	R := BGlevel( $l_{k+1}$ )
19	<b>for</b> i= $r_k + 1$ <b>to</b> $l_{k+1} - 1$
20	BGlevel(i) := L + (R-L)*( $i-r_k$ )/( $l_{k+1}-r_k$ )
21	<b>next</b> i
22	<b>next</b> k
	<i>/* Motify all BG data points */</i>
23	<b>for</b> i=1 <b>to</b> nData
24	BGlevel(i) := MovAvg(BGlevel, i, nRadiusMA2)
25	<b>next</b> i
	<i>/* Shift BG data points */</i>
26	<b>for</b> i=1 <b>to</b> nData
27	BGlevel(i) := BGlevel(i) + Shift
28	<b>next</b> i
	<b>Stop.</b> Result is in vector BGlevel

```
function isBG(Data, i, nRadiusBG, BGWidthTol)
    /* Initialization */
01 Determine MinVal as a minimal value of Data(j)
   for  $j \in [i - nRadiusBG, i + nRadiusBG]$ 
02 Determine MaxVal as a maximal value of Data(j)
   for  $j \in [i - nRadiusBG, i + nRadiusBG]$ 
03 if MaxVal - MinVal > BGWidthTol then
04     return false
05 else
06     return true
07 endif
    Stop
```

# Publications

---

## Contents

<b>E.1</b>	<b>Vidojevic et al., 2010</b> . . . . .	<b>87</b>
<b>E.2</b>	<b>Vidojevic et al., 2011</b> . . . . .	<b>92</b>
<b>E.3</b>	<b>Maksimovic et al., 2011</b> . . . . .	<b>97</b>
<b>E.4</b>	<b>Vidojevic and Maksimovic, 2009</b> . . . . .	<b>102</b>

---

## E.1 Vidojevic et al., 2010

Article published in March 2010 in *Twelfth International Solar Wind Conference*

**Title:** Langmuir Waves and Type III Bursts Observed by the Wind Spacecraft

**List of authors:** Vidojević, S. and Zaslavsky, A. and Maksimovic, M. and Atanacković, O. and Hoang, S. and Hoang, S. and Nguyen, Q. N.

**Reference:** Vidojević, S. and Zaslavsky, A. and Maksimovic, M. and Atanacković, O. and Hoang, S. and Hoang, S. and Nguyen, Q. N. Langmuir Waves and Type III Bursts Observed by the Wind Spacecraft, *Twelfth International Solar Wind Conference*. AIP Conference Proceedings, **1216**, pp. 292-295 (2010)

## Langmuir Waves and Type III Bursts Observed by the Wind Spacecraft

Sonja Vidojević<sup>\*,†</sup>, Arnaud Zaslavsky<sup>\*</sup>, Milan Maksimovic<sup>\*</sup>, Olga Atanacković<sup>†</sup>,  
Sang Hoang<sup>\*</sup> and Q. N. Nguyen<sup>\*</sup>

<sup>\*</sup>LESIA Observatoire de Paris, Section de Meudon, 5, place Jules Janssen, Meudon Cedex, 92195 France

<sup>†</sup>Department of Astronomy, Faculty of Mathematics, University of Belgrade, Studentski trg 16,  
11000 Belgrade, Serbia

**Abstract.** Interplanetary electron beams, produced by CMEs and flares, are unstable in the solar wind and generate Langmuir waves at the local plasma frequency or its harmonic. Radio observations of those waves in the range 4 kHz – 256 kHz from the WAVES experiment onboard the WIND spacecraft have been statistically analyzed. A subset of 17 events has been selected for this study. The background consisting of thermal noise, type III bursts and Galactic background has been removed and the histogram of the remaining power spectral density has been fitted by Pearson’s system of distributions.

**Keywords:** Langmuir waves, Type III bursts, Fitting by Pearson’s system.

**PACS:** 96.60.Vg, 95.85.Bh, 95.75.Pq.

### INTRODUCTION

An important problem in plasma physics and solar physics is the generation of non thermal radio emissions. Intense radio emissions are generated in numerous regions of the solar system, including the solar corona, the solar wind and regions near shock waves. Few basic generation mechanisms are currently believed to be responsible for these emissions. We are interested in one of them, often called “plasma emission” or “radiation at multiples of the plasma frequency”, first proposed by Ginzburg & Zheleznyakov [3], which is responsible for type III solar radio bursts generation. This mechanism has been further refined by numerous investigators. Type III solar radio bursts are produced by fast energetic electrons ( $v \approx 0.03$  to  $0.3$  c) which are accelerated in the low corona during a violent event (e.g. solar flare or coronal mass ejection) and travel outward along magnetic field lines through the high corona and interplanetary space. Because the faster electrons run ahead of the slower ones, a “bump on tail” distribution arises which is unstable to the production of electron plasma waves. These plasma waves, also called Langmuir waves, then produce the observed electromagnetic radiation, the type III bursts, either at the fundamental,  $f = f_p$ , or the second harmonic  $f = 2f_p$ , or both. Around 1 AU the typical plasma frequencies range between 10 and 50 kHz. The electron beams, Langmuir waves and radio emissions have all been observed in situ and studied in detail by numerous authors (e.g., Gurnett & Anderson [4], Lin et al., [5], Ergun et al. [2] etc.).

To explain the observed electric field distribution Robinson [9] developed a theory, named stochastic

growth theory (SGT), on the assumption that the LW wave growth rate is randomly fluctuating. This hypothesis is based on the fact that waves and electrons are interacting in an inhomogeneous plasma environment. Assuming that the effective number of growth rate fluctuations is large enough, the central limit theorem can be applied. A consequence of the SGT is that the probability distribution of the logarithm of wave energy density should be Gaussian. Langmuir waves in the Earth’s electron foreshock observed by the CLUSTER spacecraft have been statistically studied by Musatenko et al. [7]. They showed that the observed distributions for the logarithm of the wave intensities belong to Pearson system of distributions rather than being normal. This disagreement with the SGT prediction could be a result of an insufficient number of growth rate fluctuations in the typical Earth’s electron foreshock conditions, so that the central limit theorem can not be applied.

Our aim is to perform a similar study and examine statistically Langmuir waves associated with type III solar bursts observed by the Wind spacecraft out of Earth’s bow shock.

### OBSERVATIONS

The WAVES experiment on the Wind spacecraft, launched in 1994, provide comprehensive measurements of the radio and plasma wave phenomena. Analysis of these measurements help us to understand the kinetic processes at work in the solar wind. A detailed description about the WAVES experiment and corresponding instruments can be found in Bougeret et

**TABLE 1.** List of sample events. Calendar date is represented in form YYYYMMDD (year, month, day), approximate starting time (UT),  $t$ , of Langmuir waves in form hh:mm (hour, minute) and approximate plasma frequency,  $f_p$ , in kHz.

No	Date	$t$	$f_p$	No	Date	$t$	$f_p$
1	19950402	12:00	25	10	20000504	11:30	20
2	19971123	14:30	13	11	20010604	17:30	18
3	19971130	12:40	25	12	20010625	09:30	13
4	19980712	02:00	15	13	20021019	22:00	18
5	19990107	00:30	22	14	20021020	14:30	13
6	19990110	05:40	13	15	20021021	05:00	13
7	19990129	15:40	25	16	20030401	00:40	18
8	19990216	03:30	13	17	20030413	10:00	18
9	19990220	05:00	10				

al. [1]. In our study we use data of the two multi-channel receivers, thermal noise receivers (TNR), which cover the frequency range from 4 kHz to 256 kHz in 5 logarithmically-spaced frequency bands. Each band covers 2 octaves with one octave overlap. Each of these bands is divided into either 32 or 16 logarithmically-spaced channels. TNR provides rapid measurements of plasma electric field (every 1.5 s or half spacecraft spin).

The Langmuir waves that are converted into electromagnetic waves, type III bursts, can then be observed with the two radio receivers RAD1 and RAD2 in the frequency range from 20 kHz to 14 MHz.

Type III solar bursts are easily recognizable on dynamical spectra plots, they have fast, nearly vertical, frequency drifts from higher to lower frequencies. Looking at dynamical spectra we can see a lot of type III bursts, but only rarely do the generating electrons pass over the spacecraft instruments so that we can observe the Langmuir waves directly, in situ. From 1994 to the end of 2009 a subset of 17 events where Langmuir waves and type III bursts are associated has been selected (Table 1).

The criteria that were used in the selection of the associated type III bursts were the following: (1) the burst should be isolated in time from other bursts, (2) the intensity of the burst radiation should be much above the background, and (3) the burst should be present in a majority of frequencies. The first criterion ensures that the radio emission is related to a single package of electrons. The second and third criteria restrict the analysis to the bursts which permit an accurate measurement of the parameters. We take into account only events where impulsive electron fluxes were observed with the full three-dimensional (3-D) plasma and energetic particle (electrons and ions) experiment (Lin et al. [6]) onboard also WIND spacecraft. This experiment is designed to measure the full three-dimensional distribution of suprathermal electrons and ions at energies from a few eV to over several hundreds keV. We have also checked association

of our events with solar flares occurrence. For 11 events (#1, #8–#17), according to *Solar–Geophysical Data* publication, good association with solar flares (recorded in  $H_\alpha$  spectral line) exist.

## ANALYSIS

The stochastic growth theory (SGT) describes situations in which an unstable distribution of particles interacts self-consistently with its driven waves in an inhomogeneous plasma environment and evolves to a state in which the particle distribution fluctuates stochastically about a state close to time and volume averaged marginal stability. These fluctuations drive waves so that the wave gain,  $G = 2 \ln(E/E_0)$ , is a stochastic variable. The wave gain is the time integral of the wave energy density growth rate and it is related to the wave electric field,  $E(t)$ , by  $E^2(t) = E_0^2 \exp[G(t)]$  where  $E_0$  is a constant field. The observed electric field,  $E$ , is a consequence of a large number of amplifications and damping:

$$E = E_0 \prod_{i=1}^N e^{G_i}, \quad N \gg 1, \quad (1)$$

where  $G_i$  (gain) is a stochastic variable. Taking the logarithm of this equation one obtains:  $\log E = \log E_0 + \sum_{i=1}^N G_i$ . The central limit theorem can then be applied to the probability distribution of  $\log E$  which is thus a normal distribution (e.g. Robinson [9]).

In order to see if the Langmuir waves associated with Type III solar bursts satisfy predictions of the SGT, we have undertaken the following steps. We have integrated the power spectral density ( $S_t$ , index  $t$  denotes a certain moment of time) of Langmuir waves through a narrow interval of frequencies ( $f_1, f_2$ ) around the local plasma frequency ( $f_p$ )

$$P_{LW,t} = \int_{f_1}^{f_2} S_t df, \quad f_1 < f_p < f_2. \quad (2)$$

The integration is done numerically by a trapezium method. In that way we obtain the total power of the Langmuir waves at a given moment of time ( $P_{LW,t}$ ). As an example the 2003 April 1<sup>st</sup> event is represented on Fig. 1. The histogram of the total power of Langmuir waves is shown in Fig. 2.

Then, in a semiautomatic way, we removed the background consisting of the thermal noise, the type III radio burst and the galactic background. The blue line on Fig. 1, obtained by cubic spline interpolation between manually selected points (red crosses), represent the level of total background. From the remaining data we made new histogram, displayed on Fig. 3, and fit it with a normal probability distribution (blue line in Fig. 3). The error

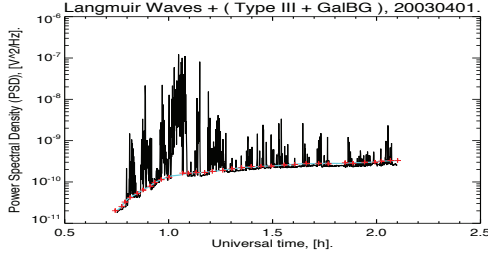


**FIGURE 1.** Power of Langmuir waves before removing background. Red crosses are selected manually. They are connected by cubic spline interpolation, the blue line.

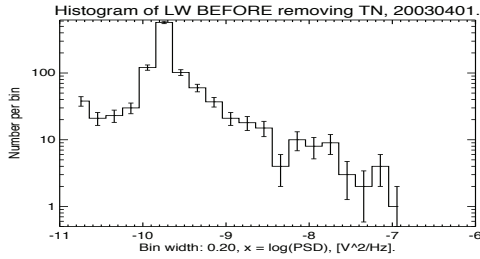


**FIGURE 2.** Histogram before removing background.

bars on both histograms are calculated as standard deviation of counting statistics, i.e. the Poisson distribution. To find a better approximation for the probability functions we have applied a family of distributions proposed by Pearson [8].

### Applying Pearson's system of distributions

The Pearson's system of distributions is a reasonable choice to be applied on empirical data in order to find better approximations of the probability density func-

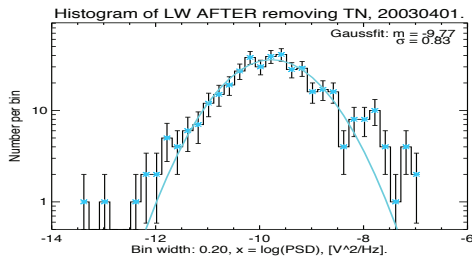


**FIGURE 3.** Histogram after removing background. The blue line represent fit with a Log-normal probability distribution.

tions. It can represent a wide class of distributions with a wide variety of shapes and provides thus more accurate representations of the observed data. Some well known distributions (e.g. normal, beta, gamma, Student's t-distribution etc.) belong all to the Pearson's system. Pearson [8] defined the Pearson distribution system by the following ordinary differential equation of the first order with respect to the probability density function  $p(x)$ :

$$\frac{p'(x)}{p(x)} = \frac{b_0 + b_1x}{c_0 + c_1x + c_2x^2} \quad (3)$$

where  $b_0, b_1, c_0, c_1$  and  $c_2$  are real coefficients.

The classification of distributions inside the Pearson system is entirely determined by the first moment – mean ( $\mu_1$ ), and next three moments around the mean ( $\mu_2, \mu_3$  and  $\mu_4$ ). For classification Pearson proposed two dimensionless parameters, the two moment ratios associated with the concepts of square of skewness ( $\beta_1$ ) and kurtosis ( $\beta_2$ ):

$$\beta_1^2 = \frac{\mu_3^2}{\mu_2^3}, \quad \beta_2 = \frac{\mu_4}{\mu_2^2}. \quad (4)$$

These two parameters characterize the peakedness and the asymmetry of the distribution, respectively. Their values can be obtained from observations. We apply Pearson's system of distributions to all 17 histograms. We find that our 17 events belong to only 3 types of Pearson's distributions: to the type I (beta), IV (not related to any standard distribution) and VI (beta prime). The positions of our 17 events in the  $\beta_1^2 - \beta_2$  plane are shown in Fig. 4. Most of the events are close to a normal distribution, which is represented by the point  $(\beta_1^2, \beta_2) = (0, 3)$ . To see whether they are really different from a normal distribution, i.e. if the point  $(0, 3)$  lies within the uncertainty limits of the events, we used two methods to evaluate the error-bars in  $\beta_1^2$  and  $\beta_2$ : a Monte Carlo simulation and a method of moments proposed by Karl Pearson [8]. The uncertainties calculated by the latter method are greater than the one obtained by the Monte Carlo simulation, we used therefore the greater values in the following. Error bars shown on the Fig. 4 are thus calculated by the method of moments. It is found that the point  $(0, 3)$  has a 'strong' intersection with only two of the uncertainty intervals (blue diamonds), and has a 'weak' intersection with three intervals (green crosses), just at the very limits of uncertainty. Out of 17 events 12 have no intersection with the normal distribution which is predicted by the SGT. This result indicates that the SGT possibly requires additional verifications and examinations.

For all the 17 events the goodness of fit for both Pearson's type I, IV and VI and the normal distribution is tested with the statistical hypothesis test  $\chi^2$  with a 95% confidence interval and in all cases a better result is found for the Pearson's system of distributions.

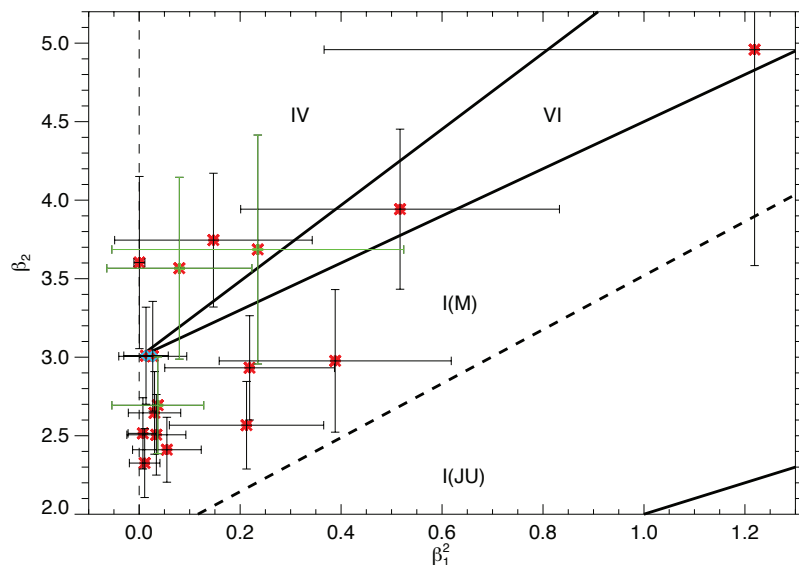


FIGURE 4. Beta plane. Out of the 17 events: 11 belong to Pearson's type I, 2 to type VI and 4 to type IV probability distribution.

## CONCLUSIONS

We have examined 17 time intervals containing intense locally formed Langmuir waves that are associated with type III radio bursts. We have shown that the probability distributions of the power of these waves belong to three different types of Pearson's probability distributions: type I, type IV and type VI. In order to compare the goodness of the fits,  $\chi^2$  tests have been realized, showing for all of the considered events that the Pearson's probability distributions are fitting better the data than Gaussian ones. This is in contradiction with the Stochastic Growth Theory which predicts Log-normal distributions for the power of the Langmuir waves. The uncertainty analysis that has been performed also goes in favor of the use of Pearson's system of distributions to fit the data.

Nevertheless, we should mention that our current results are still preliminary and still need to be confirmed in several ways. Firstly, we need to enlarge the number of events so that the statistical results will be more reliable. Secondly, we need to verify that the background has been correctly removed, since the parameters  $\beta_1^2$  and  $\beta_2$  are very sensitive to the level and the shape of the removed background. Finally we plan to compute the effect of the receiver integration time (of the order of seconds) on the analyzed spectra, as it is now known that the actual Langmuir waves electrostatic fields are formed of packets of the order of 10 to 80 ms.

If the results of our analysis are still robust to the latter

improvements, then the reasons for the disagreement of the observed distributions with the stochastic growth theory predictions should be investigated.

## ACKNOWLEDGMENTS

This work was supported by a grant from the french government and the French Embassy in Belgrade. At the Observatoire de Paris, the WIND/WAVES investigation was supported by both CNES and CNRS.

## REFERENCES

1. J.-L. Bougeret, et al., *Space Science Reviews* **71**, 231 (1995)
2. R. E. Ergun, D. Larson, R. P. Lin et al., *Astrophysical Journal*, **503** 435 (1998)
3. V. L. Ginzburg, V. V. Zheleznyakov, *Soviet Astronomy* **2**, 653–678 (1958)
4. D. A. Gurnett and R. R. Anderson, *Science*, **194**, 1159 (1976)
5. R. P. Lin, D. W. Potter, D. A. Gurnett, et al., *Astrophysical Journal*, **251**, 364 (1981)
6. R. P. Lin, K. A. Anderson, S. Ashford, et al., *Space Science Reviews*, **71**, 125 (1995)
7. K. Musatenko, V. V. Lobzin, J. Soucek et al., *Planetary and Space Science*, **55** 2273 (2007)
8. K. Pearson, *Philosophical Transactions of the Royal Society*, **A 186** 343–414 (1895)
9. P. A. Robinson, *Solar Physics*, **146** 357 (1993)

## E.2 Vidojevic et al., 2011

Article published 2011 in *Baltic Astronomy*

**Title:** Statistical Analysis of Langmuir Waves Associated with Type III Radio Bursts: I. Wind Observations

**List of authors:** Vidojević S., Zaslavsky A., Maksimović M., Dražić M. and Atanacković O.

**Reference:** Vidojević S., Zaslavsky A., Maksimović M., Dražić M. and Atanacković O. Statistical Analysis of Langmuir Waves Associated with Type III Radio Bursts: I. Wind Observations, *Baltic Astronomy*, **20**, pp. 596-599, (2011)

*Baltic Astronomy, vol. 20, 596–599, 2011*

## STATISTICAL ANALYSIS OF LANGMUIR WAVES ASSOCIATED WITH TYPE III RADIO BURSTS: I. WIND OBSERVATIONS

S. Vidojević<sup>1,2</sup>, A. Zaslavsky<sup>1</sup>, M. Maksimović<sup>1</sup>, M. Dražić<sup>2</sup> and O. Atanacković<sup>2</sup>

<sup>1</sup> *LESIA – Observatoire de Paris, CNRS, UPMC, Université Paris 06, Université Paris-Diderot, 5 Place Jules Janssen, 92195 Meudon, France; sonja.vidojevic@obspm.fr*

<sup>2</sup> *Faculty of Mathematics, University of Belgrade, Studentski trg 16, 11000 Beograd, Serbia*

Received: 2011 August 8; accepted: 2011 August 15

**Abstract.** Interplanetary electron beams are unstable in the solar wind and they generate Langmuir waves at the local plasma frequency or its harmonic. Radio observations of the waves in the range 4–256 kHz, observed in 1994–2010 with the WAVES experiment onboard the WIND spacecraft, are statistically analyzed. A subset of 36 events with Langmuir waves and type III bursts occurring at the same time was selected. After removal of the background, the remaining power spectral density is modeled by the Pearson system of probability distributions (types I, IV and VI). The Stochastic Growth Theory (SGT) predicts log-normal distribution for the power spectrum density of the Langmuir waves. Our results indicate that SGT possibly requires further verification.

**Key words:** Sun: wind, flares, radio radiation, Langmuir waves

### 1. INTRODUCTION

We used the measurements obtained by four different experiments on-board the Wind spacecraft – a laboratory for long-term solar wind measurements, launched on 1994 November 1. Our focus is on radio observations obtained by the WAVES experiment (Bougeret et al. 1995). In the study of locally generated Langmuir waves we use the data from two multi-channel thermal-noise receivers (TNR), which cover the frequency range from 4 kHz to 256 kHz in five logarithmically-spaced frequency bands. Each band covers two octaves with one octave overlap. Each of these bands is divided to either 32 or 16 logarithmically-spaced channels. TNR provides rapid measurements of the plasma electric field. The Langmuir waves that are converted to electromagnetic waves – type III bursts, can then be observed with two radio receivers, RAD1 and RAD2. The RAD1 frequency range, from 20 to 1040 kHz, is divided into 256 linearly spaced channels of 3 kHz bandwidth each. The frequency range of the RAD2 radio receiver, from 1075 to 13825 kHz, is divided in the same number of channels as RAD1, but with 20 kHz bandwidth.

For the selection of sample events (Figure 1) we used: (1) one minute averaged measurements of interplanetary magnetic field vector in the Geocentric Solar Ecliptic (GSE) cartesian coordinates from Magnetic field investigation (MFI), Lepping et al. (1995); (2) for the particle measurements, i.e., for the full three-dimensional distribution of suprathermal electrons and ions, we used the 3-D Plasma and Energetic Particle Investigation (3DP) experiment, Lin et al. (1995); (3) for the solar wind velocity we used the data from the Solar Wind Experiment (SWE), Ogilvie et al. (1995) which provides three-dimensional velocity, density and temperature of the solar wind ions. As the solar wind velocity, we used proton velocity averaged over the time interval when our events occurred. The measurements, taken simultaneously by the four experiments, allow a qualitative analysis of the events.

In order to remove the background from the TNR observations consisting of thermal noise, type III bursts and Galactic background, we have developed a heuristic algorithm based on numerical techniques with a few parameters only.

## 2. ANALYSIS, THE PEARSON SYSTEM OF DISTRIBUTIONS

Karl Pearson (1895) defined a distribution system by the following equation for the probability density function  $p(x)$ :

$$-\frac{p'(x)}{p(x)} = \frac{b_0 + b_1x}{c_0 + c_1x + c_2x^2},$$

where  $b_0$ ,  $b_1$ ,  $c_0$ ,  $c_1$  and  $c_2$  are real parameters. The form of solutions of this differential equation depends on the parameter values, resulting in several distribution types. The classification of distributions in the Pearson system is entirely determined by the two moment ratios, square of skewness,  $\beta_1$ , and kurtosis,  $\beta_2$ :

$$\beta_1 = \frac{\mu_3^2}{\mu_2^3}, \quad \beta_2 = \frac{\mu_4}{\mu_2^2}.$$

The coefficients of the probability distributions were calculated by using the following methods: the method of moments and the maximum likelihood estimation method. We have shown that the probability distributions of the power spectral density of the Langmuir waves belong to the three main types of Pearson's probability distributions: type I, type IV and type VI.

## 3. RESULTS AND CONCLUSIONS

We have shown that for 36 events – intense locally formed Langmuir waves associated with type III radio bursts – the probability distributions of the power of these waves in the spectral domain belong to the three main types of the Pearson probability distributions: type I, type IV and type VI, Figure 2 (see similar results in Krasnoselskikh et al. 2007 and Musatenko et al. 2007). The goodness of the fits test (e.g.,  $\chi^2$ ) shows that the Pearson probability distributions fit the data better than the log-normal ones for all of the considered events. The performed uncertainty analysis also is in favour of the use of Pearson's system of distributions to model the data.

This result indicates that the Stochastic Growth Theory proposed by Robinson (1992), which assumes log-normal distributions for the wave energy, possibly requires additional verifications and examinations.

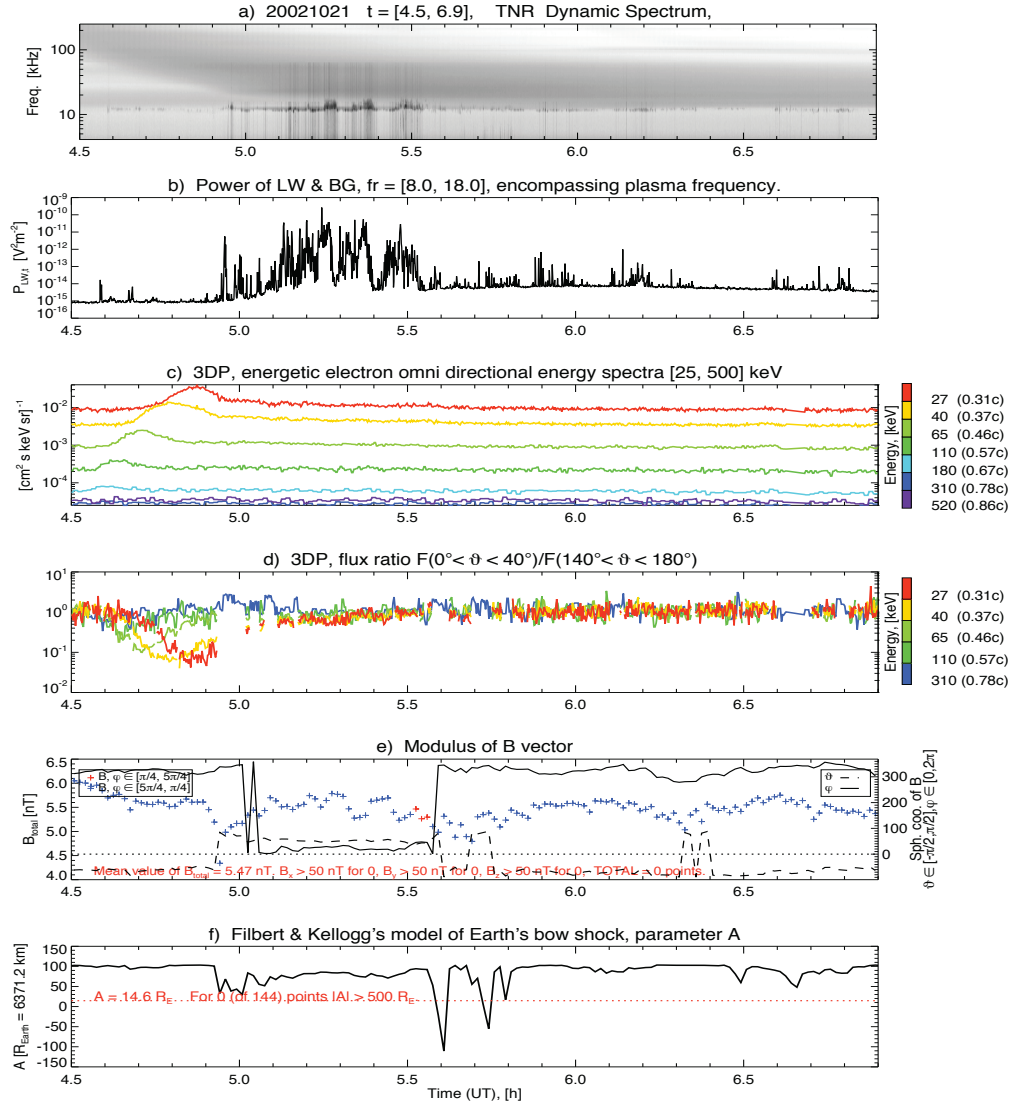


**Fig. 1.** WIND observations on 2002 October 21 (Bougeret et al. 1995): (a) dynamical spectra, only TNR receiver observations (4–256 kHz), (b) power spectral density integrated over narrow frequency band (8–40 kHz) around the plasma frequency ( $\sim 12$  kHz), (c) Omni directional spectrum of energetic electron fluxes, 3DP experiment. The energies are indicated on the right-hand side of the panel (the units on the left-hand side are  $\text{cm}^2$ , s,  $\text{keV}$ ,  $\text{sr}^{-1}$ ), (d) Energetic electron flux ratio  $F(0^\circ < \vartheta < 40^\circ)/F(140^\circ < \vartheta < 180^\circ)$ , (e) magnetic field intensity. Plus (+) symbols indicate the direction of magnetic field vector from the Sun (light gray) or from the Earth (dark gray). Solid and dashed lines indicate two spherical coordinates  $(\vartheta, \varphi)$ , respectively, (f) Parameter A of the Filbert & Kellogg (1979) model of the Earth's bow shock, i.e., the position of the nose-cone of paraboloid along x-axis in the GSE coordinate system. Its tangent (solar magnetic field line) goes through the WIND spacecraft. The dotted line indicates the distance along x-axis, from the Earth to the nose-cone of the Earth's bow shock in steady state. If A is greater than 14.6 Earth's radii, it means that the WIND spacecraft is out of the Earth's bow shock.

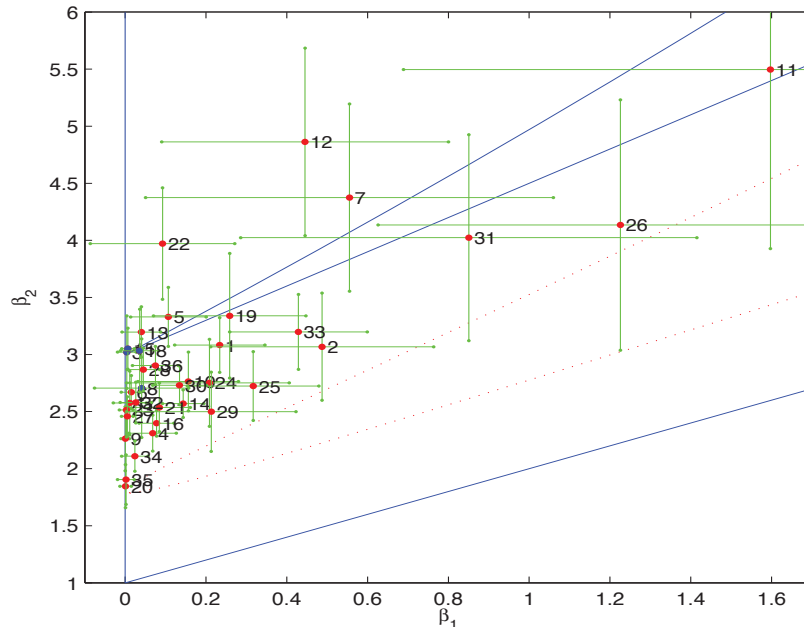


**Fig. 2.** Beta plane. From the 36 events: 28 belong to Pearson's type I, 1 to type VI and 7 to type IV probability distribution. Error bars are calculated by the method of moments. Most of the events are close to normal distribution  $-(\beta_1, \beta_2) = (0, 3)$ , but only for 4 events their error bars intersect the point of normal distribution.

**ACKNOWLEDGMENTS.** This work was supported by a grant from the French government and the French Embassy in Belgrade, and the Serbian Ministry of Education and Science, project 176002. At the Observatoire de Paris, the WIND/WAVES investigation was supported by both CNES and CNRS.

#### REFERENCES

- Bougeret J-L., Kaiser M. L., Kellogg P. J. et al. 1995, *Space Science Rev.*, 71, 231  
 Filbert P. C., Kellogg P. J. 1979, *J. Geoph. Res.*, 84, 1369  
 Krasnoselskikh V. V., Lobzin V. V., Musatenko K. et al. 2007, *J. Geoph. Res.*, 112, A10, 10109  
 Lepping R. P., Acuna M. H., Burlaga L. F. et al. 1995, *Space Science Rev.*, 71, 207  
 Lin R. P., Anderson K. A., Ashford S. et al. 1995, *Space Science Rev.*, 71, 125  
 Maksimović M., Vidojević S., Zaslavsky A. 2011, *Baltic Astronomy*, 20, 600 (this issue)  
 Musatenko K., Lobzin V., Soucek J. et al. 2007, *Plan. & Space Sci.*, 55, 2273  
 Ogilvie K. W., Chornay D. J., Fritzenreiter R. J. et al. 1995, *Space Science Rev.*, 71, 55  
 Pearson K. 1895, *Phil. Trans. R. Soc. London*, 186, 343  
 Robinson P. A. 1992, *Solar Phys.*, 139, 147

## E.3 Maksimovic et al., 2011

Article published 2011 in *Baltic Astronomy*

**Title:** Statistical Analysis of Langmuir Waves Associated with Type III Radio Bursts: II. Simulation and Interpretation of the Wave Energy Distributions

**List of authors:** Maksimović M., Vidojević S., and Zaslavsky A.

**Reference:** Maksimović M., Vidojević S., and Zaslavsky A. Statistical Analysis of Langmuir Waves Associated with Type III Radio Bursts: II. Simulation and Interpretation of the Wave Energy Distributions, *Baltic Astronomy*, **20**, pp. 600-603, (2011)

*Baltic Astronomy, vol. 20, 600–603, 2011*

## STATISTICAL ANALYSIS OF LANGMUIR WAVES ASSOCIATED WITH TYPE III RADIO BURSTS: II. SIMULATION AND INTERPRETATION OF THE WAVE ENERGY DISTRIBUTIONS

M. Maksimović<sup>1</sup>, S. Vidojević<sup>1,2</sup> and A. Zaslavsky<sup>1</sup>

<sup>1</sup> *LESIA – Observatoire de Paris, CNRS, UPMC, Université Paris 06, Université Paris-Diderot, Place Jules Janssen, 92195 Meudon, France; sonja.vidojevic@obspm.fr*

<sup>2</sup> *Faculty of Mathematics, University of Belgrade, Studentski trg 16, 11000 Beograd, Serbia;*

Received: 2011 August 8; accepted: 2011 August 15

**Abstract.** We have modeled electrostatic Langmuir waves by an electric field, consisting of superposition of Gaussian wave packets with several probability distributions of amplitudes and with several Poisson distributions of wave packets. The outcome of the model is that the WIND satellite observations, especially in the low frequency domain (the WAVES experiment), do not allow to conclude whether the input wave amplitude distributions are closer to the log-normal than to the Pearson type I or uniform. The average number of wave packets in 1 s is found to be between 0.1 and 50. Therefore, there is a clear need to measure Langmuir wave energy distributions directly at the waveform level, not a posteriori in the spectral domain. This is planned to be implemented on the RPW (Radio and Plasma Wave Analyzer) instrument in the Solar Orbiter mission.

**Key words:** solar wind – physical processes: plasmas – Langmuir waves

### 1. ELECTRIC FIELD MODEL – SIMULATIONS

We modeled the electric field,  $E(t)$ , detected by the WIND satellite antennas (Bougeret et al. 1995) as a superposition of Gaussian wave packets (Figure 1):

$$E(t) = \sum_{i=1}^N E_i e^{-\frac{1}{2} \left( \frac{t-t_{0i}}{\Delta t_i} \right)^2} \cos(2\pi f_i t + \varphi_i), \quad (1)$$

where  $E_i$  is the amplitude,  $t_{0i}$  is the time where maximum of  $i$ -th wave packet occurs,  $\Delta t_i$  determines the spread of  $t$ -values about  $t_{0i}$ ,  $f_i$  is the frequency and  $\varphi_i$  is the phase of the wave packet. Number of wave packets in 1 s is modeled as a Poisson distribution,  $\mathcal{P}(\lambda)$ . If we consider the number  $N$  to be determined by Poisson law with a flux parameter  $\lambda$  [ $\text{s}^{-1}$ ], the probability to have  $N$  wave packets

within the time  $T_S$  is given by:

$$\mathcal{P}(\lambda) = e^{\lambda T_S} \frac{(\lambda T_S)^N}{N!}, \quad (2)$$

where  $N$  is the number of wave packets observed during the sampling time  $T_S$  of the LFR instrument (Law Frequency Receiver) which measures the voltage power spectral density in  $V^2/\text{Hz}$ , i.e., the Fourier transform of the autocorrelation function of the voltage measured by the dipole antennas.

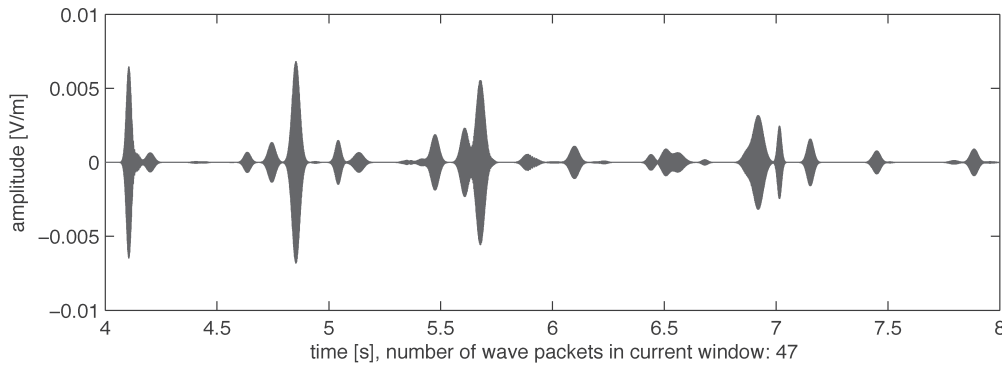


**Fig. 1.** An example of the wave packet simulation with  $\log(A_i^2)$ :  $\mathcal{N}(\mu = -7, \sigma^2 = 1.7^2)$ ;  $\mathcal{P}(\lambda = 10)$ .  $A_i$  is the amplitude of wave packet,  $\mu$  is the first moment – mean value and  $\sigma$  is the second moment – standard deviation of normal probability distribution.

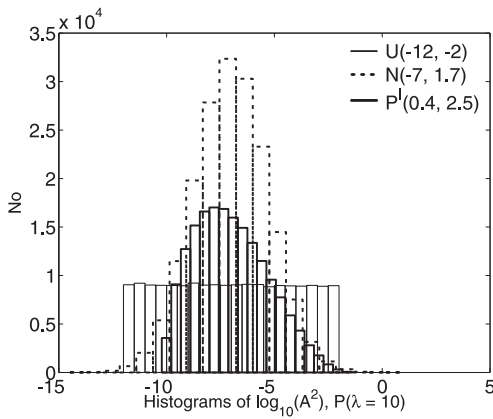


**Fig. 2.** Histograms of input wave packets with amplitudes  $\log(A_i^2)$ : light gray –  $\mathcal{U}(a = -12, b = -2)$ , black –  $\mathcal{N}(\mu = -7, \sigma^2 = 1.7^2)$ , very light gray –  $\mathcal{P}^I(\mu = -0.5, \sigma^2 = 0.5^2, \beta_1 = 0.4, \beta_2 = 2.5)$ ;  $\mathcal{P}(\lambda = 10)$ .

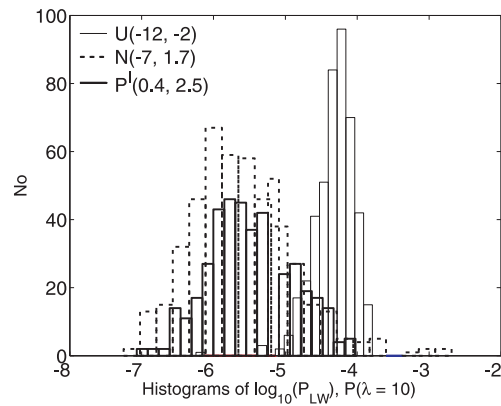


**Fig. 3.** Histograms of the Langmuir wave power,  $\log(P_{LW})$ , spectral domain. They correspond to the input wave packet amplitudes shown in Figure 2.

Histograms of input wave packet power logarithms with three different probability distributions of amplitudes  $\log(A_i^2)$  are shown in Figure 2. Light gray represents histogram with uniform probability distribution,  $\mathcal{U}(a = -12, b = -2)$  where  $a$  and  $b$  are parameters of the probability distribution; black histogram with normal distribution,  $\mathcal{N}(\mu = -7, \sigma^2 = 1.7^2)$ ; and very light gray histogram with Pearson's

type I probability distribution,  $\mathcal{P}^I(\mu = -0.5, \sigma^2 = 0.5^2, \beta_1 = 0.4, \beta_2 = 2.5)$ , where  $\mu$  and  $\sigma$  are the first two parameters, the mean and standard deviations, and  $\beta_1$  and  $\beta_2$  (Eq. 4) are the second two parameters of the distribution. The flux parameter in the Poisson law,  $\mathcal{P}(\lambda)$ , is 10. The corresponding histograms of the Langmuir wave power logarithms,  $\log(P_{LW})$ , in the spectral domain are shown in Figure 3.

## 2. PEARSON'S SYSTEM OF DISTRIBUTIONS – $\beta$ PLANE

Pearson (1895) defined a distribution system by the following equation for the probability density function  $p(x)$ :

$$-\frac{p'(x)}{p(x)} = \frac{b_0 + b_1x}{c_0 + c_1x + c_2x^2}, \quad (3)$$

where  $b_0, b_1, c_0, c_1$  and  $c_2$  are real parameters. The form of the solutions of this differential equation depends on the parameter values, resulting in several distribution types. The classification of distributions in the Pearson system is entirely determined by the two moment ratios, square of skewness,  $\beta_1$ , and kurtosis,  $\beta_2$ :

$$\beta_1 = \frac{\mu_3^2}{\mu_2^3}, \quad \beta_2 = \frac{\mu_4}{\mu_2^2}. \quad (4)$$

We conclude that in the case  $\lambda T_S \gg 1$  it is not possible to recover the initial distribution of the electric field. Whatever is this distribution, at the end we obtain a Gaussian distribution of  $V^2$  (see Figures 2 and 3). The Gaussian parameters are related to the electric field ones ( $E_i$  and  $\Delta t_i$ ) and to the flux at  $\lambda$ . Contrary, in the case  $\lambda T_S \ll 1$ , the distribution of  $V^2$  should be comparable to the distribution of  $\Delta t_i E_i^2$ . In both cases, this does not explain the log-normal distributions predicted by Robinson's Stochastic Growth Theory (SGT) (Robinson 1992), some other process(es) must be responsible.

## 3. RESULTS AND CONCLUSIONS

1. We have shown that for 36 events – intense locally formed Langmuir waves associated with type III radio bursts measured by the WIND spacecraft – the probability distributions of the power logarithm belong to the three types of the Pearson probability distributions: type I, type IV and type VI (Figure 4, black dots). The goodness of the fits test (e.g.,  $\chi^2$ ) shows that the Pearson probability distributions fit the data better than the Gaussian ones for all of the considered events. This is in contradiction with the Stochastic Growth Theory (Robinson 1992) which assumes log-normal distributions for the wave energy, see Vidojević et al. (2012).

2. We have modeled Langmuir waves by the electric field,  $E(t)$ , consisting of Gaussian wave packets with several distributions of amplitudes,  $\log(A^2)$ , and with several Poisson distributions of the number of wave packets in 1 s,  $\mathcal{P}(\lambda)$ .

3. The outcome of these simulations is that the  $\beta_1 - \beta_2$  plane of the WIND observations can be covered by a combination of the following assumptions: (a) from WIND observations it is not possible to conclude whether the input wave

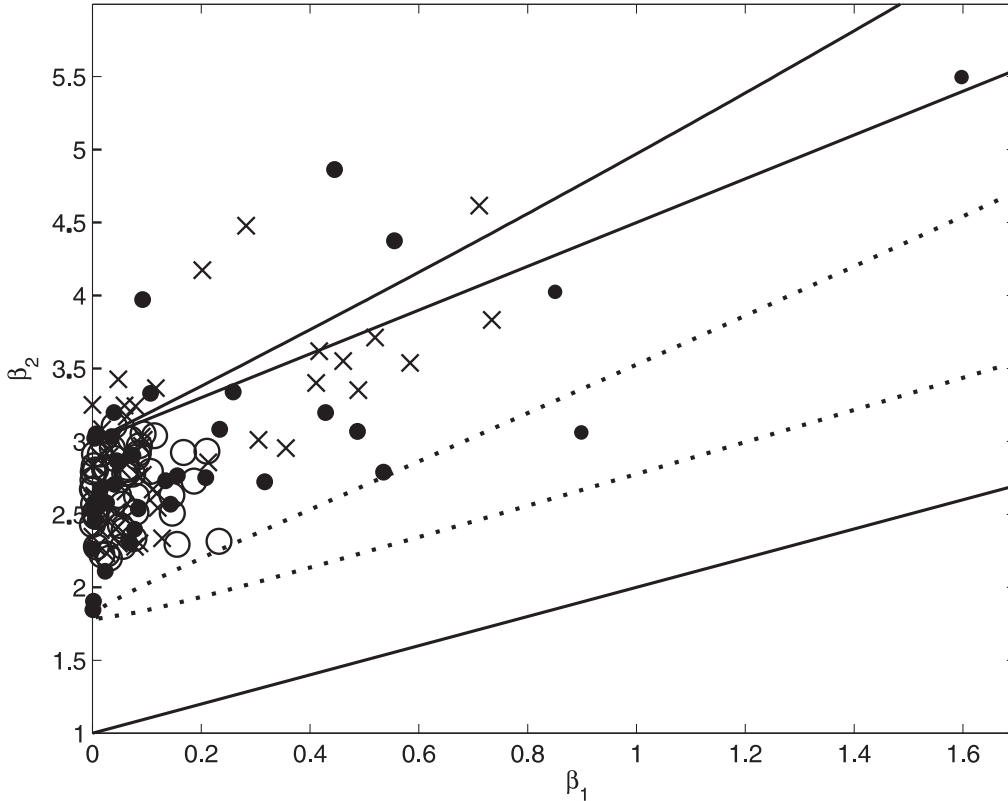


**Fig. 4.** The  $\beta$  plane filled by results of several simulations. Probability distribution of wave packet amplitudes,  $\log(A_i^2)$ :  $\mathcal{P}^I(\mu, \sigma^2, \beta_1, \beta_2)$ . Symbols: circles –  $\mathcal{P}^I(\mu = -7, \sigma^2 = 1.7^2, \beta_1 = 0.4, \beta_2 = 2.5)$ ;  $\times$  –  $\mathcal{P}^I(\mu = -0.5, \sigma^2 = 0.5^2, \beta_1 = 0.4, \beta_2 = 2.5)$ , black dots – 36 WIND events.

amplitude distributions are closer to the log-normal than to the Pearson type I or uniform; (b) the average number of wave packets in 1 s is between 0.1 and 50.

4. Therefore, there is a clear need to measure Langmuir wave energy distributions directly at the waveform level and not *a posteriori* in the spectral domain. This is what is planned to be implemented on the RPW (Radio and Plasma Waves) instrument on the Solar Orbiter, a new space mission.

**ACKNOWLEDGMENTS.** This work was supported by a grant from the French government, the French Embassy in Belgrade and the Ministry of Education and Science of Serbia, project 176002.

#### REFERENCES

- Bougeret J-L. et al. 1995, Sp. Sci. Rev., 71, 231  
 Pearson K. 1895, Phil. Trans. R. Soc. London, 186, 343  
 Robinson P. A. 1992, Solar Phys., 139, 147  
 Vidojević S., Zaslavsky A., Maksimović M., Dražić M., Atanacković O. 2011, Baltic Astronomy, 20, 596 (this issue)

## E.4 Vidojevic and Maksimovic, 2009

Article published 2009 in *Publications de l'Observatoire Astronomique de Beograd*

**Title:** Preliminary Analysis of Type III Radio Bursts from Stereo/Waves Data

**List of authors:** Vidojević S. and Maksimović M.

**Reference:** Vidojević S. and Maksimović M., Preliminary Analysis of Type III Radio Bursts from Stereo/Waves Data, *Publications de l'Observatoire Astronomique de Beograd*, Proceedings of XV National Conference of Astronomers of Serbia – 2008, **86**, pp. 287-291, (2009)

**PRELIMINARY ANALYSIS OF TYPE  
III RADIO BURSTS FROM STEREO/WAVES DATA**

S. VIDOJEVIĆ<sup>1</sup> and M. MAKSIMOVIC<sup>2</sup>

<sup>1</sup>*Department of Astronomy, Faculty of Mathematics,  
Studentstki trg 16, 11000 Beograd, Serbia  
E-mail: sonja@matf.bg.ac.yu*

<sup>2</sup>*LESIA Observatoire de Paris, Section de Meudon,  
5, place Jules Janssen, Meudon Cedex, 92195 France  
E-mail: milan.maksimovic@obspm.fr*

**Abstract.** Solar Type III radio observations in the range 125 kHz – 16 025 kHz from the STEREO/Waves experiment have been preliminary analyzed. These bursts are generated by energetic electrons traveling away from the Sun along open magnetic field lines. A subset of 88 burst has been selected for this study. The dependence of the observed intensity radiation as a function of time at given frequency has been fitted with a Gram-Charlier type A function. The flux density spectra for all the selected type III radio bursts at each frequency channel have been determined. This preliminary analysis gives an empirical expression for the frequency drift rate as a function of frequency for the type III radio bursts.

## 1. INTRODUCTION

Type III bursts arise from impulsively accelerated electrons streaming outward from the Sun on magnetic field lines that are open to the interplanetary medium. The propagating electrons produce a radio emission known as a type III radio burst (Dulk et al. 2000). The frequency, related to the local plasma frequency ( $f_{\text{pl}} \propto \sqrt{n_e}$ ,  $n_e \propto 1/R^2$ ,  $f_{\text{pl}} \propto 1/R$ ), drifts downward as the emission region rapidly propagates outward. Since the radio burst is generated by local plasma emission processes, radio emissions at high frequencies (high plasma densities) occur very near the Sun  $\sim 2R_{\odot}$  for 16 MHz, while those at low frequencies (low plasma densities) occur far from the Sun ( $\sim 1$  AU) for 20 kHz. These type III radio bursts are therefore characterized by a rapid drift to lower frequencies due to the near-relativistic speeds of the burst electrons. The type III radio bursts can be used to infer density and interplanetary magnetic field models in the inner Heliosphere (Leblanc et al. 1998), and to understand better the physics of the radio emissions associated with coronal mass ejections as they propagate from a few solar radii from the photosphere out to 1 AU and beyond.

The terrestrial ionosphere is opaque to radiation at frequencies below some threshold limit depending on the state of the ionosphere. Thus the lower frequency or longer (decametric and kilometric) wavelength interplanetary radio bursts cannot penetrate the ionosphere. If ground-based radio telescopes can access the high-frequency coro-

S. VIDOJEVIĆ and M. MAKSIMOVIC

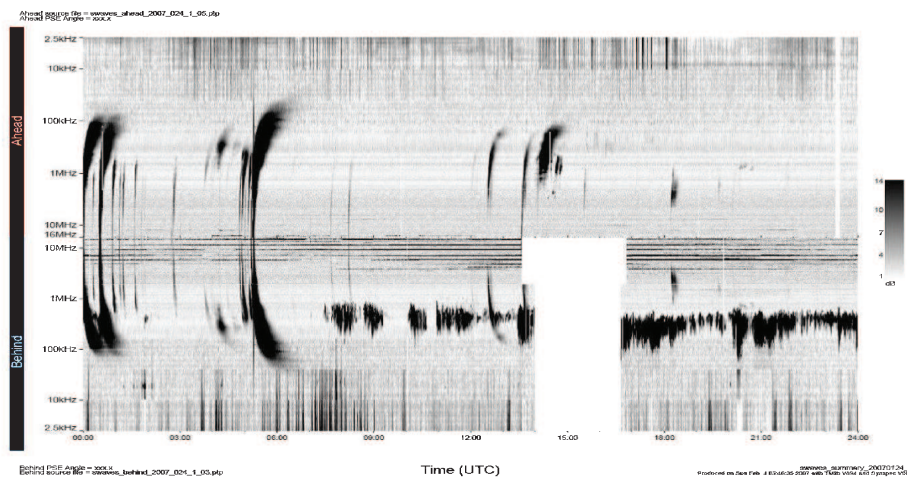


Figure 1: STEREO/Waves dynamic spectrum on January 24, 2007 – several type III radio bursts are observed between 00:00 and 01:00 UTC and at 05:30 UTC.

nal radio emission, the lower frequency interplanetary radio bursts must be detected from space.

## 2. OBSERVATIONS

STEREO (Solar TERrestrial RELations Observatory) (Kaiser 2007) is the third mission in NASA’s Solar Terrestrial Probes program. This mission, launched on October 2006, provides a unique and revolutionary view of the Sun-Earth System. The two nearly identical observatories - one ahead of Earth in its orbit, the other trailing behind - trace the flow of energy and matter from the Sun to Earth. The solar longitudinal separation of the two spacecrafts is increasing during the mission, as well as their respective distance from the Earth along its orbit.

The STEREO/Waves (SWAVES) (Bougeret et al. 2008) experiment is a set of two identical radio receivers placed onboard the two STEREO spacecrafts. Each of them consists of three receivers: the Low Frequency Receiver covering the 2.5–160 kHz range, the High Frequency Receiver covering the 125 kHz–16 MHz range and the Fixed Frequency Receiver providing measurements at 30 or 32 MHz. The sensors are a set of three mutually orthogonal 6 m long electric monopole antennae. Each analysis channel can be connected to one of the three antennae – monopole configuration, or to an electrical combination of two of the three antennae – dipole configuration.

The criteria that were used in the selection of the bursts were the following: (1) the burst should be isolated in time from other bursts, (2) the intensity of burst radiation should be much above background, and (3) the burst should be present in a majority of frequencies. The first criterion ensures that the radio emission is related to a single package of electrons. The second and third criteria restrict the analysis to those bursts which permit accurate measurement of parameters. In this way, a subset of 88 bursts, from November 2006 to the end of September 2007, has been selected (typical type III bursts selected for the analysis are presented in Fig. 1).

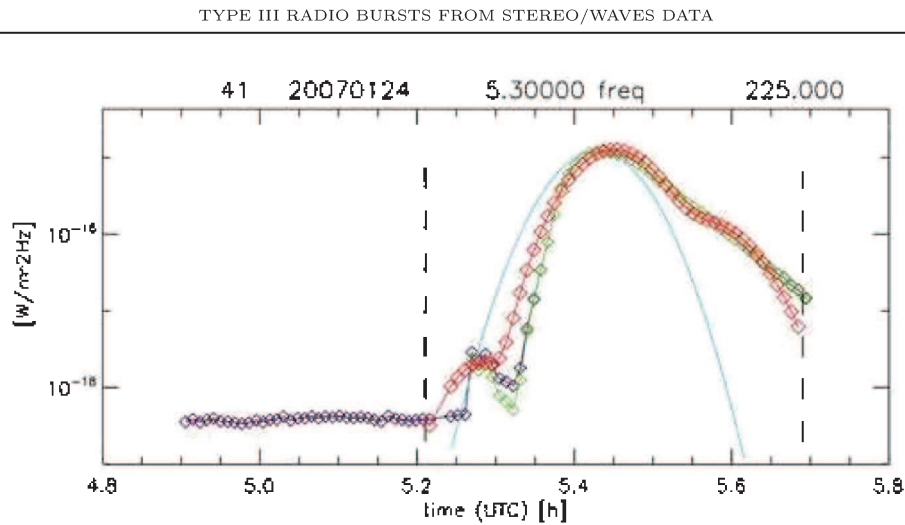


Figure 2: An example of a power spectral density time profile, for an event recorded by STEREO A on January 24, 2007, about 5.30 h UTC at 225 kHz. Violet (black, for the gray scale figure) diamonds display the power spectral density. The green (light gray) diamonds connected with a green (light gray) solid line display the power spectral density after removing the background. The solid blue (light gray) line is the result of a fitting of the latter with a Gaussian function and the red (black) diamonds between the vertical dashed lines display the result of a fitting with a Gram-Charlier type A function. The two vertical dashed lines are the time interval corresponding to plus and minus 5 times the time dispersion of the initial gaussian fit.

### 3. ANALYSIS

The power spectral density at the receiver input is measured in units of  $[V^2\text{Hz}^{-1}]$ . The conversion from power spectral density into incoming flux density in units of  $[\text{Wm}^{-2}\text{Hz}^{-1}]$  is obtained by using the galactic background signal as done by Dulk et al. (2001).

For the subset containing the 88 Type III events we have applied the following analysis procedure. For each of the events and at each of the frequency channels between 125 kHz and 3 MHz, we have examined the profile of the power spectral density as a function of time. Such a profile is displayed in Fig. 2 for an event recorded by Stereo A on January 24, 2007, about 5.30 h UTC at 225 kHz (note that this spectral profile correspond to the part of dynamical spectra showed in Fig. 1). More precisely, we have fitted the time profiles using a Gram-Charlier type A function instead of a Gaussian fit. The description of Gram-Charlier function can be find, for example, in Kendall (1994).

In Fig. 2 we show an example of such a fit. The green (light gray, for the gray scale figure) diamonds connected with a green (light gray) solid line display the power spectral density after removing the background. The solid blue (light gray) line is the result of a fitting of the latter with a Gaussian function and the red (middle gray) diamonds between the vertical dashed lines display the result of a fitting with a Gram-Charlier type A function. The two vertical dashed lines are the time interval

corresponding to plus and minus 5 times the time dispersion of the initial gaussian fit. From Fig 2 it can be clearly seen that the Gram-Charlier function provides a better fit than the Gaussian one. This is confirmed by the comparisons of the Pearson's  $\chi^2$  goodness of fit.

As a next step, we examine the maximum of the power spectral density time profiles for all of the 88 type III bursts and at each of the frequency channels between 125 kHz and 3 MHz. On the average for our subset, the maximum power spectral density occurs at around 0.8 MHz. This result, which still needs to be explained, is in total agreement with the study performed by Bonnin (2008) from an extensive analysis of WIND and ULYSSES radio observations.

As a third step in our analysis we examine the frequency drift rate of type III radio bursts. At higher frequency type III bursts are characterized by a rapid drift rate, while at lower frequency the drift rate is slower. The frequency drift rate is a direct consequence of the mechanisms leading to the emission of type III bursts. As a stream of fast electrons originating from the Sun travels outward thorough the solar corona, it produces radio waves at frequencies equal to the fundamental and to the second harmonic of the local plasma frequency. Since the density of solar plasma decreases with increasing distance from the sun, the type III bursts exhibit negative frequency drift rate. Furthermore, by assuming a constant beam speed it is possible to deduce coronal electron density models as a function of distance (Leblanc et al. 1998). On the other hand assuming a given density model, it is possible to deduce the beam speed (Alvarez and Haddock 1973, Bonnin 2008).

For our 88 bursts subset we have computed the frequency drift rates obtained from all the maxima of the power spectral density profiles at each of the covered frequencies. In our analysis we use dimensionless form of all quantities with scale factors: 1 MHz for frequency, 1 AU for distance, 1 s for time and  $1 \text{ ms}^{-1}$  for velocity. The general linear equation for the frequency drift rate in log-log scale is:

$$\log \left| \frac{df}{dt} \right| = \log b + \alpha \log f, \quad (1)$$

or, with  $\log b = a$ ,

$$\frac{df}{dt} = -10^a f^\alpha. \quad (2)$$

The negative sign denotes that the starting frequency is observed to drift from high to low values. The least square fit of a straight line through all of our observed maxima gives:

$$\alpha = 1.80 \pm 0.05 \quad \text{and} \quad a = -1.70 \pm 0.03. \quad (3)$$

This result is in good agreement with result obtained by Alvarez & Haddock (1973).

In the fourth step of our analysis, we assume a given density model for the solar wind and retrieve the electron beam speed  $V(R)$  as a function of the heliocentric distance  $R$ . Actually, using the result of our fitting, the frequency drift can be written as:

$$-0.02 f^{1.80 \pm 0.05} = \frac{\partial f}{\partial R} \frac{dR}{dt} = \frac{\partial f}{\partial R} V(R). \quad (4)$$

Assuming a simple  $1/R^2$  density variation for the solar wind, that is a  $1/R$  variation for the plasma frequency (i.e.  $f = k \frac{1}{R}$  where  $k$  is numerically equal to plasma frequency

in MHz at a distance of 1 astronomical unit), this implies:

$$V(R) = KR^{0.2 \pm 0.05}, \quad (5)$$

where  $K = 0.02 \text{ k}^{0.80}$ .

This result, which is also in very good agreement with Bonnin (2008), shows that the electron beam speed dependence with distance from the Sun is very weak. The beam speed is almost constant.

#### 4. CONCLUSION

- (i) The fitting of the power spectral density time profiles using Gram-Charlier type A functions gives better results than the fitting with Gaussian (normal) distribution.
- (ii) The global maximum of the power spectral density distributions occurs at approximately 0.8 MHz. This result still needs to be explained.
- (iii) Our preliminary analysis gives an empirical expression for the frequency drift rate as a function of frequency for the type III radio bursts:  $\frac{df}{dt} = -0.02 f^{1.80}$  in units  $[\text{MHz s}^{-1}]$ .
- (iv) From the frequency drift rate, we have deduced that the electron beam speed,  $V(R)$ , is a weak function of the heliocentric distance.

#### References

- Alvarez, H., Haddock, F. T.: 1973, *Solar Physics*, **29**, 197.
- Bonnin, X.: 2008, Etude stéréoscopique de la directivité des sursauts radio solaires de type III aux fréquences inférieures à 10 MHz, Thèse de Doctorat, Université Paris, Diderot - Paris VII.
- Bougeret J.-L. et al.: 2008, *Space Sci. Rev.*, **136**, 487.
- Dulk, G. A.: 2000, Type III Solar Radio Bursts at Long Wavelengths, in: Stone, R. G., Weiler, K. W., Goldstein, M. L., Bougeret, J.-L., eds, *Radio Astronomy at Long Wavelength*, 115.
- Dulk, G. A., Erickson, W. C., Manning, R., Bougeret, J.-L.: 2001, *Astron. Astrophys.*, **365**, 294.
- Kaiser M. L.: 2005, *Adv. Space Res.*, **36**, 1483.
- Kaiser M. L. et al.: 2007, *Space Science Reviews*, **136**, iss. 1-4, 5.
- Kendall, G. M.: 1994, *Kendall's advanced theory of statistics*, Edward Arnold, Halsted Press, London, New York.
- Leblanc, Y., Dulk, G. A., Bougeret, J.-L.: 1998, *Sol. Phys.*, **183**, 165.



# Bibliography

- Aitchison, J. and Brown, J. (1957). *The Lognormal Distribution*. Univ. of Cambridge, Dep. of Applied Economics. Monographs. University Press.  
**Referenced on page:** 21.
- Aschwanden, M. J., Benz, A. O., and Schwartz, R. A. (1993). The Timing of Electron Beam Signatures in Hard X-Ray and Radio: Solar Flare Observations by BATSE/Compton Gamma-Ray Observatory and PHOENIX. *Astrophysical Journal*, **417**, 790.  
**Referenced on page:** 16.
- Bale, S. D. (2011). personal communication.  
**Referenced on page:** 27 and 62.
- Bale, S. D., Burgess, D., Kellogg, P. J., Goetz, K., and Monson, S. J. (1997). On the amplitude of intense Langmuir Waves in the terrestrial electron foreshock. *Journal of Geophysical Research*, **102**, 11281–11286.  
**Referenced on page:** 38, 49 and 65.
- Bale, S. D., Kellogg, P. J., Goetz, K., and Monson, S. J. (1998). Transverse z-mode waves in the terrestrial electron foreshock. *Geophysical Research Letters*, **25**, 9–12.  
**Referenced on page:** 11.
- Bernstein, I. B. (1958). Waves in a plasma in a magnetic field. *Phys. Rev.*, **109**, 10–21.  
**Referenced on page:** 70.
- Biermann, L. (1951). Kometenschweife und solare Korpuskularstrahlung. *Zeitschrift fur Astrophysik*, **29**, 274.  
**Referenced on page:** 1 and 7.
- Boehm, M. H., Carlson, C. W., McFadden, J. P., Clemmons, J. H., Ergun, R. E., and Mozer, F. S. (1994). Wave rectification in plasma sheaths surrounding electric field antennas. *Journal of Geophysical Research*, **99**, 21361.  
**Referenced on page:** 11.
- Bougeret, J., Kaiser, M. L., Kellogg, P. J., Manning, R., Goetz, K., Monson, S. J., Monge, N., Friel, L., Meetre, C. A., Perche, C., Sitruk, L., and Hoang, S. (1995). Waves: The Radio and Plasma Wave Investigation on the Wind Spacecraft. *Space Science Reviews*, **71**, 231–263.  
**Referenced on page:** 25 and 42.
- Bougeret, J. L., Goetz, K., Kaiser, M. L., Bale, S. D., Kellogg, P. J., Maksimovic, M., Monge, N., Monson, S. J., Astier, P. L., Davy, S., Dekkali, M., Hinze, J. J., Manning, R. E., Aguilar-Rodriguez, E., Bonnin, X., Briand, C., Cairns, I. H., Cattell, C. A., Cecconi, B., Eastwood, J., Ergun, R. E., Fainberg, J., Hoang, S., Huttunen, K. E. J., Krucker, S., Lecacheux, A., MacDowall, R. J., Macher, W., Mangeney, A., Meetre, C. A., Moussas, X., Nguyen, Q. N., Oswald, T. H., Pulupa, M., Reiner, M. J., Robinson, P. A., Rucker, H., Salem, C., Santolik, O., Silvis, J. M., Ullrich, R., Zarka, P., and Zouganelis, I. (2008). S/WAVES: The Radio and Plasma Wave Investigation on the STEREO Mission. *Space Science Reviews*, **136**, 487–528.  
**Referenced on page:** 38 and 41.
- Cairns, I. H. and Melrose, D. B. (1985). A theory for the 2f(p) radiation upstream of the earth's bow shock. *Journal of Geophysical Research*, **90**, 6637–6640.  
**Referenced on page:** 11 and 62.
- Cairns, I. H. and Robinson, P. A. (1999). Strong Evidence for Stochastic Growth of Langmuir-like Waves in Earth's Foreshock. *Physical Review Letters*, **82**, 3066–3069.  
**Referenced on page:** 38.

- Cairns, I. H., Johnston, S., and Das, P. (2001). Intrinsic Variability of the Vela Pulsar: Lognormal Statistics and Theoretical Implications. *The Astrophysical Journal Letters*, **563**, L65–L68.  
**Referenced on page: 2.**
- Cane, H. V. and Reames, D. V. (1988). Soft X-ray emissions, meter-wavelength radio bursts, and particle acceleration in solar flares. *Astrophysical Journal*, **325**, 895–900.  
**Referenced on page: 16 and 17.**
- Cane, H. V., Erickson, W. C., and Prestage, N. P. (2002). Solar flares, type III radio bursts, coronal mass ejections, and energetic particles. *Journal of Geophysical Research (Space Physics)*, **107**, 1315.  
**Referenced on page: 17.**
- Carrington, R. C. (1859). Description of a Singular Appearance seen in the Sun on September 1, 1859. *Monthly Notices of the Royal Astronomical Society*, **20**, 13–15.  
**Referenced on page: 6.**
- Cranmer, S. R. (2002). Coronal Holes and the High-Speed Solar Wind. *Space Science Reviews*, **101**, 229–294.  
**Referenced on page: 8.**
- Dawson, J. (1961). On Landau Damping. *Physics of Fluids*, **4**, 869–874.  
**Referenced on page: 18.**
- Dulk, G. A., Leblanc, Y., Bastian, T. S., and Bougeret, J.-L. (2000). Acceleration of electrons at type II shock fronts and production of shock-accelerated type III bursts. *Journal of Geophysical Research*, **105**, 27343–27352.  
**Referenced on page: 17.**
- Ergun, R. E., Larson, D., Lin, R. P., McFadden, J. P., Carlson, C. W., Anderson, K. A., Muschietti, L., McCarthy, M., Parks, G. K., Reme, H., Bosqued, J. M., D’Uston, C., Sanderson, T. R., Wenzel, K. P., Kaiser, M., Lepping, R. P., Bale, S. D., Kellogg, P., and Bougeret, J. (1998). Wind Spacecraft Observations of Solar Impulsive Electron Events Associated with Solar Type III Radio Bursts. *Astrophysical Journal*, **503**, 435–+.  
**Referenced on page: 54 and 65.**
- Feldman, U., Landi, E., and Schwadron, N. A. (2005). On the sources of fast and slow solar wind. *Journal of Geophysical Research (Space Physics)*, **110**(A9), 7109.  
**Referenced on page: 7.**
- Filbert, P. C. and Kellogg, P. J. (1979). Electrostatic noise at the plasma frequency beyond the earth’s bow shock. *Journal of Geophysical Research*, **84**, 1369–1381.  
**Referenced on page: 27.**
- Frank, L. A. and Gurnett, D. A. (1972). Direct Observations of Low-Energy Solar Electrons Associated with a Type III Solar Radio Burst. *Solar Physics*, **27**, 446–465.  
**Referenced on page: 53.**
- Ginzburg, V. L. and Zhelezniakov, V. V. (1958a). On the Possible Mechanisms of Sporadic Solar Radio Emission (Radiation in an Isotropic Plasma). *Soviet Astronomy*, **2**, 653–+.  
**Referenced on page: iii, v, vii, 3 and 10.**
- Ginzburg, V. L. and Zhelezniakov, V. V. (1958b). On the Possible Mechanisms of Sporadic Solar Radio Emission (Radiation in an Isotropic Plasma). *Astronomicheskii Zhurnal*, **35**, 694–705.  
**Referenced on page: 53.**
- Goldman, M. V., Reiter, G. F., and Nicholson, D. R. (1980). Radiation from a strongly turbulent plasma - Application to electron beam-excited solar emissions. *Physics of Fluids*, **23**, 388–401.  
**Referenced on page: 12.**

- Gosling, J. T., Skoug, R. M., and McComas, D. J. (2003). Solar electron bursts at very low energies: Evidence for acceleration in the high corona? *Geophysical Research Letters*, **30**(13), 130000–1.  
**Referenced on page:** 54.
- Gringauz, K. I., Bezrokh, V. V., Ozerov, V. D., and Rybchinskii, R. E. (1960). A Study of the Interplanetary Ionized Gas, High-Energy Electrons and Corpuscular Radiation from the Sun by Means of the Three-Electrode Trap for Charged Particles on the Second Soviet Cosmic Rocket. *Soviet Physics Doklady*, **5**, 361.  
**Referenced on page:** 1 and 7.
- Gurnett, D. A. and Anderson, R. R. (1976). Electron plasma oscillations associated with type III radio bursts. *Science*, **194**, 1159–1162.  
**Referenced on page:** 53.
- Gurnett, D. A. and Anderson, R. R. (1977). Plasma wave electric fields in the solar wind - Initial results from HELIOS 1. *Journal of Geophysical Research*, **82**, 632–650.  
**Referenced on page:** 53.
- Gurnett, D. A. and Bhattacharjee, A. (2005). *Introduction to Plasma Physics: With Space and Laboratory Applications*. Cambridge University Press.  
**Referenced on page:** 1.
- Gurnett, D. A. and Frank, L. A. (1975). Electron plasma oscillations associated with type III radio emissions and solar electrons. *Solar Physics*, **45**, 477–493.  
**Referenced on page:** 62.
- Harten, R. and Clark, K. (1995). The Design Features of the GGS Wind and Polar Spacecraft. *Space Science Reviews*, **71**, 23–40.  
**Referenced on page:** 25.
- Henon, M. (1982). Vlasov equation. *Astronomy and Astrophysics*, **114**, 211.  
**Referenced on page:** 70.
- Henri, P., Briand, C., Mangeney, A., Bale, S. D., Califano, F., Goetz, K., and Kaiser, M. (2009). Evidence for wave coupling in type III emissions. *Journal of Geophysical Research (Space Physics)*, **114**, 3103.  
**Referenced on page:** 62.
- Hodgson, R. (1859). On a curious Appearance seen in the Sun. *Monthly Notices of the Royal Astronomical Society*, **20**, 15–16.  
**Referenced on page:** 6.
- Hollweg, J. V. (2008). The solar wind: Our current understanding and how we got here. *Journal of Astrophysics and Astronomy*, **29**, 217–237.  
**Referenced on page:** 8.
- Hospodarsky, G. B. and Gurnett, D. A. (1995). Beat-type Langmuir wave emissions associated with a type III solar radio burst: Evidence of parametric decay. *Geophysical Research Letters*, **22**, 1161–1164.  
**Referenced on page:** 11.
- Johnson, N., Kotz, S., and Balakrishnan, N. (1994). *Continuous Univariate Distributions*, volume 1,2 of *Wiley Series in Probability and Mathematical Statistics*. Wiley, New York.  
**Referenced on page:** 35.
- Kasaba, Y., Matsumoto, H., Omura, Y., Anderson, R. R., Mukai, T., Saito, Y., Yamamoto, T., and Kokubun, S. (2000). Statistical studies of plasma waves and backstreaming electrons in the terrestrial electron foreshock observed by Geotail. *Journal of Geophysical Research*, **105**, 79–104.  
**Referenced on page:** 62.

- Kellogg, P. J., Goetz, K., Lin, N., Monson, S. J., Balogh, A., Forsyth, R. J., and Stone, R. G. (1992). Low frequency magnetic signals associated with Langmuir waves. *Geophysical Research Letters*, **19**, 1299–1302.  
**Referenced on page:** 11.
- Kim, E.-H., Cairns, I. H., and Robinson, P. A. (2008). Mode conversion of Langmuir to electromagnetic waves at magnetic field-aligned density inhomogeneities: Simulations, theory, and applications to the solar wind and the corona. *Physics of Plasmas*, **15**(10), 102110.  
**Referenced on page:** 11.
- Kontar, E. P. (2001). Dynamics of electron beams in the solar corona plasma with density fluctuations. *Astronomy and Astrophysics*, **375**, 629–637.  
**Referenced on page:** 54 and 62.
- Kontar, E. P., Lapshin, V. I., and Melnik, V. N. (1998). Numerical and analytical study of the propagation of a monoenergetic electron beam in a plasma. *Plasma Physics Reports*, **24**, 772–776.  
**Referenced on page:** 54.
- Krasnoselskikh, V. V., Lobzin, V. V., Musatenko, K., Soucek, J., Pickett, J. S., and Cairns, I. H. (2007). Beam-plasma interaction in randomly inhomogeneous plasmas and statistical properties of small-amplitude Langmuir waves in the solar wind and electron foreshock. *Journal of Geophysical Research (Space Physics)*, **112**(11), 10109–+.  
**Referenced on page:** 23 and 54.
- Krucker, S. (2012). personal communication.  
**Referenced on page:** 59.
- Krucker, S., Kontar, E. P., Christe, S., and Lin, R. P. (2007). Solar Flare Electron Spectra at the Sun and near the Earth. *The Astrophysical Journal Letters*, **663**, L109–L112.  
**Referenced on page:** 54.
- Krucker, S., Oakley, P. H., and Lin, R. P. (2009). Spectra of Solar Impulsive Electron Events Observed Near Earth. *The Astrophysical Journal Letters*, **691**, 806–810.  
**Referenced on page:** 58 and 66.
- Landau, L. (1946). On the vibrations of the electronic plasma. *J. Phys. USSR*, **10**(25), 574.  
**Referenced on page:** 3, 18, 54, 70 and 70.
- Lang, K. (2001). *The Cambridge Encyclopedia of the Sun*. Cambridge University Press.  
**Referenced on page:** 13.
- Lepping, R. P., Acuña, M. H., Burlaga, L. F., Farrell, W. M., Slavin, J. A., Schatten, K. H., Mariani, F., Ness, N. F., Neubauer, F. M., Whang, Y. C., Byrnes, J. B., Kennon, R. S., Panetta, P. V., Scheifele, J., and Worley, E. M. (1995). The Wind Magnetic Field Investigation. *Space Science Reviews*, **71**, 207–229.  
**Referenced on page:** 25 and 54.
- Li, B., Robinson, P. A., and Cairns, I. H. (2006). Numerical Simulations of Type-III Solar Radio Bursts. *Physical Review Letters*, vol. 96, Issue 14, id. 145005, **96**(14), 145005.  
**Referenced on page:** 54.
- Lin, R. P. (1970). The Emission and Propagation of 40 keV Solar Flare Electrons. I: The Relationship of 40 keV Electron to Energetic Proton and Relativistic Electron Emission by the Sun. *Solar Physics*, **12**, 266–303.  
**Referenced on page:** 53.
- Lin, R. P. (1974). Non-relativistic Solar Electrons. *Space Science Reviews*, **16**, 189–256.  
**Referenced on page:** 53.

- Lin, R. P. (1985). Energetic solar electrons in the interplanetary medium. *Solar Physics*, **100**, 537–561.  
**Referenced on page: 53.**
- Lin, R. P., Evans, L. G., and Fainberg, J. (1973). Simultaneous Observations of Fast Solar Electrons and Type III Radio Burst Emission Near 1 AU. *Astrophysical Letters*, **14**, 191.  
**Referenced on page: 53 and 65.**
- Lin, R. P., Potter, D. W., Gurnett, D. A., and Scarf, F. L. (1981). Energetic electrons and plasma waves associated with a solar type III radio burst. *Astrophysical Journal*, **251**, 364–373.  
**Referenced on page: 54.**
- Lin, R. P., Mewaldt, R. A., and Van Hollebeke, M. A. I. (1982). The energy spectrum of 20 keV–20 MeV electrons accelerated in large solar flares. *Astrophysical Journal*, **253**, 949–962.  
**Referenced on page: 58 and 66.**
- Lin, R. P., Levedahl, W. K., Lotko, W., Gurnett, D. A., and Scarf, F. L. (1986). Evidence for nonlinear wave-wave interactions in solar type III radio bursts. *Astrophysical Journal*, **308**, 954–965.  
**Referenced on page: 11.**
- Lin, R. P., Anderson, K. A., Ashford, S., Carlson, C., Curtis, D., Ergun, R., Larson, D., McFadden, J., McCarthy, M., Parks, G. K., Rème, H., Bosqued, J. M., Coutelier, J., Cotin, F., D’Uston, C., Wenzel, K., Sanderson, T. R., Henrion, J., Ronnet, J. C., and Paschmann, G. (1995). A Three-Dimensional Plasma and Energetic Particle Investigation for the Wind Spacecraft. *Space Science Reviews*, **71**, 125–153.  
**Referenced on page: 26 and 54.**
- Lin, R. P., Larson, D., McFadden, J., Carlson, C. W., Ergun, R. E., Anderson, K. A., Ashford, S., McCarthy, M., Parks, G. K., Rème, H., Bosqued, J. M., d’Uston, C., Sanderson, T. R., and Wenzel, K. P. (1996). Observation of an impulsive solar electron event extending down to ~0.5 keV energy. *Geophysical Research Letters*, **23**, 1211–1214.  
**Referenced on page: 58.**
- Magelssen, G. R. and Smith, D. F. (1977). Nonrelativistic electron stream propagation in the solar atmosphere and type III radio bursts. *Solar Physics*, **55**, 211–240.  
**Referenced on page: 54.**
- Malaspina, D. M., Ergun, R. E., and Cairns, I. H. (2009). Plasma Emission at Shocks by the Eigenmode-Antenna Mechanism. In X. Ao and G. Z. R. Burrows, editors, *American Institute of Physics Conference Series*, volume 1183 of *American Institute of Physics Conference Series*, pages 131–138.  
**Referenced on page: 12.**
- Malmberg, J. H. and Wharton, C. B. (1966). Dispersion of electron plasma waves. *Phys. Rev. Lett.*, **17**, 175–178.  
**Referenced on page: 18.**
- McLean, D. J. and Labrum, N. R. (1985). *Solar radiophysics: Studies of emission from the sun at metre wavelengths*. Cambridge University Press.  
**Referenced on page: 53.**
- Melnik, V. N. (1995). “Gas-dynamic” expansion of a fast-electron flux in a plasma. *Plasma Physics Reports*, **21**, 89–91.  
**Referenced on page: 54.**
- Mel’nik, V. N. and Kontar, E. P. (2000). To gasdynamic description of a hot electron cloud in a cold plasma. *New Astronomy*, **5**, 35–42.  
**Referenced on page: 62.**

- Melrose, D. B. (1985). Plasma emission mechanisms. In D. J. McLean and N. R. Labrum, editors, *Solar Radiophysics: Studies of Emission from the Sun at Metre Wavelengths*, pages 177–210. Cambridge University Press.  
**Referenced on page:** 10.
- Melrose, D. B. (1990). Particle beams in the solar atmosphere - General overview. *Solar Physics*, **130**, 3–18.  
**Referenced on page:** 28.
- Meyer-Vernet, N. and Perche, C. (1989). Tool kit for antennae and thermal noise near the plasma frequency. *Journal of Geophysical Research*, **94**, 2405–2415.  
**Referenced on page:** 26.
- Musatenko, K., Lobzin, V., Soucek, J., Krasnoselskikh, V. V., and Décréau, P. (2007). Statistical properties of small-amplitude Langmuir waves in the Earth's electron foreshock. *Planetary Space Science*, **55**, 2273–2280.  
**Referenced on page:** 23.
- Muschietti, L. (1990). Electron beam formation and stability. *Solar Physics*, **130**, 201–228.  
**Referenced on page:** 28.
- Nagahara, Y. (2004). A method of simulating multivariate nonnormal distributions by the Pearson distribution system and estimation. *Computational Statistics & Data Analysis*, **47**, 1–29.  
**Referenced on page:** 35 and 36.
- Neugebauer, M. and Snyder, C. W. (1962). Solar Plasma Experiment. *Science*, **138**, 1095–1097.  
**Referenced on page:** 1 and 7.
- Neugebauer, M. and Snyder, C. W. (1966). Mariner 2 Observations of the Solar Wind, 1, Average Properties. *Journal of Geophysical Research*, **71**, 4469.  
**Referenced on page:** 7.
- Ogilvie, K. W., Chornay, D. J., Fritzenreiter, R. J., Hunsaker, F., Keller, J., Lobell, J., Miller, G., Scudder, J. D., Sittler, Jr., E. C., Torbert, R. B., Bodet, D., Needell, G., Lazarus, A. J., Steinberg, J. T., Tappan, J. H., Mavretic, A., and Gergin, E. (1995). SWE, A Comprehensive Plasma Instrument for the Wind Spacecraft. *Space Science Reviews*, **71**, 55–77.  
**Referenced on page:** 26 and 54.
- Papadopoulos, K. and Freund, H. P. (1978). Solitons and second harmonic radiation in type III bursts. *Geophysical Research Letters*, **5**, 881–884.  
**Referenced on page:** 12.
- Parker, E. N. (1958). Suprathermal Particle Generation in the Solar Corona. *Astrophysical Journal*, **128**, 677.  
**Referenced on page:** 1, 5 and 7.
- Parker, E. N. (2001). A history of early work on the heliospheric magnetic field. *Journal of Geophysical Research*, **106**, 15797–15802.  
**Referenced on page:** 7.
- Pearson, K. (1895). Contributions to the Mathematical Theory of Evolution. II. Skew Variation in Homogeneous Material. *Philosophical Transactions of the Royal Society of London*, **186**, 343–414.  
**Referenced on page:** 23, 33, 34, 34, 36 and 73.
- Pearson, K. (1902). On the Mathematical Theory of Errors of Judgment, with Special Reference to the Personal Equation. *Royal Society of London Philosophical Transactions Series A*, **198**, 235–299.  
**Referenced on page:** 74.

- Pottelette, R., Treumann, R. A., and Dubouloz, N. (1992). Generation of auroral kilometric radiation in upper hybrid wave-lower hybrid soliton interaction. *Journal of Geophysical Research*, **97**, 12029.  
**Referenced on page:** 12.
- Press, W. H., Teukolsky, S. A., Vetterling, W. T., and Flannery, B. P. (2007). *Numerical Recipes 3rd Edition: The Art of Scientific Computing*. Cambridge University Press, New York, NY, USA.  
**Referenced on page:** 36.
- Reames, D. V. (1999). Particle acceleration at the Sun and in the heliosphere. *Space Science Reviews*, **90**, 413–491.  
**Referenced on page:** 17.
- Reid, H. A. S. and Kontar, E. P. (2010). Solar Wind Density Turbulence and Solar Flare Electron Transport from the Sun to the Earth. *Astrophysical Journal*, **721**, 864–874.  
**Referenced on page:** 54, 58, 59 and 66.
- Reid, H. A. S. and Kontar, E. P. (2012). Evolution of the Solar Flare Energetic Electrons in the Inhomogeneous Inner Heliosphere. *Solar Physics*, page 109.  
**Referenced on page:** 54, 58, 59 and 66.
- Richaume, P. (1996). *Approche connexionniste pour le pilotage temps réel du récepteur numérique Waves/TNR embarqué sur la sonde spatiale Wind*. Ph.D. thesis, Conservatoire National des Arts et Métiers, Paris, France.  
**Referenced on page:** 27.
- Robinson, P. A. (1992). Clumpy Langmuir waves in type III radio sources. *Solar Physics*, **139**, 147–163.  
**Referenced on page:** iii, v, vii, 22, 23, 28 and 32.
- Robinson, P. A. (1993). Stochastic-growth theory of Langmuir growth-rate fluctuations in type III solar radio sources. *Solar Physics*, **146**, 357–363.  
**Referenced on page:** 22 and 23.
- Robinson, P. A., Cairns, I. H., and Gurnett, D. A. (1993). Clumpy Langmuir waves in type III radio sources - Comparison of stochastic-growth theory with observations. *Astrophysical Journal*, **407**, 790–800.  
**Referenced on page:** 22, 23, 33 and 38.
- Sitruk, L. and Manning, R. (1995). *L'expérience spatiale G.G.S./WIND/WAVES, Ondes radioélectriques et ondes de plasma, Le récepteur TNR*. LESIA, l'Observatoire de Paris.  
**Referenced on page:** 42 and 42.
- Stix, T. H. (1962). *The theory of plasma waves*. McGraw-Hill Book Co., Inc., New York.  
**Referenced on page:** 22 and 22.
- Takakura, T. and Shibahashi, H. (1976). Dynamics of a cloud of fast electrons travelling through the plasma. *Solar Physics*, **46**, 323–346.  
**Referenced on page:** 54.
- Thejappa, G., MacDowall, R. J., Scime, E. E., and Littleton, J. E. (2003). Evidence for electrostatic decay in the solar wind at 5.2 AU. *Journal of Geophysical Research (Space Physics)*, **108**, 1139.  
**Referenced on page:** 11.
- Vlasov, A. A. (1938). O vibratsionnykh svoistvakh elektronnogo gaza. *Zhurnal eksperimental'noi i teoreticheskoi fiziki*, **8**(3), 291–318.  
**Referenced on page:** 69.

- Vlasov, A. A. (1967). O vibratsionnykh svoistvakh elektronogo gaza. *Uspekhi Fizicheskikh Nauk*, **93**(11), 444–470.  
**Referenced on page: 70.**
- Wild, J. P., Smerd, S. F., and Weiss, A. A. (1963). Solar Bursts. *Annual Review of Astronomy & Astrophysics*, **1**, 291.  
**Referenced on page: 13.**
- Willes, A. J. and Cairns, I. H. (2000). Generalized Langmuir waves in magnetized kinetic plasmas. *Physics of Plasmas*, **7**, 3167–3180.  
**Referenced on page: 11.**
- Wu, S. T., de Jager, C., Dennis, B. R., Hudson, H. S., Simnett, G. M., Strong, K. T., Bentley, R. D., Bornmann, P. L., Bruner, M. E., Cargill, P. J., Crannell, C. J., Doyle, J. G., Hyder, C. L., Kopp, R. A., Lemen, J. R., Martin, S. F., Pallavicini, R., Peres, G., Serio, S., Sylwester, J., and Veck, N. J. (1989). Flare energetics. In M. R. Kundu and B. Woodgate, editors, *Energetic Phenomena on the Sun*, pages 377–492.  
**Referenced on page: 17.**
- Yin, L., Ashour-Abdalla, M., El-Alaoui, M., Bosqued, J. M., and Bougeret, J. L. (1998). Generation of electromagnetic  $f_{pe}$  and  $2f_{pe}$  waves in the Earth's electron foreshock via linear mode conversion. *Geophysical Research Letters*, **25**, 2609–2612.  
**Referenced on page: 11.**
- Yoon, P. H., Wu, C. S., Vinas, A. F., Reiner, M. J., Fainberg, J., and Stone, R. G. (1994). Theory of  $2\omega_{pe}$  radiation induced by the bow shock. *Journal of Geophysical Research*, **99**, 23481.  
**Referenced on page: 12.**
- Yoon, P. H., Ziebell, L. F., and Wu, C. S. (2000). Excitation of Langmuir waves in interplanetary space. *Journal of Geophysical Research*, **105**, 27369–27376.  
**Referenced on page: 54.**
- Zaitsev, V. V., Mityakov, N. A., and Rapoport, V. O. (1972). A Dynamic Theory of Type III Solar Radio Bursts. *Solar Physics*, **24**, 444–456.  
**Referenced on page: 3 and 54.**
- Zakharov, V. E. (1972). Collapse of Langmuir Waves. *Zhurnal Eksperimental'noi i Teoreticheskoi Fiziki (Journal of Experimental and Theoretical Physics, eng.)*, **35**, 908.  
**Referenced on page: 12.**
- Zaslavsky, A. (2012). personal communication.  
**Referenced on page: 41.**
- Zaslavsky, A., Volokitin, A. S., Krasnoselskikh, V. V., Maksimovic, M., and Bale, S. (2010). Spatial localization of Langmuir waves generated from an electron beam propagating in an inhomogeneous plasma: Applications to the solar wind. *Journal of Geophysical Research*, **115**, A08103.  
**Referenced on page: 38 and 38.**
- Zaslavsky, A., Meyer-Vernet, N., Hoang, S., Maksimovic, M., and Bale, S. (2011). On the antenna calibration of space radio instruments using the galactic background: General formulas and application to STEREO/WAVES. *Radio Science*, **46**.  
**Referenced on page: 42.**
- Zheleznyakov, V. V. and Zaitsev, V. V. (1970a). Contribution to the Theory of Type III Solar Radio Bursts. I. *Soviet Astronomy*, **14**, 47.  
**Referenced on page: 54.**

Zheleznyakov, V. V. and Zaitsev, V. V. (1970b). The Theory of Type III Solar Radio Bursts. II. *Soviet Astronomy*, **14**, 250.

**Referenced on page:** 54.